A THESIS

SUBMITTED TO

UNIVERSITY OF ABOU BEKR-BELKAID -TLEMCEN

for a degree of

Doctor

in the subject of Physics

by

Miss KHELIFI SAMIRA

Effect of Impurities and Defects on Performance and Degradation of Solar Cells

Examination committee:

prof. Tayeb Benouaz	University of Abou-Bakr Belkaid- Tlemcen	Chairman
prof. Abderrahmane Belghachi	University of Bechar	Promoter
prof. Marc Burgelman	University of Gent (Belgium)	Co-Promoter
prof. Abderrachid Helmaoui	University of Bechar	Examinator
prof. Abdelkader Saidane	ENSET (Oran)	Examinator
dr. Abdelkrim Merad	University of Abou-Bakr Belkaid- Tlemcen	Examinator

Academic Year 2009-2010

Acknowledgements

So many people helped me along the way, and I am grateful to all of them.

First of all, a big thanks to my promoters Abderrahmane Belghachi and Marc Burgelman, who were always willing to discuss all aspects of the work in great details, and to help me find the simplest solution to the wide variety of challenges we faced. Without their commitment to find the necessary resources and implement new ideas, none of this would have ever happened. I commend them both for their noble efforts in guiding me and encouraging me at the difficult moments.

I am also immensely grateful to my thesis committee members. A deepest thanks to Pr. Tayeb Benouaze for agreeing to chair the lecture committee of my thesis and also to Pr. Abderrachid Helmaoui, Pr. Abdelkader saidane and Dr. Merad Abdelkrim for accepting to be in the lecture and examination jury of this work.

The time I spent at Gent University working on my doctorate was an experience that will continue to shape me for the rest of my life, and I wish to thank everyone who contributed to it. I give my deepest thanks to the following persons for their help during the preparation of my thesis: Dr. Nadine Carchon (of ELINTEC, University of Gent) for the GaAs sample's etching, Dr. Johan Lauwaert (Solid States Lab) for the DLTS measurements, ir. Hamidreza Azarinia (ELIS, University of Gent) for the FIB measurements and ir. Nico De Roo (Solid States Lab, University of Gent) for the XPS measurements.

It was always my great privilege to have worked with some amazing colleagues during this time. Special thanks to Johan Verschraegen, working together on the IPV effect's subject was very interesting and fruitful. Thanks to Jonas Marlein who provided me the benefits of his own measurement

experience. I cannot forget Koen Decock, he was there with me in the Lab and he always find time in his busy research shedule to help me. Thanks to Ben Minaert, Catelijne Grasso and Masoumeh Karvar for their precious friendship.

I couldn't ask for a better family than my parents, my sisters and my brother, his wife and my two nephews, the twins. Having a family that I knew I could count on without fail and that were always sure to ask what and how I was doing.

To my parents, I give them my deepest thanks for all the love, support and encouragement that they have given me over the years.

Table of contents

Summary

The solar photovoltaic (PV) industry continues to be one of the world's fastest growing industries. The global industry ended 2008 with over 8 GW of PV modules manufactured.

Any mature solar cell technology seems likely to evolve to the stage where costs are dominated by those of the constituent materials. First generation solar cells had high production costs with moderate efficiency. Second generation cells offer much lower overall production cost, but efficiencies are even lower. Third generation cells aim at high efficiency and slightly higher production costs. Therefore, different materials and technologies in PV manufacturing have been used in an attempt to reduce manufacturing costs.

Therefore, research in the field of solar cells is continuously increasing, in order to fabricate high efficiency cells and using inexpensive materials and technologies. In this dissertation, defect's investigation has been performed in solar cells. For this purpose, I report on research on different kind of solar cells by the means of characterization, analysis and simulation. In the third generation solar cells, impurity photovoltaic effect (IPV) was suggested some time ago as a new approach to improve solar cell performance, especially the short-circuit current, by using sub-band gap photons and extending the infrared response. In this thesis, the IPV effect in silicon solar cells with indium impurity level was reinvestigated, new results are given using the software scaps, which was extended for this purpose in a joint work between the two laboratories, ELIS (Gent, Belgium) and LPDS (Béchar, Algeria). Also, for the first time to our knowledge, IPV effect was investigated in wide band gap material (GaAs) with more than one impurity level in the band gap of the semiconductor. New results have been obtained

and published, showing the possibilities and also the limitations of the IPV effect in solar cells.

Furthermore, some selected problems have been analyzed during my research by use of numerical simulation. GaAs concentrator solar cells offer the possibility of reducing the panel cost by using higher power incident on the cell. However, the use of concentrator increases the temperature of the solar cell, which reduces the cell efficiency if no special measures are taken for cooling. In this perspective, the effect of concentration and temperature on GaAs solar cell performance has been analyzed by simulation.

Micro thin film solar cells are good candidates for built-in power sources for a new generation of MEMS (Micro-Electro-Mechanical-Systems). They have the advantage of being small and light weight, and above all, a high output voltage can be obtained with cell sizes on the order of micrometers. For that reason, a number of single solar cells are connected in series to produce the required high voltage. However, in this kind of cells (small area mesa diode), the current due to perimeter recombination is very important and can reduce the cell output. In this thesis, the perimeter recombination effect was investigated in GaAs-based micro-solar cells. The calculations obtained by scaps software were modified to take into account the perimeter recombination effect which is a two dimensional effect.

The use of GaAs pin diodes in photovoltaic application has been recently the focus of a lot of investigations, some of them being in multiple quantum well solar cells. GaAs solar cells with different intrinsic layer thicknesses, were fabricated at the Institute of electronic structure and lasers of the University of Heraklion (Greece), and then sent to our University for electrical characterization. Measurement numerical analyses have been carried out on these cells in order to find a correlation between the quality and the thickness of the intrinsic layer and the device performance.

Thin film solar cells are attractive because they could produce electricity cheaper than conventional silicon solar cells. Absorber materials based on amorphous and microcrystalline silicon (a-Si, μc-Si), on copper indium-gallium diselenide (CIGS), and on cadmium telluride have been considered as the prime candidates for thin film solar cells. The challenge is to reliably and cheaply produce thin film solar cells at large scale and with a decent efficiency performance. Some of these materials show excellent promise in term of efficiency (this is the case for CIGS), whilst others excel in the ease of large scale producibility (the case of a-Si and CdTe) . For example, CIGS solar cells have shown the highest efficiency of any thin film cell with 20 %

efficiency on a glass substrate, thereby largely exceeding the efficiency of present day commercial silicon solar panels ($\eta = 15 – 16$ %). But, it remains difficult until now to reach this level of efficiency in mass-produced cells.

Flexible solar cells offer distinct advantages over cells on rigid glass substrate, in terms of manufacturability and application possibilities, and this has motivated quite a lot of studies of these cells. However, the substitution of a glass substrate by an alternative material results in reducing the device performance, for both the low-temperature process on polyimide and the high-temperature process on metal substrates. Metallic foil substrates offer some attractive features when compared to plastic foil substrates, the most important being that they can withstand the high processing temperatures needed to optimize the CIGS materials quality. However, unwanted diffusion of impurities from the metal substrate to the CIGS cell should be avoided or be under control. Increasing activities to develop and to fabricate flexible CIGS-based devices have been observed over the past years. PVFlex Solar GmbH is a German company specializing in development and manufacturing of flexible light weight solar panels. In the framework of a European project, we received several flexible CIGS thin film solar cells grown on different metallic foils with and without barrier layers. The substrate structures were completed to CIGS solar cells by the Helmholtz Zentrum Berlin (HZB; formerly called Hahn Meitner Institute, HMI). Measurements and simulation have been carried out on these cells in order to find a correlation between the properties of the CIGS devices and the substrate treatment. Besides the electrical characterization, additional measurements have been performed on these cells such as XPS and DLTS characterization to investigate the nature of defects existing in these cells, and limiting or not their performance.

Résumé

L’industrie photovoltaïque solaire continue à être l'une des industries les plus rapides en croissance dans le monde. La fin de l’année 2008 a enregistré une industrie globale de 8 GW de modules photovoltaïques fabriqués. Toute technologie avancée de cellule solaire semble susceptible d'évoluer vers le stade où les coûts sont dominés par celles des matériaux constitutifs. La première génération de cellules solaires ont eu des coûts de production élevés avec un rendement modéré. La deuxième génération de cellules solaires offrent un coût de production global beaucoup plus faible, mais leurs rendements sont encore plus bas. Les cellules solaires de troisième génération ont un rendement élevé et une légère augmentation des coûts de production. Par conséquent, différents matériaux et technologies dans la fabrication PV ont été utilisés pour tenter de réduire les coûts de fabrication. La recherche dans le domaine des cellules solaires ne cesse d’augmenter, afin de fabriquer des cellules solaires à rendement élevé et d'utiliser des matériaux et des technologies peu coûteux. Dans cette thèse, une recherche sur les defaults présents dans les cellules solaire a été realisée. Dans ce but, des études ont été effectuées sur différents types de cellules solaires par le moyen de caractérisation, d'analyse et de simulation numérique. Dans la troisième génération de cellules solaires, l'effet photovoltaïque d’impureté (PVI) a été proposé il y a quelques années comme une nouvelle approche pour améliorer les performances des cellules solaires, particulièrement le courant de court-circuit, en utilisant les photons d’énergie inférieure à celle de la bande interdite, et l'extension de la réponse infrarouge. Dans cette thèse, l'effet PVI a été réétudié dans des cellules solaires à base de silicium possédant un niveau d'impuretés d'indium. De nouveaux résultats sont présentés en utilisant le logiciel scaps, qui a été modifié pour cet effet, dans un travail commun entre les deux laboratoires, ELIS (Gent, Belgique) et LPDS (Béchar, Algérie). En outre, c’est pour la première fois à notre

connaissance, que l'effet PVI a été étudié dans des matériaux à large bande interdite (GaAs) avec plus qu'un niveau d'impureté présent dans la bande interdite du semiconducteur. De nouveaux résultats ont été obtenus et publiés, montrant les possibilités et aussi les limites de l'effet PVI dans ces cellules solaires.

Au cours de ma recherche, quelques problèmes physiques ont été sélectionnés et analysés par simulation numérique. Les cellules à concentrateurs à base de GaAs offrent la possibilité de réduire le coût du panneau solaire à l'aide de l'utilisation de puissance incidente élevée sur la cellule. Cependant, l'utilisation de concentrateur augmente la température de la cellule solaire, ce qui réduit son rendement si aucune mesure particulière n'est prise en compte pour le refroidissement. Dans cette perspective, l'effet de concentration et de la température sur le rendement des cellules solaires à base de GaAs a été analysé par simulation numérique.

Les micro-cellules solaires à couches minces sont bonnes candidates pour les sources de puissance intégrées, vues comme une nouvelle génération de MEMS (Micro-Electro-Mechanical-Systems). Ils ont l'avantage d'être petites et légères, en plus, une tension de sortie élevée peut être obtenue avec des cellules de taille de l'ordre de micromètres. C'est la raison pour laquelle, un certain nombre de cellules solaires sont connectés en série pour obtenir la tension élevée nécessaire. Toutefois, dans ce type de cellules (petite surface, diode Mesa), le courant dû à la recombinaison au périmètre est très important et peut réduire les paramètres de sortie de la cellule. Dans cette thèse, l'effet de la recombinaison au périmètre a été étudié dans des micro-cellules solaires à base de GaAs. Les calculs obtenus par le logiciel scaps ont été modifiés pour tenir compte de l'effet de recombinaison au périmètre qui est un effet à deux dimensions.

L'utilisation des diodes PIN à base de GaAs en application photovoltaïque a été récemment l'objet de beaucoup de recherches, certains d'entre eux étant en cellules solaires aux puits quantiques multiples. Des cellules solaires à base de GaAs avec différentes épaisseurs de la couche intrinsèque, ont été fabriquées à l'Institut de structure électronique et lasers de l'Université d'Heraklion (Grèce), puis envoyées à notre Université pour caractérisation électrique. Des analyses numériques et des mesures électriques ont été réalisés sur ces cellules afin de trouver une corrélation entre la qualité et l'épaisseur de la couche intrinsèque, et les performances de la cellule.

Les cellules solaires à couches minces sont attractives car elles pourraient produire de l'électricité moins chère que dans les cellules solaires

conventionnelles à base du silicium. Les matériaux utilisés pour l'absorbeur (ou émetteur), comme le silicium amorphe et microcristallin (a-Si, μ c-Si), le cuivre-indium- gallium-séléniure (CIGS), et le tellurure de cadmium sont considérés comme les premiers candidats pour les cellules solaires à couches minces. Le défi consiste à produire des cellules solaires à couches minces d'une manière fiable et peu coûteuse, à grande échelle et avec un rendement décent. Certains de ces matériaux ont un avenir prometteur en terme de rendement (c'est le cas du CIGS), tandis que d'autres sont excellent dans la facilité de la productibilité en grande échelle (le cas du a-Si et CdTe). Par exemple, les cellules solaires CIGS ont le rendement le plus élevé de n'importe quelle cellule solaire à couches minces avec 20% de rendement sur un substrat de verre, dépassant ainsi largement le rendement des panneaux solaires commerciaux actuels, à base du silicium (η = 15 - 16%). Mais, il reste difficile jusqu'à présent d'atteindre ce niveau de rendement dans la production en masse des cellules.

Les cellules solaires flexibles offrent des avantages différents, en termes de fabrication et les possibilités d'application, par rapport aux cellules solaires sur un substrat en verre rigide, ce qui a beaucoup motivé les recherches sur ces cellules. Toutefois, la substitution d'un substrat de verre par un matériau alternatif conduit à la réduction des performances de la cellule, et cela dans les deux processus de fabrication, à basse température sur les polyimides, ainsi qu'à haute température sur des substrats métalliques. Les substrats métalliques offrent des caractéristiques attractives par rapport à ceux en plastique, le plus important étant qu'ils peuvent supporter les températures de traitement élevées, nécessaires pour optimiser la qualité des matériaux CIGS. Toutefois, la diffusion indésirable des impuretés, du substrat métallique vers la cellule CIGS devrait être évitée ou contrôlée. Une augmentation considérable dans les activités de recherche pour le développement et la fabrication des cellules solaires flexibles à bases de CIGS a été observée, au cours de ces dernières années. PVFlex Solar GmbH est une société allemande spécialisée dans le développement et la fabrication des panneaux solaires flexibles et légers. Dans le cadre d'un projet européen, nous avons reçu plusieurs cellules solaires à couches minces flexibles à base de CIGS, fabriquées sur différentes feuilles métalliques (substrats), avec ou sans couches barrière. Ces cellules solaires à base de CIGS ont été fabriquées par Helmholtz Zentrum Berlin (HZB; anciennement appelé Hahn Meitner Institut, IHM). Des mesures électriques et des simulations numériques ont été effectuées sur ces cellules afin de trouver une corrélation entre les propriétés des composants et le traitement du substrat. Outre la

caractérisation électrique, des mesures supplémentaires ont été effectuées sur ces cellules, telles que la caractérisation par XPS et DLTS et cela pour déterminer la nature des défauts existants dans ces cellules, et limitants ou pas leur performance.

List of figures

List of tables

List of symbols and abbreviations

Symbols

α	[/cm]	optical absorption constant
$\alpha_{e\text{-}h}$	[/cm]	optical absorption constant due to band-to-band excitation (creation of electron-hole pairs)
α_{fc}	[/cm]	optical absorption constant due to free carrier absorption
α_n	[/cm]	optical absorption constant due to emission of electrons from a defect (IPV effect)
α_p	[/cm]	optical absorption constant due to emission of holes from a defect (IPV effect)
α_{tot}	[/cm]	total optical absorption constant
α_i		integrated absorption of the wavelengths for a given illumination.
β	[-]	an exponent describing the $C(V)$ dependency
ε		surface emissivity
ε_0	[F/cm]	permittivity of vacuum
ε_s	[-]	relative dielectric constant of a semiconductor
λ	[nm] or [μm]	wavelength
μ_n	[cm^2/Vs]	electron mobility
μ_p	[cm^2/Vs]	hole mobility
ρ_t	[C/cm^3]	charge density in deep traps (defects)
ϕ	[$\#/cm^2$.nm]	photon flux density per wavelength
Φ	[V]	electrostatic potential

η	[-] or [%]	photovoltaic conversion efficiency
σ	[W/m^2.K^{-4}]	Stefan-Boltzmann constant
σ_n	[cm^2]	capture cross section for electrons
σ_n^{opt}	[cm^2]	optical capture cross section for electrons
σ_p	[cm^2]	capture cross section for holes
σ_p^{opt}	[cm^2]	optical capture cross section for holes
τ	[s]	a time constant
τ_n	[s]	electron minority carrier life time
τ_p	[s]	hole minority carrier life time
τ_s	[s]	time constant of surface states
ω	[1/s]	angular frequency
A	[cm^2]	cell area
c	[cm/s]	velocity of light
C	[-]	concentration ratio (illumination intensity relative to 1 sun = 1000 W/m^2)
C	[F/cm^2]	cell capacitance per unit area
C_d	[F/cm^2]	diffusion capacitance per unit area
C_{hf}, C_{lf}	[F/cm^2]	high and low frequency limits of the capacitance
C_j	[F/cm^2]	junction capacitance (or depletion capacitance) per unit area
C_s	[F/cm^2]	contribution of surface states to the capacitance per unit area
C_t	[F/cm^2]	contribution of traps or defects to the capacitance per unit area
C_{fc}^n, C_{fc}^p	[-]	empirical constants in calculating free carrier absorption
D_n	[cm^2/s]	electron diffusion constant
D_p	[cm^2/s]	hole diffusion constant
E	[V/cm]	electric field
E	[V/cm]	electric field of the incident wave
E_A, E_a	[eV]	apparent activation energy
E_C	[eV]	bottom edge of conduction band
E_D	[eV]	ionization energy for donors
E_{eff}	[V/cm]	electric field at the impurity
E_F	[eV]	(equilibrium) Fermi level
E_{Fn}	[eV]	electron Fermi level
E_{Fp}	[eV]	hole Fermi level

EQE	[-] or [%]	external quantum efficiency
E_T	[eV]	trap level; energy level of a defect
f	[Hz]	frequency
f_t	[-]	probability that a trap or defect is occupied with an electron
FF	[-] or [%]	fill factor
G	[#/cm^3.s]	(optical) carrier generation rate
h	[J.s]	Planck's constant
$\hbar$	[J.s]	reduced Planck's constant ($\hbar = h/2\pi$)
h_c	[W.m^{-2}.K^{-1}]	Heat transfert coefficient
$h\nu$	[J or eV]	photon energy
I_{cell}	[A]	short circuit current of a solar cell to be measured (QE measurement)
I_{ref}	[A]	short circuit current of a the reference cell (QE measurement)
IQE	[-] or [%]	internal quantum efficiency
J	[A/cm^2]	current density
J_0	[A/cm^2]	(dark) saturation current density
J_m	[A/cm^2]	current density at maximum power
J_{peri}	[A/cm^2]	contribution of perimeter recombination to the dark current
J_{rec}	[A/cm^2]	contribution of recombination to the dark current
J_{sc}	[A/cm^2]	short circuit current density
J_n	[A/cm^2]	electron particle current density
J_p	[A/cm^2]	hole particle current density
k	[J/K] or [eV/K]	Boltzmann constant
m_n^*	[Kg]	electron effective mass
m_p^*	[Kg]	hole effective mass
n	[-]	diode ideality factor
n	[-]	index of refraction
N_A	[1/cm^3]	shallow acceptor density
N_A^-	[1/cm^3]	density of ionised shallow acceptors
N_C	[1/cm^3]	effective density of states in the conduction band
N_D	[1/cm^3]	shallow donor density
N_D^+	[1/cm^3]	density of ionised shallow donors
N_t, N_T	[1/cm^3]	density of traps, defects
N_V	[1/cm^3]	effective density of states in the valence band

P_{inc}	[W/cm^2]	incident light power density
q	[C]	elementary charge
QE	[-] or [%]	quantum efficiency
R	[#/cm^3.s]	(thermal) recombination rate
R_b	[-] or [%]	internal reflection at the bottom surface of a solar cell
R_f	[-] or [%]	internal reflection at the front surface of a solar cell
R_s	[Ω]	series resistance
$R_s.A$	[Ω.cm^2]	series resistance for a unit area cell
R_{sh}	[Ω]	shunt resistance
$R_{sh}.A$	[Ω.cm^2]	shunt resistance for a unit area cell
S_{cell}	[A.cm^2/W]	spectral sensitivity of the cell to be measured (*QE* measurement)
S_{ref}	[A.cm^2/W]	spectral sensitivity of the reference cell (*QE* measurement)
T	[K]	absolute temperature
v_{th}	[cm/s]	thermal velocity
V	[V]	voltage, applied voltage
V_{bi}	[V]	built-in voltage
V_m	[V]	voltage at maximum power
V_{oc}	[V]	open circuit voltage
w_i	[cm, μm or nm]	width of the intrinsic layer (*pin* cell)
W	[cm, μm or nm]	depletion layer width

Abbreviations

AM1.5G	Air Mass 1.5 Global solar spectrum
AS	Admittance spectroscopy
BIPV	Building Integrated Photovoltaics
BSF	Back Surface Field
CIGS	Copper indium gallium selenide $Cu(In,Ga)Se_2$
CPE	Constant Phase Element
DLTS	Deep Level Transient Spectroscopy
ELIS	Department (Vakgroep) of Electronics and Information Systems at UGent
FIB	Focussed Ion Beam
FSF	Front Surface Field
HF	high frequency limit
HZB	Helmholtz Zentrum Berlin für Materialien und Energie
IB	Intermediate Band
III-V	A binary compound of a group III element (B, Al, Ga or In) and a group V element (N, P, As, Sb). Or a ternary, quaternary,… compound based on binary III-V compounds
IPV	Impurity Photovoltaic Effect
IS	Impedance spectroscopy
LF	low frequency limit
LPDS	Laboratoire de Physique des Semiconducteurs, at the Université de Béchar, Algeria
MBE	Molecular Beam Epitaxy
MEMS	Micro Electro-Mechanical Systems
MIA	Measure It All. The *J-V*, *C-V* and *C-f* measurement system of ELIS, UGent
OVC	ordered vacancy CIGS compound, such as $CuIn_3Se_5$
PI	poly-imide
PIA	Plot It All. A measurement interpretation programme of ELIS, UGent (developed in ELIS by ir. K. Decock)
PV	Photovoltaic
QW	Quantum well
SCAPS	A solar cell capacitance simulator, a simulation software of ELIS, UGent
SCR	Space charge region, depletion layer
SEM	Scanning Electron Microscopy
SIMS	Secondary Ion Mass Spectroscopy

SRC	Standard reporting conditions for solar cells and modules (see also STC)
SRH	Shockley-Read-Hall recombination mechanism
SS	Stainless steel
STC	Standard reporting conditions for solar cells and modules (see also SRC)
W	Warburg element
XRF	X-Ray Fluorescence
XPS	X-ray Photoelectron Spectroscopy

List of Publications

International Journals (ISI)

[1] S. Khelifi et A. Belghachi, "Le Rôle de la Couche Fenêtre dans les Performances d'une Cellule Solaire GaAs", *Revue des Energies Renouvelables*, vol. 7, pp.13-21, 2004.

[2] A. Belghachi, S. Khelifi, "Modelling of Perimeter recombination effect in GaAs-based micro-solar cell", *Solar Energy Materials and Solar Cells*, vol. 90, pp. 1 – 14, 2006.

[3] S. Khelifi, J. Verschraegen, M. Burgelman, A. Belghachi, "Numerical Simulation of Impurity Photovoltaic Effect in Silicon Solar Cells", *Renewable Energy*, vol. 33, pp.293 – 298, 2008.

[4] S. Khelifi, L. Ayat Leila, A. Belghachi, "Effects of temperature and series resistance on GaAs concentrator solar Cell", *European Physical Journal, Applied Physics*, vol. 41, pp.115 – 119, 2008.

[5] S. Khelifi, M. Burgelman, J. Verschraegen, A. Belghachi, "Impurity Photovolatic Effect in GaAs Solar Cell with two deep impurity levels", *Solar Energy Materials and Solar Cells*, vol. 92, pp.1559-1565, 2008.

[6] A.F. Meftah, N. Sengouga, A.M. Meftah, S. Khelifi, "Numerical simulation of the Al molar fraction and thickness of an $Al_xGa_{1-x}As$ window on the sensitivity of a p^+-n-n^+ GaAs solar cell to 1 MeV electron irradiation", *Renewable Energy*, vol. 34, No.11, pp.2426-2431, 2009.

[7] J. Lauwaert, K. Decock, S. Khelifi, M. Burgelman, "A simple correction method for series resistance and inductance on solar cell admittance spectroscopy", accepted for publication in *Solar Energy Materials and Solar Cells*, 2009.

[8] Samira Khelifi, Abderrahmane Belghachi, Johan Lauwaert, Koen Decock, Jeannette Wienke, Raquel Caballero, Christian A. Kaufmann,

Marc Burgelman, "Characterization of flexible thin film CIGSe solar cells grown on different metallic foil substrates", accepted for publication in *Energy Procedia*, 2009.

International Conferences

[9] Samira Khelifi, Johan Verschraegen, Marc Burgelman, Abderrahmane Belghachi, "Numerical Simulation of Impurity Photovoltaic Effect in Silicon Solar Cells", E-MRS Conference, (European Material Research Society), Spring Meeting, Nice (France) 29th May – 01st June 2006, Symposium M.

[10] Johan Verschraegen, Samira Khelifi, Marc Burgelman, Abderrahmane Belghachi, "Numerical Modeling of Impurity Photovoltaic Effect (IPV) in SCAPS", The proceedings of 21st EU PVSEC (European Photovoltaic Solar Energy Conference and Exhibition), Dresden (Germany), 4-8 September 2006, pp.396-399.

[11] Samira Khelifi, Johan Verschraegen, Marc Burgelman, Abderrahmane Belghachi, "Impurity Photovoltaic Effect in GaAs Solar Cell with two deep impurity levels", International Workshop on Numerical Modelling of Thin Film Solar Cells, Proceedings of PhD, Gent, Belgium 28-30 March 2007, pp.275-286.

[12] Samira Khelifi, Jonas Marlein, Marc Burgelman, Abderrahmane Belghachi, "Electrical Characteristics of $Cu(In,Ga)Se_2$ Thin Films Solar Cells Metallic Foil Substrates", The proceedings of 23rd EU PVSEC (European Photovoltaic Solar Energy Conference and Exhibition), Valencia (Spain), 1-5 September 2008, pp.2165-2169.

[13] Samira Khelifi, Abderrahmane Belghachi, Johan Lauwaert, Jeannette Wienke, Raquel Caballero, Christian A. Kaufmann, Marc Burgelman, "Characterization of flexible thin film CIGSe solar cells grown on different metallic foil substrates", presented in E-MRS Spring Meeting Strasbourg, 2009.

National Conferences

[14] Samira Khelifi et Belghachi Abderrahmane, "Modélisation et Simulation numérique d'une Cellule Solaire pin (nip) à base de $Ga_{0.3}Al_{0.7}As/GaAs$", $6^{ième}$ Séminaire International sur la Physique Energétique, Béchar (Algérie) 21 au 23 Octobre 2002.

[15] Samira Khelifi et Abderrahmane Belghachi, "Modélisation d'une Cellule Solaire nip à Base de $Ga_{1-x}Al_xAs/GaAs$", La conférence Internationale sur la Physique et ses Applications, USTMB, Oran (Algérie) du 08 au 10 Décembre 2003, pp 292-295.

[16] Samira Khelifi et Abderrahmane Belghachi, "Simulation des performances d'une cellule Solaire à Couches Minces $Ga_{1-x}Al_xAs/GaAs$", International Congress on Photovoltaic and Wind Energies (ICPWE), Université Abou Bekr Belkaid, Tlemcen (Algérie), du 20 au 22 décembre 2003.

[17] Ayat Leila, Samira Khelifi, Abderrahmane Belghachi, "Effect of Temperature and Series Resistance on AlGaAs/GaAs Concentrator Solar Cell", Le Colloque International OASIS'2006 (Ordre-désordre; Alcane ; Simulation ; Spin), Université de Béchar (Algérie), du 11 au 13 Novembre 2006.

[18] Samira Khelifi, Johan Verschraegen, Marc Burgelman, Abderrahmane Belghachi, "Numerical Simulation of Impurity Photovoltaic Effect in GaAs Solar Cells", Le 7ième Congrès National de la Physique et ses Applications (CNPA'2006), Université de Béchar (Algérie), du 18 au 21 Décembre 2006.

[19] Ouahabi Foudil, Samira Khelifi, Abderrahmane Belghachi, "Modélisation d'une Cellule Solaire pin AlGaAs/GaAs à Puits Quantiques Multiples", Le 7ième Congrès National de la Physique et ses Applications (CNPA'2006), Université de Béchar (Algérie), du 18 au 21 Décembre 2006.

[20] Samira Khelifi, Johan Verschraegen, Marc Burgelman, Abderrahmane Belghachi, "Numerical Simulation of Impurity Photovoltaic Effect in GaAs Solar Cells", International Congress on Photovoltaic and Wind Energies (ICPWE), Université Abou Bekr Belkaid, Tlemcen (Algérie), du 20 au 22 Mai 2007.

Chapter 1

Introduction

In the 1970s the energy supply crisis caused by an excessive dependency on oil supply, led to a abrupt growth of interest in alternative sources of energy, such as solar, wind, biomass, hydro, geothermal and ocean waves. Solar energy is a promising source of future energy supplies because not only is it clean, but also because it is remarkably abundant. The sun's energy is not depleted when we use it, and it is available free of charge to the entire planet: therefore it is called renewable or sustainable. In photovoltaic (PV) solar energy, solar energy is direct converted into electrical energy. PV solar energy can reduce the use of oil, natural gas and propane, while emitting no global warming pollution.

Photovoltaic solar energy was a subject of continuous and intense interest since the first oil crisis, and many strategies for producing photovoltaic devices more cheaply and improving device efficiency were explored. In the late of 1990s the photovoltaic production extended of rate of 15-25 % per annum, leading to a reduction in cost. Photovoltaics first became competitive in contexts where conventional electricity supply is more expensive, for remote low power applications such as navigation, telecommunications, and rural electrification and for enhancement of supply in grid-connected loads. As prices fall, new markets are opened up. An important example is the application of building integrated photovoltaics (BIPV), where the cost of the photovoltaic system is offset by the savings in building materials.

At the end of 2008 and in early 2009, in part in response to the financial crisis, a number of national governments announced plans to increase public finance of renewable energy.

Overall, renewable power capacity expanded to 280 GW in 2008, a 75 percent increase from 160 GW in 2004 excluding large hydropower (see Figure 1). The capacity in developing countries grew to 119 GW. The top six countries were China (76 GW), the USA (4O GW), Germany (34 GW), Spain (22 GW), India (13 GW) and Japan (8 GW). The capacity of developing countries grew to 119 GW.

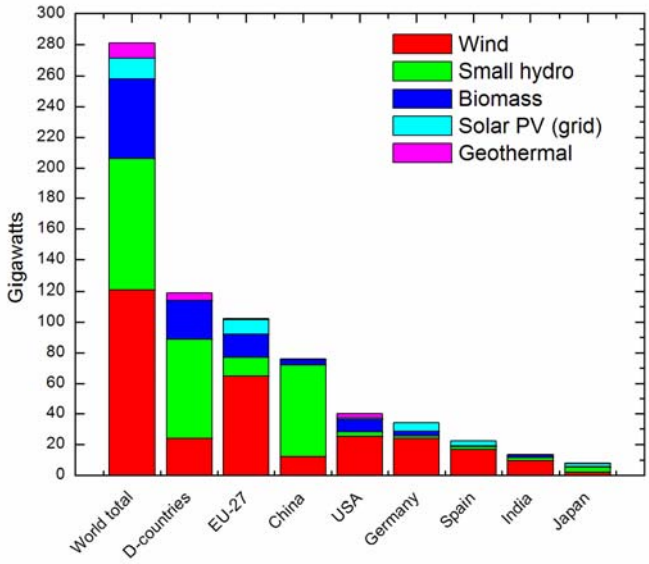

Figure 1 Renewable electric power capacity existing as of 2008 [1] (graph made from data in Table R4, pp.24).

The solar PV industry continues to be one of the world's fastest growing industries. Global annual production increased nearly sixfold between 2004 and 2008, reaching 6.9 GW. This is due to two important trends, first growing attention to building-integrated PV, which increase to 13 GW in 2008 (see Figure 2) and second thin film solar PV technologies which became larger share of total installations. The global PV industry ended 2008 with over 8 GW of cell manufacturing capacity, including 1 GW of thin film capacity.

Nevertheless, in 2008 solar PV markets showed some clear trends. One was the growing attention of building integrated PV, which is small but fast growing of some markets, with more than 25 MW installed in Europe. The second one that thin film solar PV technologies became larger share of total installations.

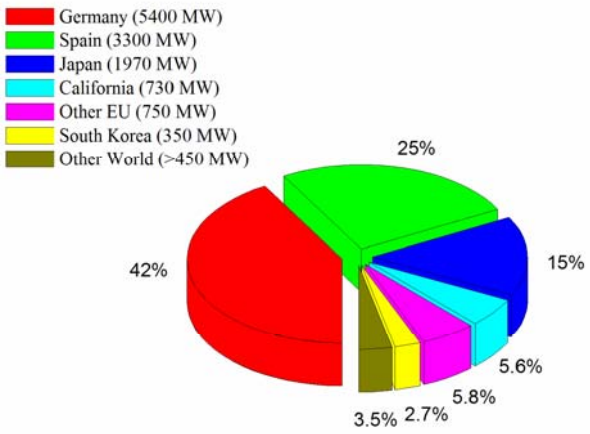

Figure 2 Grid connected Solar PV (MW) existing as of 2008 [1] (graph made from data in Table R3, pp.24).

The production cost of PV modules has been decreasing continuously as a result of increasing production volume (economics of scale, 'learning curve') and as a result of intensive research.

Crystalline solar cells based on mono or multi crystalline silicon, or on crystalline GaAs and other III-V compounds are sometimes called first generation solar cells. The development of these cells has taken large profit from the massive knowledge base that has been developed for these materials in the microelectronics research and industrial applications. However, even these well established solar cells have a complicated structure, consisting of several distinct layers and interfaces; this holds especially for III-V based solar cells. The quantitative assessment of the influence of some materials of structure property on the final solar cell properties is often beyond intuition, and even the application of analytical textbook formulas, based on Shockley's ideal *pn* junction theory if often

insufficient. The use of numerical simulation has become standard in research on crystalline silicon and III-V solar cells.

Thin film solar cells consist of thin (order of μm) active layers deposited on a passive or inert substrate, e.g. glass. The most important thin film cell families are the CIGS family (based on $Cu(In,Ga)Se_2$ and other chalcopyrite absorber films), the CdTe family (based on polycrystalline CdTe absorber films) and the thin Si family (based on amorphous silicon Si:H or silicon alloys SiGe:H or SiC:H, or on micromorphous Si, or combinations between these materials). These thin film solar cells are sometimes called second generation solar cells. These cells are developed more recently than crystalline cells. Excellent research results have been obtained with these cells, e.g. a 20 % efficient laboratory-scale CIGS cell [2]. The industrial production of these cells is emerging, and, as mentioned before, their market share is now of the order of 10 %. The physical and electronic operation of these cells is far more complicated than that of crystalline Si cells. Dedicated numerical programmes have been developed for a realistic numerical simulation of thin film cells [3]. The ELIS department of the University of Gent has taken active part in this research line with the development of SCAPS, a numerical simulation tool available freely to PV research community and mainly used for $Cu(In,Ga)Se_2$ and CdTe based thin film solar cells [4].

'Third generation solar cells' is a generic term for a collection of solar cells and solar cell ideas that make use of particular physical phenomena to improve the cell efficiency. These term and the ideas underneath has been actively promoted by Martin Green of the University of New South Wales, Australia [5]. Tandem solar cells and multijunction solar cells, which consist of a stack of *pn* solar cells, are sometimes classified as third generation solar cells. They achieve the highest conversion efficiencies, even exceeding 40 % [6], at the expense of a very complicated cell structure. All other third generation ideas are still in a research phase, and none of them has yet lead to an experimental efficiency improvement. Some of these third generation ideas are: the impurity photovoltaic effect (IPV), impurity band solar cells (IB), multiple quantum wells (QW), impact ionisation, hot carrier solar cells, up and or down conversion of photons, … In this thesis, we will deal with IPV solar cells.

The guideline of this thesis is the use of numerical simulation to obtain a better understanding and insight in various types of solar cells. Selected problems in first, second and third generation solar cells have been studied.

The content of this thesis is as follows:

Chapter two presents a general introduction to basic concepts of solar cells, and gives a brief description of the simulation tool and the characterization methods used during my research.

Chapter three is dedicated to the simulation of the IPV effect in silicon solar cells with one deep impurity level, and of the IPV effect in GaAs solar cell with more than one impurity level. To our knowledge, this was the first time that IPV effect was numerically investigated in wide band gap material with multi-defect levels. This study allowed us to give an overview on the possibilities and the limitations of this particular 'third generation' approach to improve the solar cell performance.

Chapter four is treating several effects in crystalline GaAs solar cells: the effect of module heating, of low level illumination, and of perimeter recombination. The latter effects are of relevance in a *niche* application (micro-solar cells to power actuator and similar devices).

Chapter five is devoted to the electrical characterization of GaAs solar cells with a *pin* structure with different intrinsic layers. The purpose of this study is to gain insight in the role of the *i*-layer on the cell efficiency.

Chapter six is devoted to the electrical characterization of flexible CIGS thin film solar cells grown on different metallic foils. The efficiency of such cells grown on flexible substrates is lower than that of cells grown on glass substrates. Also here, our goal is to gain more insight in this problem.

Finally, the results are summarized in the last chapter, chapter seven.

Chapter 2

Solar Cells: Basic Concepts

2.1 Introduction

The solar cell is the basic building block of solar photovoltaics. The term photovoltaic is derived by combining the Greek word for light (φωτος, photos), with voltaic, named after Alessandro Volta. A device is said photovoltaic when exposure to the light that can be absorbed by the material is able to transform the energy of light photons into electrical energy. The number of materials that are able to exhibits photovoltaic characteristics is large. However, what is not large is the number of such materials or devices that are able to make such transformation with high conversion efficiency, of the order of 20 %, at low cost, and with high stability under operation. The principles and properties of solar cells are briefly reviewed in this chapter. We include also a brief description of numerical simulation of solar cells (software tool used in our simulation), and the basic measurement principles and methods.

2.2 Solar cell: principle and characteristics

2.2.1 Principle

A conventional solar cell consists of two layers of semiconductor, one positive (*p*-type) and the other negative (*n*-type) juxtaposed to form a *p*-*n* junction. A schematic cross section of a solar cell is shown in Figure 3.

When the cell is illuminated, the energy $h\nu$ of incident photons is absorbed by the semiconductors and breaks electron bonds: electrons are excited from the valence (energy) band to the conduction (energy) band and thereby become mobile, and can carry electric current; in the valence band, holes are left, which also are mobile and can carry current. The electrons and holes near the junction are swept across in opposite directions by the electric field. Diffusion of charge carriers to the electrical contacts causes a voltage to be present at the solar cell. In an unloaded state, the open circuit voltage arises at the solar cell. If the electrical circuit is closed, a current flows.

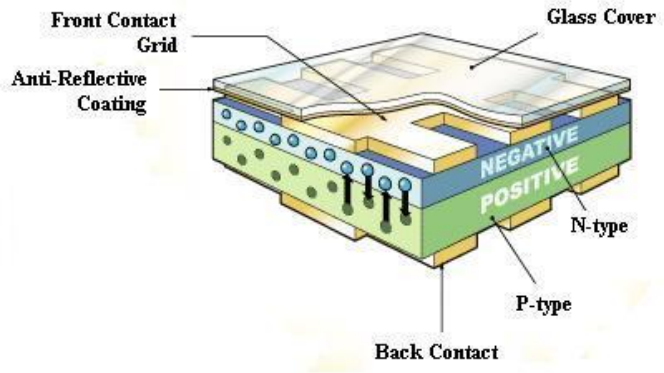

Figure 3 Schematic cross section of a solar cell.

2.2.2 Characteristics

The basic solar cell performance parameters are the short circuit current density J_{sc}, the open circuit voltage V_{oc} , the fill factor FF and the efficiency η. These parameters are defined in Figure 4, and are briefly discussed below.

2.2.2.1 Short circuit current J_{sc}

The flow of carriers into the external circuit constitutes a reverse electrical current density which under short circuit conditions ($V = 0$) is known as the short circuit current density J_{sc}. By convention, we take J_{sc} as a positive quantity, and describe the actual current density at short circuit as either $+J_{sc}$ or $-J_{sc}$, depending on the current reference adopted.

2.2.2.2 Open circuit voltage V_{oc}

The separation of charges sets up a forward potential difference between the two contacts of the solar cell, which under open circuit conditions ($I = 0$) is known as the open circuit voltage V_{oc}.

2.2.2.3 Fill Factor *FF*

The fill factor is a measure of the "squareness" of the *J-V* curve under illumination and is defined as the ratio:

$$FF = \frac{J_m V_m}{J_{sc} V_{oc}} \tag{1}$$

where J_m and V_m are respectively the values of current density and voltage at the maximum power condition. Again, J_m is treated as a positive quantity; the actual current at maximum power then is $\pm J_m$ depending on the current reference.

2.2.2.4 Efficiency η

The efficiency of the cell is the power density delivered at the maximum power point as a fraction of the incident light power density P_{inc}

$$\eta = \frac{J_m V_m}{P_{inc}} = \frac{J_{sc} V_{oc} FF}{P_{inc}} \tag{2}$$

The four quantities J_{sc}, V_{oc}, *FF* and η are the key performance characteristics of a solar cell. All of them should be defined for particular illumination conditions. The standard test conditions (STC) or standard reporting conditions (SRC) for solar cells are the Air Mass 1.5 Global spectrum ('AM1.5G'), an incident power density of 1000 W/m^2 and a cell or module temperature of 25 °C.

2.2.2.5 Quantum efficiency *QE*(λ)

The quantum efficiency *QE* is the number of carriers collected by the solar cell to the number of photons incident on the solar cell. The short circuit current density can be predicted from the wavelength dependency of quantum efficiency *QE*(λ) and the solar spectrum

$$J_{sc} = q \int_{\lambda} \phi(\lambda) QE(\lambda) d\lambda \tag{3}$$

where $\phi(\lambda)$ is the incident photon flux density per unit wavelength bandwidth.

2.2.2.6 *J-V* characteristics

The overall current voltage response of the solar cell, its current voltage characteristic, is the sum of the short circuit current and the dark current. The dark current can usually be approximated quite well by a slight adaptation of the ideal Shockley equation [7]. The *J-V* characteristic is then described by

$$J = J_0\left[\exp\left(\frac{qV}{nkT}\right)-1\right]-J_{sc} \tag{4}$$

where J_0 is the saturation current density, q the elementary charge, k Boltzmann's constant and T the absolute temperature. Thus, the expected current density at reverse bias in the dark is $-J_0$. In Eq. (4), n is called the diode quality factor, or the diode ideality factor. In the ideal Shockley theory, $n = 1$ or $n = 2$. In typical devices, the value of n ranges from 1 to 2.

Figure 4 shows a *J-V* curve measured for GaAs solar cell under dark and illumination at standard conditions.

$J = 0$ yields

$$V_{oc} = \frac{nkT}{q}\ln\left(\frac{J_{sc}}{J_o}+1\right) \tag{5}$$

In real cells, the *J-V* curve deviates from the ideal Eq. (4) by parasitic effects, which can be described by two resistances, one in series (R_s) and one in parallel (R_{sh}) with the cell. Series resistance is due to the resistance of the cell material to current flow, especially through the front surface to the contacts. The parallel resistance can be due to a leakage current trough the cell (e.g. around the edges of the device).

Thus when parasitic resistances are included the diode equation (4) becomes

$$J = J_0\left[\exp\left(\frac{q(V-JR_SA)}{nkT}\right)\right]+\frac{(V-JR_SA)}{R_{sh}A}-J_{sc} \tag{6}$$

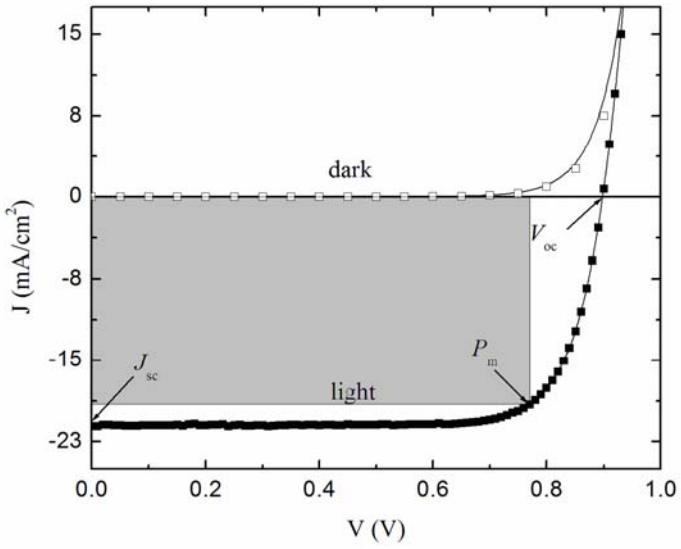

Figure 4 Typical current-voltage (*J-V*) characteristics of a GaAs solar cell, showing the open circuit voltage (V_{oc} = 0.9 V), the short circuit current density (J_{sc} = 21.46 mA/cm^2) and the maximum power point (P_m = 15 mW/cm^2). The other cell characteristics extracted from the curve are *FF* = 78 % and η = 15 %. The top curve is the measured dark current density.

2.3 Numerical simulation of solar cells

Numerical simulation of solar cells is essential, not only for interpretation of advanced measurement on complicated cell structure, but also for design and optimization of cell structures. An ideal thin film solar cell simulation program should meet all the requirements listed in Table 1. Currently, a number of simulation packages are available to the PV research community. This group of software tools includes: AMPS-1D, SCAPS-1D, PC1D, SimWindows, ASA, ADEPT-F, SC-Simul, ASPIN and AFORS-HET. Some of these numerical tools were reviewed and compared by Burgelman et al. [3], where also their possibilities and limitations were discussed.

Amongst the available simulation tools, SCAPS is mainly used for modeling CdTe and CIGS/CIS thin film based solar cells [4]. Although at the beginning the software was designed for CdTe and CIGS solar cells, it was successfully applied for modeling other solar cells based materials, such as

GaAs [8][9]. SCAPS is written and maintained at the University of Gent. Since its first development in the middle of 90's, it was substantially improved and extended in consecutively released versions. Now version 2.8 is available and all the requirements cited in Table 1 are already included in it. SCAPS has now about 280 users all over the world, among them in reputed research institutions and labs.

Table 1 Critical issues for a thin film simulation program [3].

Multiple layers
Band discontinuities in E_C and E_V: ΔE_C and ΔE_V
Wide band gaps: E_g > 2-3.7 eV
Graded band gaps: $E_g(x)$; all other parameters can be graded as well: $\chi(x)$, N_C(x), $N_V(x)$, $\alpha(x)$…
Recombination and charge in deep bulk states
Recombination and charge in deep interface states
Simulation of non-routine measurements:
J-V, *C-V*, *C-f*, *QE*(λ)… all as a function of *T*
Fast and easy to use

SCAPS is capable of solving the basic semiconductor equations, the Poisson equation and the continuity equations for electrons and holes (Eqs. (7)-(9)):

$$\frac{d^2\Phi}{dx^2} = -\frac{q}{\varepsilon_0\varepsilon_s}\left(p - n - N_A^- + N_D^+ + \frac{\rho_t}{q}\right) \tag{7}$$

$$\frac{dJ_n}{dx} = G - R \tag{8}$$

$$\frac{dJ_p}{dx} = G - R \tag{9}$$

Here ε_0 and ε_s are the permetivity of vaccum and semiconductor respectively, Φ is the electrostatic potential, n and p are the free carrier concentrations, N_A^- and N_D^+ are the density of ionized acceptors and donors, ρ_t the charge density contained in defects (deep traps), J_n and J_p are the electron and hole current density, R is the recombination rate, and G is the generation rate.

Carrier transport in semiconductors occurs by drift and diffusion and can be expressed by the equations:

$$J_n = -D_n \frac{dn}{dx} + \mu_n n \frac{d\Phi}{dx} \tag{10}$$

$$J_p = -D_p \frac{dp}{dx} - \mu_p p \frac{d\Phi}{dx} \tag{11}$$

where μ_n, μ_p and D_n, D_p are the carrier mobilities and the carrier diffusion constants for electrons and holes respectively.

The recombination terms in Eqs (8) and (9) have non-linear dependencies on the carrier concentrations n and p. Also, the second (drift) term in the current equations (10) and (11) is non-linear, as it contains the product of two unknown functions n (or p) and Φ. Finally, the carrier concentrations depend exponentially on the electrostatic potential Φ (and the Fermi levels) (Boltzmann or Fermi statistics). Therefore, the basic semiconductor Eqs. (7)-(9) are highly non linear. The set of $3N$ non-linear equations is solved numerically in SCAPS with the following typical approach:

- discretization of the device: in one dimension, the total cell length L is divided in N intervals, and the value of Φ_i and the electron and hole concentrations n_i and p_i at each of the intervals constitute the $3N$ unknowns of the problem.
- discretization of Eqs. (7)-(9): basic equations at each of the intervals i leads to $3N$ non-linear equations (discretization by finite difference method).
- application of boundary conditions (contacts and interfaces).
- solution of resulting matrix equation by iteration, using Scharfetter-Gummel algorithm [10].

In the actual SCAPS code, (Φ_i , E_{Fni}, E_{Fpi}) are used as independent variables instead of (Φ_i , n_i, p_i), where E_{Fni} and E_{Fpi} are the quasi-Fermi energy levels for electrons and holes respectively.

2.4 Electrical characterization methods

The most commonly available electrical characterization methods for thin film solar cells are current density vs. voltage (J-V), capacitance-voltage, quantum efficiency, admittance spectroscopy (AS) and deep level transient spectroscopy (DLTS) measurements. The DLTS measurements were done in the Solid-State Physics department of UGent. All other electrical measurements were done in the department of Electronics and Information

Systems of UGent (ELIS). In this section we will give a short description of the characterization methods as well as the equipment used in our measurements.

2.4.1 Current-voltage characterization

Current-voltage measurements are very important in solar cells characterization. Dark *J-V* measurement provides information on the limiting recombination mechanisms in the solar cell, especially when it is performed as a function of temperature. A *J-V* measurement under illumination and under standard conditions (one sun and illumination and room temperature), is necessary to extract the solar cell performance parameters (V_{oc}, J_{sc}, *FF* and η). An example is shown in Figure 4. However, additional information can be deduced from *J-V* measurement performed at different light intensity and temperature, such as shunt resistance and the band gap of the material.

At ELIS, the *J-V* measurements are carried out by an integrated computer system. The setup consist of a Source Measure Unit (KEITHLEY 236) used as a voltage source, programmed and controlled by a computer, and a solar simulator. Four probes are used (four points measurements) for the contacts as is shown in Figure 5.

Temperature dependent measurement are carried out using a cold finger cryostat mounted on a nitrogen source. A picture showing the temperature measurement seutup as it is used in ELIS is shown in Figure 5, constituted of cold finger cryostat, a nitrogen source, a vacuum pressure gauge to control the pressure inside the cryostat and a flow regulator of nitrogen. Note that the same setup is used for *J-V(T)*, *C-V*(*T*), *C-f*(*T*) and also J_{sc}-V_{oc} measurement. For *J-V(T)* under different illumination intensities we used an Oriel 6143 lamp together with neutral density filters (also shown in Figure 5), to get different illumination levels, ranging from about 1 to 1500 W/m^2.

All measurements are computer controlled. The control of the measurement equipment, the collection of data, the calculation of the solar cell parameters and most of the data interpretation is handled by a special program called MIA (Measure It All). The program MIA was written in ELIS by Dr. J. Verschraegen [11] and is used not only in *J-V*(*T*) measurements but also for *C-V*(*T*), *C-f*(*T*) measurements. A screen shot of *J-V* curve as calculated by MIA program is shown in Figure 7.

A phenomenological interpretation of the *J-V* measurements is usually done with a two-diode model, which is a straight forward extension of the one-diode model of Eq. (6). Here, the *J-V* characteristics of a solar cell with a

discrete shunt conductance G_{sh} ($1/R_{sh}$) and a discrete series resistance R_s can be written as

$$J = J_{01}\left[\exp\left(\frac{q(V - JAR_s)}{n_1 kT}\right) - 1\right] + J_{02}\left[\exp\left(\frac{q(V - JAR_s)}{n_2 kT}\right) - 1\right] + \frac{G_{sh}}{A}(V - JAR_s) \tag{12}$$

where J_{01}, J_{02} are the saturation current densities, and n_1 and n_2 are the ideality factors associated with the two diodes. From the junction theory the idealization factor amounts to unity (n = 1) for the recombination current in the quasi-neutral regions (diffusion current; ideal Shockley theory) and two (n = 2) for the recombination current in the space charge region.

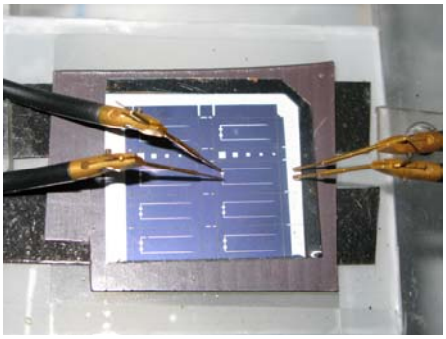

Figure 5 A thin film flexible CIGS solar cell measured using a four-point probe set-up.

The dark *J-V* measurement and Eq. (12) can be used to extract the saturation current densities J_{01} and J_{02}, the ideality factors n_1 and n_2 and the parasitic resistances R_s and G_{sh}. A program called CELLPARAMETERS, developed at ELIS, is used for this purpose. An example of a *J-V* curve fitting is given in Figure 8, showing the results of the relevant parameters extracted from the fitting.

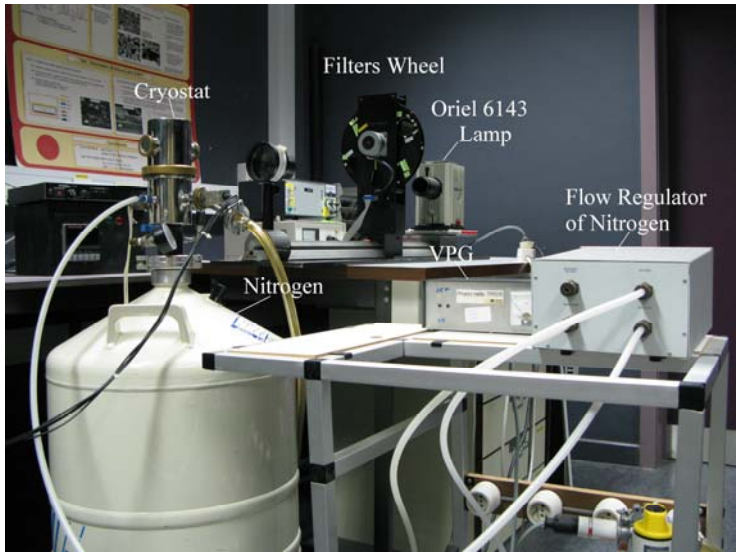

Figure 6 Temperature measurement setup used for *J-V-T*, *C-V-T*, *C-f-T* and J_{sc}-V_{oc}-*T*, where the cell is mounted in the cryostat.

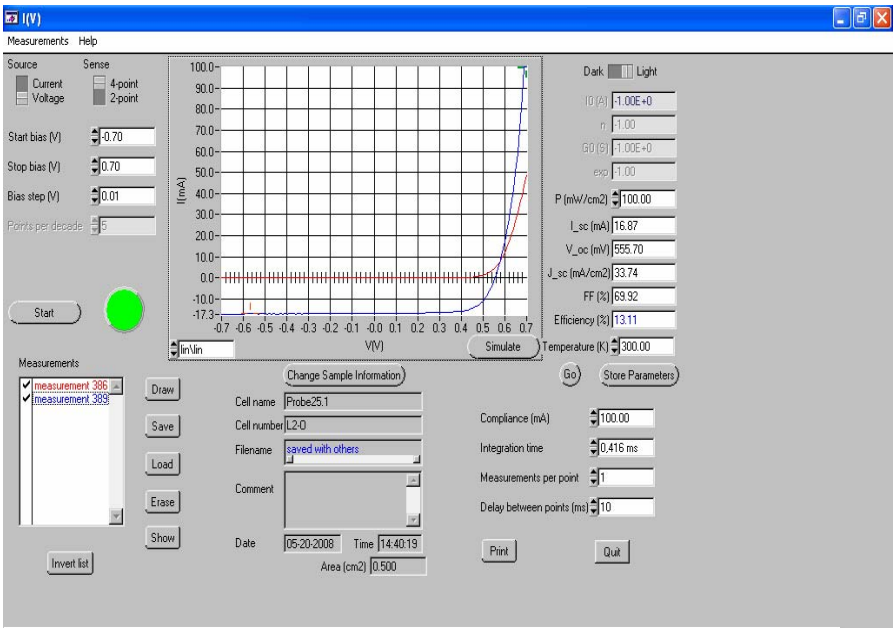

Figure 7 An *I-V* measurement in the MIA measurement and interpretation program used at ELIS.

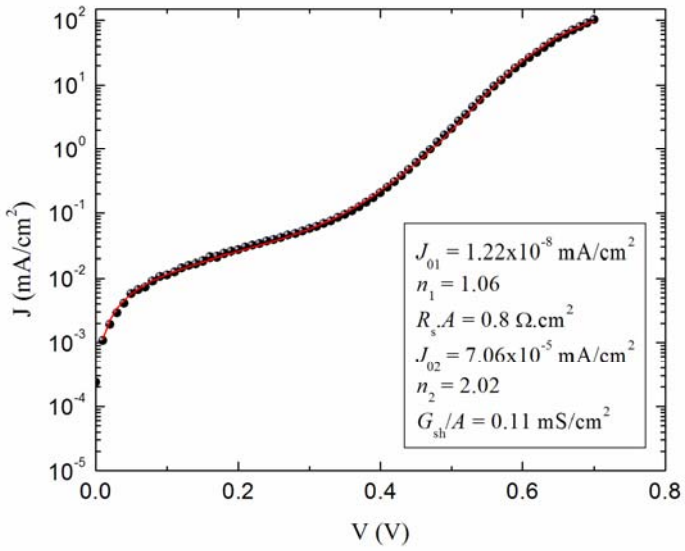

Figure 8 Measured *J-V* dark of a CIGS flexible solar cell. (●) measured points; (solid line) result of fitting with the CELLPARAMETERS program. The insert shows the cell parameters extracted from the fitting.

2.4.2 Quantum efficiency measurement

Quantum efficiency analysis can be used more or less straight forward to determine the band gap E_g of the absorber material; in principle, it can also provide insight in recombination in the device as well. Operationally, the quantum efficiency *QE* is calculated from a measurement of the short circuit current at a given wavelength λ, taking into consideration the power density of the incident radiation.

$$QE = \frac{I_{sc}}{A.P}\frac{hc}{q\lambda} \tag{13}$$

where P is the incident light power and A is the area of the cell, h is Planck's constant and c the velocity of light. Since it is difficult to determine the incident light power, it is necessary to use a reference cell whose response is known. The sensitivity S_{cell} of the solar cell to be measured and S_{ref} of the reference cell are defined by

$$S_{cell} = \frac{I_{sc}\left(\text{cell to be measured}\right)}{P} \text{ and } S_{ref} = \frac{I_{sc}\left(\text{reference cell}\right)}{P} \tag{14}$$

The dimension of the sensitivity S is [A.cm^2/W] = [cm^2/V]. The measured current in the reference cell and in the sample can be expressed as

$$\begin{aligned} I_{ref} &= S_{ref}.\Gamma(\lambda).d\lambda \\ I_{cell} &= S_{cell}.\Gamma(\lambda).d\lambda \end{aligned} \tag{15}$$

where $\Gamma(\lambda)$ is the power spectrum of light intensity [W.cm^{-2}.nm^{-1}] and $d\lambda$ the wavelength bandwidth of the monochromator. The spectral sensitivity S_{ref} of the reference cell has been measured by a calibration institute (JRC, Joint Research Centre of the E.U., Ispra, Italy: courtesy Dr. Ewan Dunlop). The reference measurement (thus the measurement of $I_{ref}(\lambda)$) is carried out at the beginning of every measurement session.

From Eq. (15) we can deduce

$$\frac{I_{cell}}{I_{ref}} = \frac{S_{cell}}{S_{ref}} \tag{16}$$

By extracting S_{cell} from Eq. (16) and substituting in Eq. (13), the quantum efficiency is finally given by

$$QE = S_{ref}.\frac{I_{cell}}{I_{ref}}.\frac{1240 \text{ V.nm}}{\lambda}.\frac{1}{A} \tag{17}$$

where 1240 V.nm is the numerical value of hc/q expressed in convenient units. A schematic diagram of the quantum efficiency measurement set up is shown in Figure 9. The solar cell is illuminated by a halogen lamp via a monochromator; the output of the cell is fed into a current-voltage converting pre-amplifier and is then phase-sensitively detected by a lock-in amplifier. The chopper between the light source and the monochromator serves to modulate the light beam and provides the reference signal to the lock-in amplifier to facilitate phase sensitive detection. Usually, a chopping frequency of 189 Hz is used. Two-point probes are applied to make contact between the measured cell and the measurement set-up.

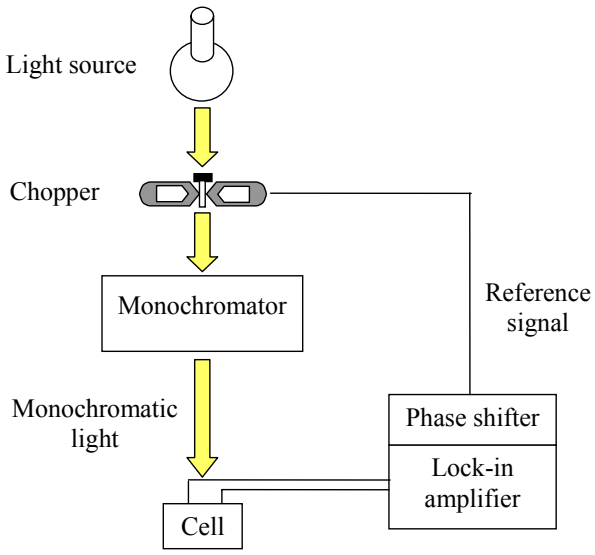

Figure 9 A schematic diagramme of the spectral response measurement setup used in ELIS.

2.4.3 Capacitance-voltage and admittance spectroscopy measurement

In an asymmetrical junction, the depletion layer with width W is situated completely in the weakest doped part of the junction: in a n^+p, this is the p-side. The capacitance is measured by applying a *dc* bias V to widen or shrink the depletion layer W and a superimposed small *ac* signal voltage for probing the actual capacitance at a given bias. Regardless the shallow doping profile $N_A(x)$ in this layer, the relation between depletion layer width and junction capacitance C_j is given by

$$C_j = \frac{\varepsilon_0 \varepsilon_s}{W} \tag{18}$$

where ε_0 is the permittivity of vacuum and ε_s the relative dielectric constant of the p-semiconductor material. When the p-side is uniformly doped, thus when N_A is a constant, C_j is given by

$$C_j = \frac{\varepsilon_0 \varepsilon_s}{W} = \sqrt{\frac{q \varepsilon_0 \varepsilon_s N_A}{2(V_{bi} - V)}} \tag{19}$$

where V_{bi} is the built-in voltage of the cell and V is the applied voltage. At reverse to moderately forward voltage bias, the measured capacitance C is dominated by the junction capacitance. At high forward bias, another contribution to the capacitance, the diffusion capacitance C_d dominates the C-V measurement. The interpretation below is only valid for reverse bias to moderately forward bias voltage.

A plot of $1/C^2$ versus V is called Mott-Schottky plot. In a uniformly doped junction, it takes the form

$$\frac{1}{C_j^2} = \frac{2\left(V_{bi} - V\right)}{q\varepsilon_0\varepsilon_s N_A} \tag{20}$$

Equation (20) describes a straight line in the Mott-Schottky plot. The intersection of this line with the voltage axis gives the junction built-in voltage V_{bi}.

The (negative of the) slope determines the acceptor density of the diode (the absorber of the cell).

In real C-V measurements, deviations from a straight line are frequently observed. An obvious cause of such deviation is a non-uniform doping distribution $N_A(x)$ in the weakly doped p-layer. Fortunately, Eq. (20) can be generalized for any doping profile $N_A(x)$:

$$\frac{d\left(1/C_j^2\right)}{dV} = -\frac{2}{q\varepsilon_0\varepsilon_s N_A\left(W\right)} \tag{21}$$

where the relation between W and C_j is given by Eq. (18) at every voltage. The equations (18) and (21) are thus used to derive a doping profile $N_A(W)$ from a C-V measurement.

Considering further inhomogeneous doping capacitance dependence on the reverse voltage, Eq. (19) may be written as:

$$C_j = \frac{C_0'}{\left(1 - \frac{V}{V_{bi}}\right)^{\frac{1}{\beta}}} \tag{22}$$

When the doping is uniform $\beta = 2$ and when there is a doping gradient with position, $\beta \neq 2$. The parameter β can be used as a measure of the non-uniformity of the doping density.

Thin film solar cells most often contain defects or impurities, with an energy level deep in the forbidden gap. In dc, the occupation and hence ionization state of a deep defect will change with applied dc-bias voltage. When the frequency of the ac-signal used to measured the capacitance is low enough, the deep state will adapt its ionization state also with the ac-signal, and hence contribute to the measured capacitance. When the frequency of the ac-signal is too high, the deep defect will not adapt its ionization state to the ac-signal, and hence not contribute to the measured *C*. It follows that the junction capacitance will show a dependence on the measurement frequency, which is not taken into account in Eq. (18).

In this case, the measured capacitance-frequency dependence $C(\omega)$ is given by

$$C(\omega) = C_j + C_t(\omega) \tag{23}$$

where C_j is the frequency-independent depletion capacitance and $C_t(\omega)$ is the frequency-dependent contribution of the deep trap levels to the capacitance.

An example of such frequency-dependent capacitance curves, measured at different temperatures, is given in Figure 10.

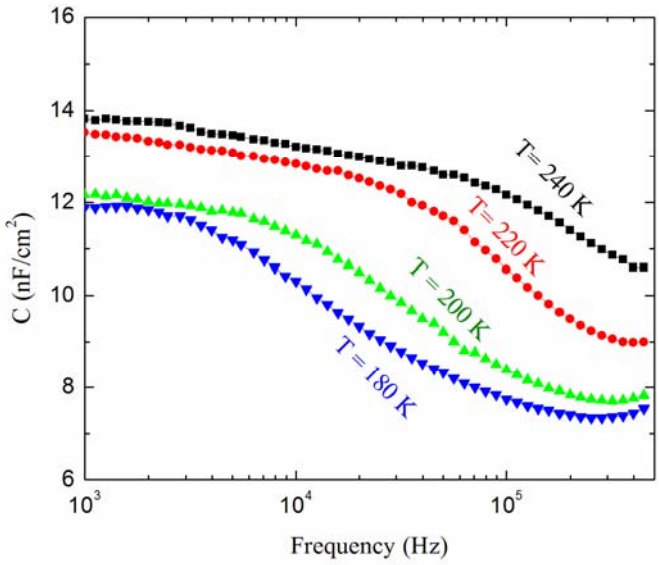

Figure 10 Capacitance-frequency measured at different temperature of a flexible thin film CIGS solar cell on steel foil substrate.

The contribution of one single defect level to the capacitance can be described by a relaxation process [12]

$$C(\omega) = C_{hf} + \frac{1}{1+\omega^2\tau^2}\left(C_{lf} - C_{hf}\right) \tag{24}$$

The high frequency capacitance C_{hf} is the depletion capacitance. The low frequency capacitance C_{lf} is the combined contribution of the deep defect and the depletion capacitance: the contribution of the trap is thus given by C_{lf}- C_{hf}, and the dynamics of the trap is described by the time constant τ. When the measured *C-f* curve has a step-like character, the quantities C_{lf}, C_{hf} and τ can be extracted from the measurement. An obvious cause for a non-step like *C-f* behaviour is the presence of two or more traps, or a distribution of the energy position of the traps in a band. The interpretation of the more complicated case is treated below in section 2.4.4.

The consideration of traps located at the interface results in additional interface state capacitance C_s which is also frequency dependent [13]:

$$C(\omega) = C + \frac{C_s}{1+\omega^2\tau_s^2} \tag{25}$$

where C is the contribution of the bulk and the second term of Eq. (25) the contribution of the interface. The density of interface states N_s can be obtained by:

$$N_s = \frac{C_s}{q} \tag{26}$$

It is however obvious that it is at this point not possible to attribute a frequency-dependent *C-f* behaviour to bulk states (Eq. (24)) or to interface states (Eq. (25)). In cases, the (dc) voltage dependence of the *C-f* curve, together with specific assumptions can allow to discriminate between bulk and interface effects [13].

When capacitance measurements, leading to a *C-f* curve, are complemented with conductance measurements, leading to a *G-f* curve, the technique is called impedance spectroscopy (IS) or admittance spectroscopy (AS). There exist many ways to represent IS or AS measurements: *C-f* and *G-f* curves (used here), Bode plots of admittance ($\log|Y|$ vs. $\log(f)$; $\arg(Y)$ vs. $\log(f)$) or impedance, Nyquist plots ($\mathrm{Im}(Z)$ vs. $\mathrm{Re}(Z)$), and to interpret these measurements (e.g. network representations, including dedicated network elements as the constant phase element *CPE* or the Warburg element *W*). We

will primarily use an interpretation of the C vs. log(f) measurement, see below, section 2.4.4.

In ELIS, capacitance-voltage and admittance spectroscopy measurement are performed using a HP 4192A LF impedance analyzer (5 Hz-13 MHz). A picture of the set up is displayed in Figure 11.

Figure 11 Setup of *C-V* and *C-f* measurement used at ELIS.

2.4.4 Defect investigation

In a measurement, the time constant τ (in Eq. (24)) is deduced from the angular frequency ω_I of the inflection point of the $C(\omega)$ curve: $\tau = 1/\omega_I$. In a p-type material, hole traps can be charged and discharged at frequencies $\omega < \omega_t$. In the limit of small trap concentrations $N_t << N_A$ this 'inflection frequency' ω_I is given by

$$\omega_I = 2v_{th}\sigma_p N_V \exp\left(-\frac{E_T - E_V}{kT}\right) = A\exp\left(-\frac{E_A}{kT}\right) \tag{27}$$

where E_T is the trap energy, kT the thermal energy, σ_p the hole capture cross section, v_{th} the thermal velocity of holes, N_V the effective density of states in the valence band, and E_A the apparent activation energy of ω_I and τ. Of course this interpretation can only be applied when the *C-f* measurements show a clear step between a *LF* and a *HF* plateau value as it is more or less the case in Figure 10. In this case, an Arrhenius plot of Eq. (27) can be used to determine the activation energy of the trap.

A gradual decay of the *C-f* curves over an extended frequency range can be caused by a distribution of defects in the semiconductor. The analytical calculation of the capacitance spectrum for a semiconductor with more than one trap level or a distribution of traps requires a more complex theory [14]. Walter et *al*. [15] developed an analytical model which allows to determine the energetic distribution of defects $N_T(E)$ from the measured capacitance data $C(\omega,T)$ using differentiated capacitance spectra:

$$N_t(E_\omega) = -\frac{V_{bi}}{qW}\frac{dC}{d\omega}\frac{\omega}{kT} \tag{28}$$

which can be also written as

$$N_t(E_f) = -\frac{V_{bi}}{qkT}\cdot\frac{C}{\varepsilon_0\varepsilon_s}\cdot\frac{dC}{d(\log f)} \tag{29}$$

V_{bi} is the built-in voltage and W is the width of the space charge region of the junction.

The local derivative $dC/d(\log(f))$ is proportional to the density of defect states N_t (in $cm^{-3}.eV^{-1}$), and the energy position E of the defect state is proportional to $\log(f)$.

It is important to note that this model gives a useful visualization of energetic distribution of trap states for the case of small trap densities $N_t(E) < N_A$.

The analysis and interpretation of *C-V* curves and *C-f* curves along the lines explained above is greatly facilitated by the software tool PIA (Plot it all). Some basic facilities are directly available from the measurement program MIA. Sometimes parasitic effects (R_s and R_{sh}) can obscure the interpretation of the *C-f* measurement. Advanced data processing still allows the determination of defect levels and densities in that case (when R_s and R_{sh} are not too severe) [16].

Chapter 3

IPV effect in Si and GaAs Solar Cells

3.1 Introduction

The impurity photovoltaic effect (IPV) has attracted much attention as an approach to improve solar cell performance by introducing sub-band gap absorption mechanisms [17][20]. It can be exploited by intentionally adding impurities, acting as defect levels lying deeply within the forbidden gap. Photons having energies below the band gap E_g of the host material, can excite electrons and holes from the defect to the conduction and valence band, respectively, thereby increasing the short circuit current J_{sc} of the solar cell: this is called IPV effect. It is however also recognized that the deep defect states also act as recombination centres and hence reduce the open circuit voltage V_{oc} [18].

A significant amount of theoretical work has been carried out on IPV effect in the literature, particularly on silicon solar cells with indium impurities as defect. In 1994, Keevers and Green [18] presented a theoretical study of the IPV effect where one optical impurity process was combined with effective light trapping. They studied a silicon solar cell with a large density of indium impurities, which produce a relatively deep acceptor level at 157 meV above the valence-band edge. They showed that an efficiency increase of 1 % to 2 % absolute could be obtained. In a numerical study of the IPV effect, Schmeits and Mani [19] confirmed that an improvement of silicon solar cell

performances is possible by choosing a *p-n-n* $^+$ structure solar cell. Other theoretical calculations show that the IPV effect is more attractive for solar cells with larger band gap materials [20].

In this chapter new results [21][22][23] obtained for the IPV effect in silicon and gallium arsenide solar cells will be presented using the software SCAPS [4], which was extended to include this effect.

3.2 The IPV effect and its SCAPS implementation

The lack of an easily available solar cell simulator including the IPV effect is a handicap. For this reason, the numerical solar cell simulator SCAPS of the ELIS group was extended to include IPV. SCAPS is a one dimensional solar cell device simulator, developed at ELIS, University of Gent, which is freely available to the PV research community. The user can define a solar cell as a series of layers with different properties, such as: thickness, doping densities and defect distribution. It is then possible to simulate a number of common measurements: *I-V*, *QE*, *C-f*, *C-V*. In a joint ELIS/LPDS study, a new version of SCAPS was developed which takes into account the IPV effect. The main new features being implemented in this SCAPS version are:

1. The occupation probability of the defects depends on their optical capture cross section for electrons and holes.
2. The optical absorption coefficient accounts for photoemission electrons and holes from the IPV impurity, and hence becomes position dependent.
3. The optical capture cross sections are either taken from a file or calculated analytically according to a model by Lucovsky [24].
4. A simple light trapping scheme has been implemented.

The model of Lucovsky to calculate the optical cross section of an impurity $\sigma_{n,p}^{\text{opt}}$ needs the input of five parameters: refractive index n of the semiconductor, the effective mass m_n^* and m_p^* of the carriers, the ionization energy of the defect E_i (E_C - E_t for electrons and E_t - E_V for holes) and the effective field ratio E_{eff}/E_0 which represents the ratio between the electric field at the impurity and the electric field of the incident wave. The analytical expression of $\sigma_{n,p}^{\text{opt}}$ takes then the form [24]:

$$\sigma_{n,p}^{\text{opt}}(\hbar\omega) = \frac{1}{n}\left(\frac{E_{eff}}{E_0}\right)^2 \frac{16\pi q^2\hbar}{3m_{n,p}^* c}\frac{(E_i)^{1/2}(\hbar\omega - E_i)^{3/2}}{(\hbar\omega)^3} \tag{30}$$

In the IPV effect, the presence of a deep state within the energy gap adds two impurity optical transitions to the traditional Shockley-Read-Hall recombination model (SRH, e.g. [7]). As illustrated in Figure 12, electron and hole transition through the impurity is governed by capture, thermal and optical emission of carriers. The net recombination rate U via the impurity is given by [18]:

$$U = \frac{np - (n_1 + \tau_{n0}g_{nt})(p_1 + \tau_{po}g_{pt})}{\tau_{no}(p + p_1 + \tau_{p0}g_{pt}) + \tau_{po}(n + n_1 + \tau_{n0}g_{nt})} \tag{31}$$

with

$$\tau_{n0} = \frac{1}{c_n N_t} \text{ and } \tau_{p0} = \frac{1}{c_p N_t} \tag{32}$$

$$n_1 = N_C e^{-(E_C - E_t)/kT},\ p_1 = N_V e^{-(E_t - E_V)/kT} \tag{33}$$

$$g_{nt} = N_t \int_{\lambda_{n\min}}^{\lambda_{n\max}} \sigma_n^{opt}(x,\lambda)\phi_{ph}(x,\lambda)d\lambda \tag{34}$$

$$g_{pt} = N_t \int_{\lambda_{p\min}}^{\lambda_{p\max}} \sigma_p^{opt}(x,\lambda)\phi_{ph}(x,\lambda)d\lambda \tag{35}$$

$$\phi_{ph}(x,\lambda) = \phi_{ext}(\lambda)\frac{1 + R_b e^{-2\alpha_{tot}(\lambda)(L-x)}}{1 - R_f R_b e^{-2\alpha_{tot}(\lambda)L}} e^{-\alpha_{tot}(\lambda)x} \tag{36}$$

In Eq. (31), n and p are the electron and hole concentrations, τ_{n0} and τ_{p0} are the SRH lifetimes for electrons and holes, c_n and c_p are the electron and hole thermal capture cross sections, N_t is the impurity concentration, and E_t is the impurity level energy. The electron and hole concentrations n_1 and p_1 in Eq. (33) are calculated with the Fermi level coinciding with the impurity level, E_C and E_V are the conduction and valence band edges, and N_C and N_V are the effective densities of states in the conduction and valence bands.

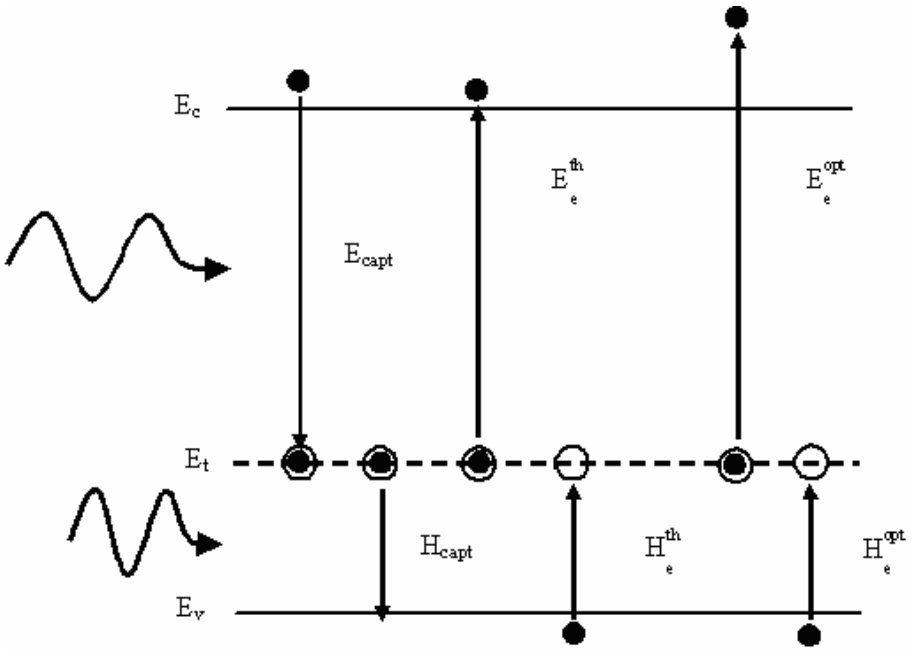

Figure 12 The carriers transitions of the modified SRH recombination model. E_{cap} and H_{cap} are the electron and hole capture, E_e^{th} and H_e^{th} are the electron and hole thermal emission respectively. E_e^{opt} and H_e^{opt} are the electron and hole photoemission.

The optical emission rates from the impurity, g_{nt} for electrons and g_{pt} for holes constitute the IPV extension to the normal SRH expression. In Figure 12, these processes are indicated as E_e^{opt} and H_e^{opt}, respectively. Eq. (31) takes into account that the impurity should be fully occupied for the optical electron emission process (E_e^{opt} with optical cross section $\sigma_n^{opt}(\lambda)$) and completely empty for the optical hole emission process (H_e^{opt} with optical cross section $\sigma_p^{opt}(\lambda)$) [18].

Eqs. (34) and (35) are given for a normal incident light, without considering the increase of the optical path length by Lambertian or other scattering at the surfaces [18]. The external incident photon flux is $\phi_{ext}(\lambda)$ and spectral distribution of the photon flux at distance x from the illuminated surface is noted as $\phi_{ph}(x,\lambda)$. In Eq. (36), L is the total length of the solar cell, and R_f and R_b are the internal reflection coefficients at the front and back of the cell,

respectively. Setting R_f and R_b equal to zero corresponds to a solar cell without internal reflection, while a maximum (but unphysical) internal reflection is obtained by setting R_f and R_b equal to unity.

In SCAPS the parameters R_b and R_f are used to describe empirically light trapping without getting into the details of how this light trapping is achieved.

The total absorption coefficient is the sum of all absorption processes in the cell:

$$\alpha_{tot}(\lambda) = \alpha_{e-h}(\lambda) + \alpha_n(\lambda) + \alpha_p(\lambda) + \alpha_{fc}(\lambda) \tag{6}$$

where $\alpha_{e\text{-}h}(\lambda)$ the band-to-band absorption coefficient, and $\alpha_n(\lambda)$ and $\alpha_p(\lambda)$ are the defect absorption coefficients given by:

$$\alpha_n(\lambda) = f_t N_t \sigma_n^{opt}(\lambda) \text{ and } \alpha_p(\lambda) = (1 - f_t) N_t \sigma_p^{opt}(\lambda) \tag{37}$$

with f_t is the occupation probability of the impurity level. The free carrier absorption $\alpha_{fc}(\lambda)$ is given by [25]

$$\alpha_{fc}(\lambda) = C_{fc}^n \lambda^2 n + C_{fc}^p \lambda^2 p \tag{38}$$

where C_{fc}^n and C_{fc}^p are empirical parameters.

In this study, we considered only band to band absorption $\alpha_{e\text{-}h}(\lambda)$ and the defect absorption $\alpha_n(\lambda)$ and $\alpha_p(\lambda)$; free carrier absorption are not yet implemented in SCAPS. It should be noted that this absorption process is important in heavily doped semiconductors, and does not create electron-hole pairs so it gives no contribution to the photocurrent.

3.3 The IPV effect in silicon solar cell

To test the validity of the new SCAPS version, we first checked the results of [19], and we found a good agreement. In the next step, we studied the influence of the indium defect concentration and light trapping on the photovoltaic parameters of the cell.

Our structure is a crystalline silicon p^+nn^+ solar cell, where the indium impurity concentration is zero in the n^+ layer. The corresponding thicknesses and shallow doping densities of the layers are respectively (2 μm, $N_A = 10^{18}$ cm^{-3}), (100 μm, $N_D = 10^{17}$ cm^{-3}) and (20 μm, $N_D = 10^{18}$ cm^{-3}).

The parameters characterizing Si and the indium impurity at 300 K are summarized in Table 2. To calculate the electron and hole photoemission cross sections of the impurity, we used both the models presented in [18] and the model of Lucovsky [24]. Note that all are assumed zero for photons of energy above the band gap. Free carrier absorption was not included into the model. In this numerical study, we varied indium concentration N_t, and the light trapping parameters R_f and R_b.

Table 2 Silicon and indium impurity parameters used in this study (at 300 K) [18][19].

Property	Symbol	Value	Unit
Energy gap	E_g	1.12	eV
Electron mobility	μ_n	1350	cm^2/Vs
Hole mobility	μ_p	480	cm^2/Vs
Dielectric constant	ε_s	11.7	
Surface recombination velocity	$v_{sn} = v_{sp}$	$10\text{-}10^4$	cm/s
Indium energy level from the top of the valence band	$E_t - E_V$	0.157	eV
Defect type		acceptor	
Electron thermal capture cross section	σ_n^{th}	1.0×10^{-22}	cm^2
Hole thermal capture cross section	σ_p^{th}	5.07×10^{-15}	cm^2

3.3.1 Validation of the numerical model

In Figure 13 we show the current–voltage characteristics for the p^+nn^+ structure with $N_t = 10^{17}cm^{-3}$ in the p^+ and n region. Our SCAPS simulations (Figure 13a) are compared with the result calculated in [19] (Figure 13b). In both Figure 13a and b, ideal light trapping ($R_b = R_f = 1$) is assumed in curves a and b, while more realistic values $R_b = 0.97$ and $R_f = 0.93$ are assumed in curves (c) and (d). In curves (b) and d the optical generation via In impurities are switched off, but they can still contribute to the net doping and to the recombination. The curves (e) correspond to the case where there is no In at all in the cell. We noticed a good agreement between our results (Figure 13a) and those of [19] (Figure 13b). The IPV effect clearly increases J_{sc} (compare curves (a) with (b), and (c) with (d)), but this advantage is appreciable only when ideal light trapping is assumed (compare curves (a) to (c)).

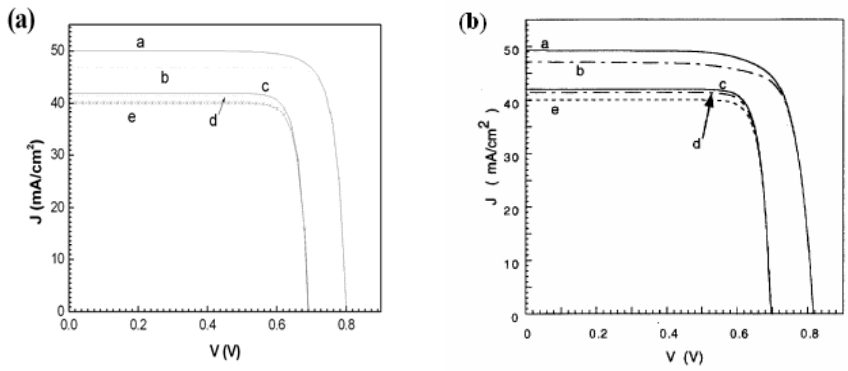

Figure 13 Current-voltage characteristics for the p^+nn^+ silicon solar cell with In impurity concentration $N_t = 10^{17}\text{cm}^{-3}$. (a) Results calculated with SCAPS (this work); (b) Results calculated in [19]. In both (a) and (b), curves a and b are for $R_b = R_f = 1$, curves c and d are for $R_b = 0.97$, $R_f = 0.93$. For b and d, the electron and hole optical generation rates are switched off. In curves e indium concentration is set to zero.

In Figure 15 the infrared response of the silicon cell is presented using two different models to calculate the optical cross sections $\sigma_n^{opt}(\lambda)$ and $\sigma_p^{opt}(\lambda)$ of the indium impurity, based on measurements [18] or calculated with the Lucovsky model [24]. A small difference was observed for long wavelengths λ >1.1 μm. Figure 2.3b show the spectral response calculated for four different cases: cell without indium impurity, fully optically active or not. "Fully optically active" means $\sigma_n^{opt}(\lambda)$ and $\sigma_p^{opt}(\lambda)$ from measurements in [18], and "not fully optically active" means either $\sigma_n^{opt}(\lambda) = 0$ or $\sigma_p^{opt}(\lambda) = 0$. Two general conclusions can be deduced from these figures: (i) indium incorporated in the cell improves the sub-gap spectral response, and (ii) the generation current due to In impurity is governed by the slowest optical process which is the indium to conduction band transition described by $\sigma_n^{opt}(\lambda)$.

3.3.2 The effect of indium concentration

Figure 15 shows the effect of indium impurity concentration N_t on the photovoltaic parameters: open circuit voltage V_{oc}, photocurrent density J_{sc} and the efficiency η.

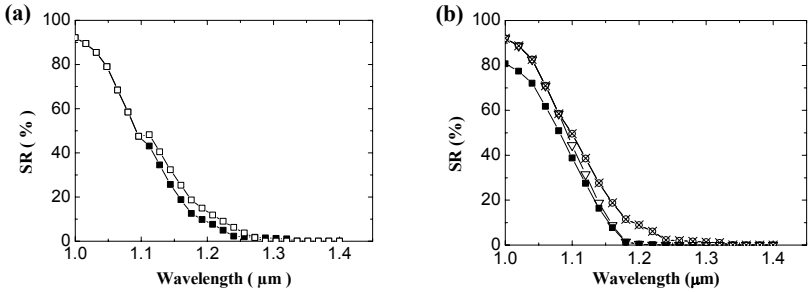

Figure 14 Spectral response calculated with SCAPS of p^+nn^+ Si cell. Base doping $N_D = 10^{17}$ cm^{-3}, indium impurity concentration $N_t = 10^{17}$ cm^{-3}. (a) Optical cross sections from measurements [18] (■) or from the Lucovsky model [24] (□); (b) without (■) and with indium impurities: fully optically active (○), or only emission of electrons to the conduction band (×) or of holes to the valence band (▽).

Both J_{sc} and η increase with increasing N_t when $N_t \leq N_D$ and decrease above this concentration. An In concentration N_t lower than the base concentration N_D keeps the indium level fully occupied which allows sub-band gap photons to be absorbed by the electron photoemission process (from the In level to the conduction band). When indium concentration compensates the base doping ($N_t > N_D$), the hole photoemission process (from the In level to the valence band) is maximized. It competes with the first photoemission process and also with electron-hole pair creation by intrinsic band to band absorption which reduces the available photon flux and photocurrent of the cell. The open circuit voltage also decreases while maintaining reasonable values.

The p^+nn^+ structure has the advantage to keep a high value for the built-in voltage and thereafter keep the indium level occupied due to the presence of the n^+ layer. In addition, this layer introduces a back surface electric field which improves the cell electric characteristics, particularly the open circuit voltage by reducing the recombination current. Note that it is difficult to shift the condition $N_t = N_D$ for maximal IPV effect to higher values: first, N_D should not exceed about 10^{18} cm^{-3} to prevent band gap narrowing and a shift of intrinsic band to band absorption to lower energies [26], second, N_t is limited because the maximum solid solubility of indium in silicon which is about 10^{18} cm^{-3} [27].

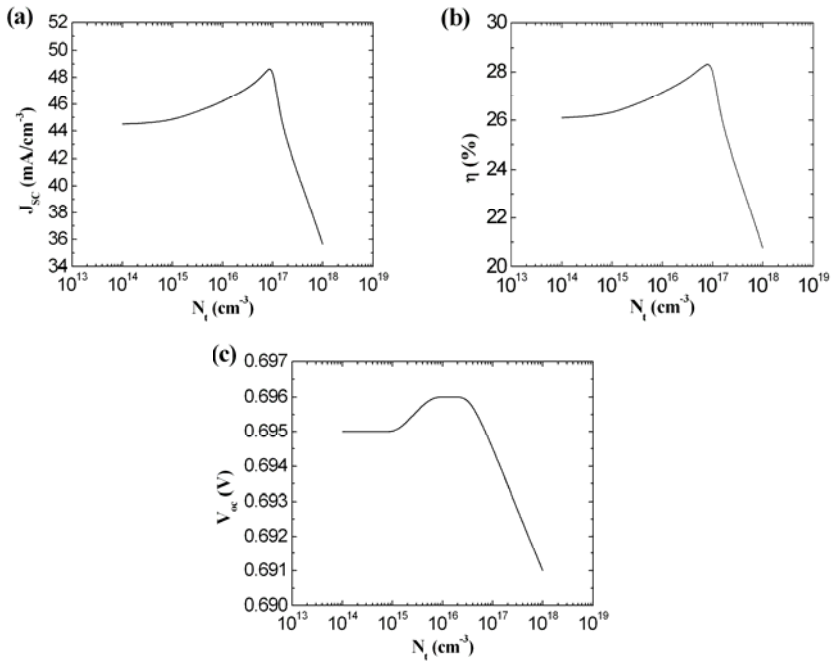

Figure 15 Photovoltaic parameters of a silicon solar cell as a function of indium concentration, (a) Short circuit current density, (b) Efficiency, (c) Open circuit voltage.

3.3.3 The effect of light trapping

The importance of light trapping in IPV cells was suggested for the first time by Keevers and Green [18]. Light trapping increases the opportunity for photons to be absorbed by weak optical processes in a cell, such as the rate limiting electron photoemission process from the indium level.

In a silicon solar cell with a randomising top surface, a perfect antireflection coating and a planar back surface of reflectivity R_b, the degree of light trapping is adjusted by the value of R_b. Setting $R_b = 0$ corresponds to no light trapping, however a perfectly back surface reflectivity is obtained by setting $R_b = 1$. Note that a reflectivity close to unity in the back surface of a silicon solar cell has been measured experimentally [26].

To examine how much light trapping affects the IPV effect and improves sub-band gap absorption in the solar cell, we show in Figure 16 the $J_{sc}(N_t)$ and $\eta(N_t)$ curves with ($R_b = 1$) and without ($R_b = 0$) light trapping. We see that light trapping increases the photocurrent by about 6 mA/cm^2, and the

efficiency by about 2 % (absolute) at the optimum indium concentration N_t = 10^{17} cm^{-3}. This improvement is due to the enhancement of the IPV effect by improving long-wavelength absorption, as can be seen in Figure 17 in which we observed an extension of the infrared response into the sub-band gap wavelength region, especially between λ = 1100 nm and λ = 1350 nm.

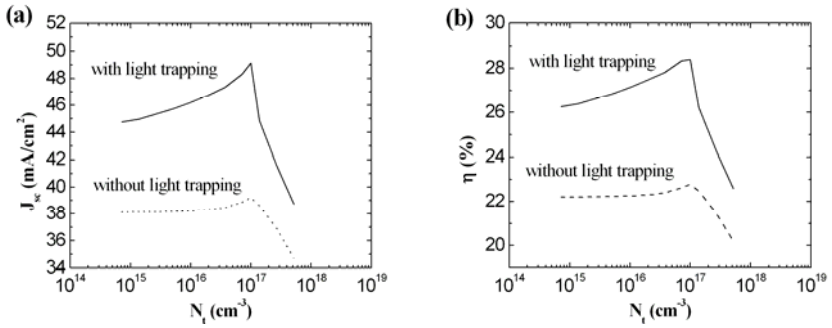

Figure 16 Effect of light trapping on the IPV effect, (a) Short circuit current improvement, (b) Efficiency improvement, with N_t = 10^{17} cm^{-3}.

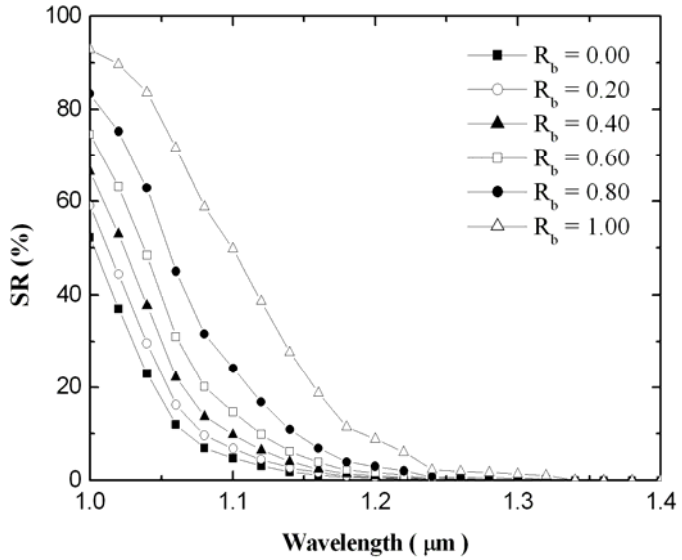

Figure 17 Effect of light trapping on sub-band gap spectral response with N_t = 10^{17} cm^{-3}

A good internal reflection R_f at the front of the cell is also necessary to obtain a significant IPV effect. In Figure 18 we show the absolute increase which could be obtained for the solar cell efficiency as a function of the reflection coefficients at the front and the back of the cell, R_f and R_b respectively. Values approaching the unity are necessary for R_f and R_b otherwise no significant efficiency increase is obtained.

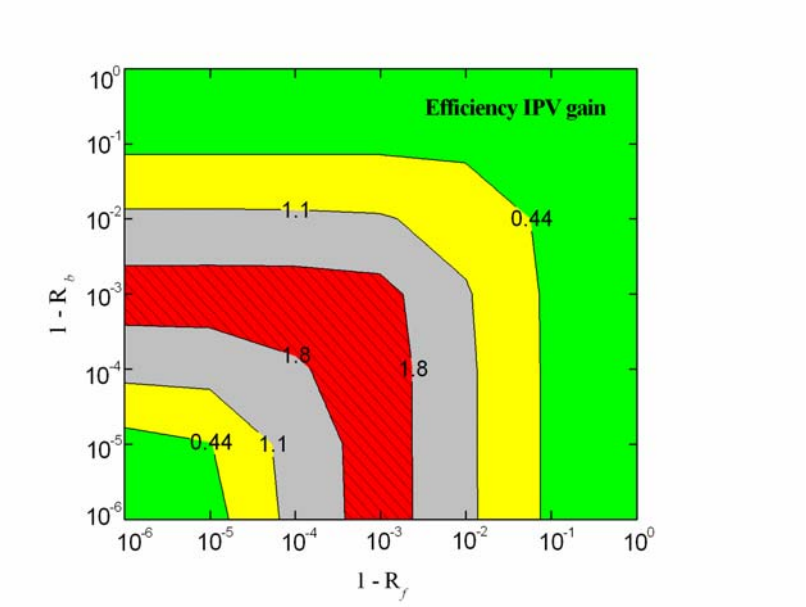

Figure 18 Absolute efficiency gain (in %) as a function of front and back surface reflectivity, R_f and R_b respectively, with $N_t = 10^{17}$ cm^{-3}.

3.4 The IPV effect in a GaAs solar cell

In order to exploit the potential of the IPV effect, one has to study wide-band gap semiconductors, since it is predicted to be more pronounced in such materials, and possibly also by introducing more than one impurity level. For this purpose, we carried out a numerical study on GaAs solar cells with copper impurities. Copper impurities in GaAs introduce several more or less deep acceptor states with reported energy levels of (0.13 to 0.15) eV, 0.24 eV and (0.40 to 0.49) eV above the valence band edge [28][29][30], however the exact structure of these levels are not known [30]. The current-voltage

characteristics *J-V* and the internal quantum efficiency $QE(\lambda)$ are calculated and the influence of some determining parameters is discussed.

We investigated the influence of the density of the Cu-defects and the light trapping on parameters of the solar cell structure. The contribution of the various Cu levels is assessed by considering all combinations of two of the defects, and then studying the effect of the most efficient couple of defects in more detail.

The GaAs solar cell structure is the same as for the Si solar cell (p^+-n-n^+), in which Cu impurities are incorporated in the base region. We assume that the base region contains both a shallow background donor type dopant as well as the acceptor type IPV impurity copper. Also finite surface recombination velocities for electrons and holes are assumed. The doping concentration and the thicknesses of the different layers are, if not stated else, as follows: $N_A = 10^{18}$ cm^{-3}, d = 0.5 µm for the p^+ layer; $N_D = 10^{17}$ cm^{-3}, d = 3.5 µm for the n-base layer and $N_D = 10^{18}$ cm^{-3}, d = 2 µm for the n^+ layer. The parameters used in the simulation are given in Table 3.

We used the model of Lucovsky [24] to calculate the optical cross sections for electrons and holes. The absorption coefficient $\alpha_{e\text{-}h}(\lambda)$ for gallium arsenide is taken from [40]. The solar cell is assumed to be operating under global AM1.5 illumination and a temperature of 300 K. Light trapping is incorporated with a substantial effect, which corresponds to internal reflection at the back and the front close to unity. The importance of free carrier absorption was estimated a posteriori in Figure 19, where the calculated IPV contributions α_n and α_p to the total absorption are compared to the literature data of the band-to-band and free carrier absorption. It is seen that α_{fc} does not significantly contribute to α_{tot} in the entire wavelength range under consideration.

3.4.1 Effect of impurity defect concentration

In this section, we assume that the band gap of the base layer contains only the Cu(B) defect level, and we calculate the solar cell parameters as function of the impurity concentration for different base doping concentration $N_D = 10^{16}$, 3×10^{16} and 10^{17} cm^{-3}. Figure 20 shows the short circuit current density, efficiency and open circuit voltage of the solar cell respectively, as a function of the Cu(B) concentration N_t. The short circuit current density and efficiency increase with increasing N_t only when $N_t \leq N_D$.

Table 3 GaAs and copper parameters used in simulation at K = 300 K.

Property	Symbol	Value	Unit	Ref.
GaAs band gap energy	E_g	1.42	eV	[31]
Dielectric constant	ε_r	13.18		[32]
Electron mobility	μ_n	4600	cm^2/Vs	[32]
Hole mobility	μ_p	239	cm^2/Vs	[32]
Electron effective mass	m_n^* / m_o	0.063		[31]
Hole effective mass	m_n^* / m_o	0.45		[31]
Refractive index	n	3.3		[31]
Surface recombination velocity	$S_n = S_p$	10^4	cm/s	[33][34]
Cu(*A*) defect level				
Energy level above E_v	$E_t(A)$-E_V	0.14	eV	[32][35]
Electron capture cross section	$\sigma_n^{th}(A)$	$\leq 10^{-20}$	cm^2	[36][37]
Hole capture cross section	$\sigma_p^{th}(A)$	1.20×10^{-17}	cm^2	[35]
Cu(*B*) defect level				
Energy level above E_v	$E_t(B)$-E_v	0.40	eV	[38][39][29] [29][37]
Electron capture cross section	$\sigma_n^{th}(B)$	$\leq 10^{-20}$	cm^2	[36][37]
Hole capture cross section	$\sigma_p^{th}(B)$	6.30×10^{-15}	cm^2	[38][29]
Cu(*C*) defect level				
Energy level above E_v	$E_t(C)$-E_v	0.24	eV	[28][32]
Electron capture cross section	$\sigma_n^{th}(C)$	10^{-22}	cm^2	
Hole capture cross section	$\sigma_p^{th}(C)$	2.70×10^{-16}	cm^2	

As it was shown in the previous section, since the generation current due to IPV effect is governed by the slowest optical process ($\sigma_n^{opt}(\lambda)$ in this case), impurity defect level not fully occupied increase transition rate from the valence band to the defect level, which reduces the photon flux available for the electron photoemission process. The open circuit voltage decreases but by keeping moderate values with increasing impurity concentration. In practice, there are limits to the application of high copper concentrations to obtain a substantial IPV effect.

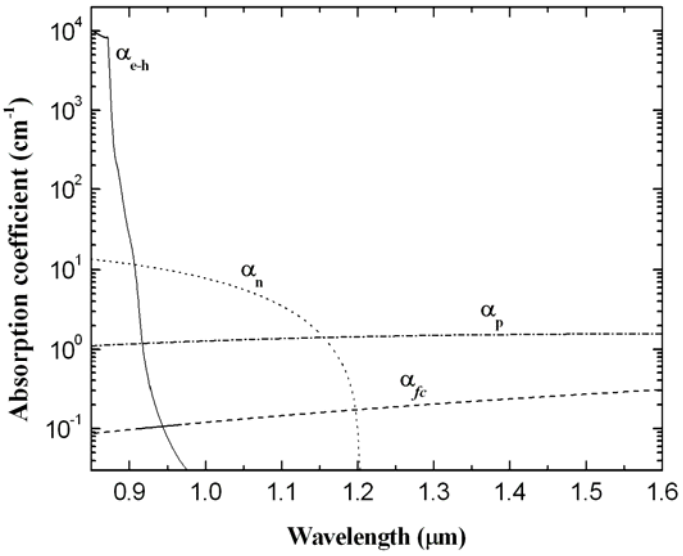

Figure 19 Optical absorption coefficient as a function of wavelength calculated with the *Cu*(*B*) level and for $N_D = N_t(B) = 10^{17}\text{cm}^{-3}$ and $1\text{-}R_f = 10^{-3}$ and $1\text{-}R_b = 10^{-4}$. $\alpha_{e\text{-}h}$ is the band-to-band absorption coefficient, α_n defect to conduction band absorption coefficient, α_p valence band to defect level absorption coefficient and α_{fc} free carrier absorption coefficient.

It was established that for low copper concentrations, the GaAs base semiconductor remains *n*-type and conducting, but turns to *p*-type at high Cu concentrations due to a compensation effect. Also, the density of the Cu impurities is effectively limited by the solid solubility of Cu in GaAs, which is about $5\times10^{16}\,\text{cm}^{-3}$ [35]. Finally, it is worth noting that at impurity concentrations exceeding 10^{17} cm^{-3} the SRH formalism as used here becomes inaccurate due to the onset of degeneration and other heavy doping effects.

3.4.2 Effect of light trapping

As discussed above, in our model all effects of the optical management of the cell are incorporated in the values of the internal reflection R_f at the front and R_b at the back of the cell. The effect of these reflection parameters on the short circuit current is illustrated in Figure 21.

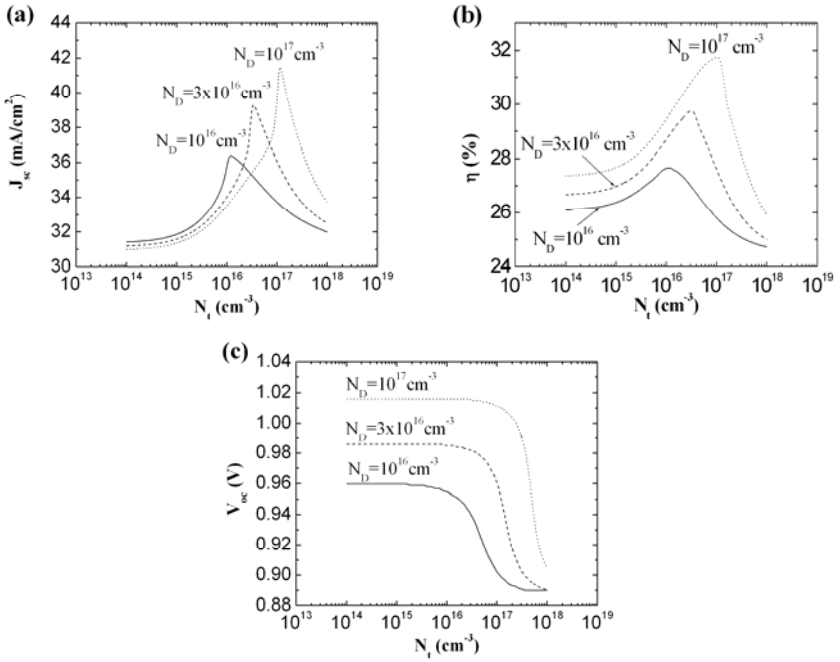

Figure 20 Solar cell parameters of an IPV GaAs solar cell as a function of the *Cu*(*B*) impurity concentration N_t calculated for $N_D = 10^{17}$ cm^{-3}. The internal reflections are set to $1\text{-}R_f = 10^{-3}$ and $1\text{-}R_b = 10^{-4}$ (a) short circuit current density J_{sc}; (b) conversion efficiency η; and (c) open circuit voltage V_{oc} .

It is evident that the maximum IPV effect (a J_{sc} gain of $\Delta J_{sc} \cong 9$ mA/cm^2 with the parameters of Figure 20) is only obtained for unphysical values $R_f = R_b = 1$. Nevertheless, a substantial IPV effect of e.g. ΔJ_{sc} exceeding 2 mA/cm^2 can already be obtained at a high value of the reflection coefficients, R_f and $R_b > 0.99$. It is also verified in Figure 20 that when no IPV effect is taken into account, the effect of a high value of R_f and R_b is very marginal: $\Delta J_{sc} = 7$ μA/cm^2 only.

Figure 22 compares the current-voltage curve of the IPV GaAs solar cell for $N_t = 3\times10^{16}$ cm^{-3}, with and without light trapping, respectively. With the parameters of Figure 22, the IPV effect with light trapping results in a J_{sc} gain of about $\Delta J_{sc} = 6$ mA/cm^2 without any appreciable loss of V_{oc} or *FF*.

The potential benefits of light trapping in GaAs solar cells can be summarized in the three following features:

Increase optical absorption by maximizing the path length of weakly absorbed photons, which results in an increase of minority carrier's photogeneration.

Using a base layer of a thickness smaller than the minority carrier diffusion length, which improves the collection efficiency of the solar cell.

Increase photon recycling effects by optically confining photons generated by radiative recombination.

Many approaches are possible to implement light trapping in GaAs solar cells. One of the simplest implementations of this concept is planar back reflector, ensuring that weakly absorbed photons will cross the cell twice.

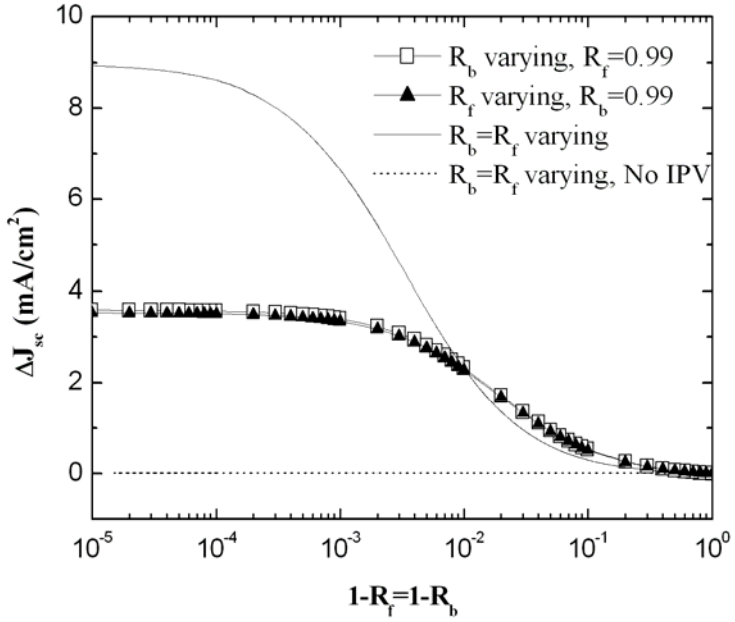

Figure 21 Effect of the internal reflections R_f and R_b on the short circuit current J_{sc}. The short circuit current IPV gain ΔJ_{sc} is referred to the situation where no IPV effect is present. Calculated for $N_D = N_t(B) = 10^{17}$ cm^{-3}.

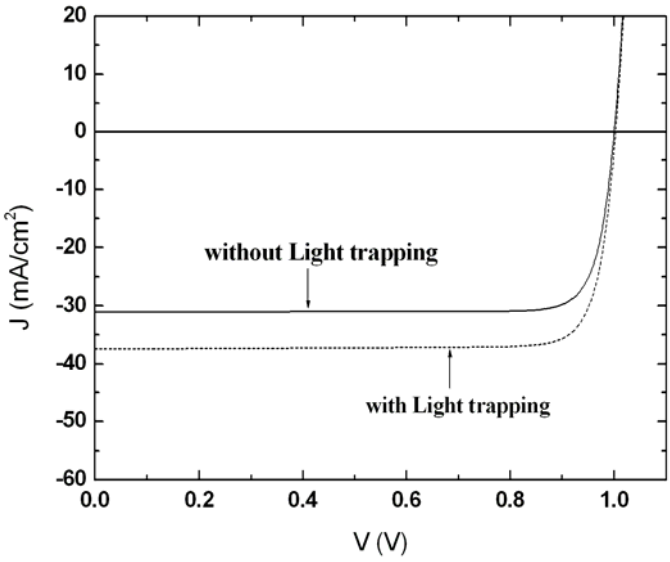

Figure 22 Current-voltage curve $J(V)$ of an IPV GaAs solar cell with $Cu(B)$ impurity density $N_t = 3\times10^{16}$ cm^{-3}, calculated with ($1\text{-}R_f = 1\text{-}R_b = 10^{-4}$) and without ($R_f = R_b = 0$) light trapping.

This approach is compatible with most solar cell fabrication technologies, and can be realized by epitaxial lateral overgrowth or by incorporating a Bragg mirror reflector between the solar cell and the substrate. The first approach gives a reflection of about 50 % at normal incidence, whereas the second gives a high reflection (> 95 %) [42]. Other researchers have proposed a Bragg reflector structure consisting e.g. of thin alternating layers of AlAs and $(Al_xGa_{1-x})As$. This structure is reported to "reflect nearly 100 % of long wavelength photons" [43]. The implementation of such a Bragg reflector in a conventional heteroface cell would enhance the efficiency by approximately 1 % absolute [43].

Another scheme to increase light trapping efficiency is by texturing the back mirror to scatter the reflected light. The usual approach is to model the textured back mirror as a Lambertian reflector [44]. Texturing front and back surfaces can provide a high degree of light trapping, leading to high internal reflection coefficients. A discussion of possible experimental realisations, and of the practical limits that can be achieved, however, is beyond the scope of this thesis.

3.4.3 GaAs solar cells with two impurity levels

The various energy levels introduced by copper impurities in the GaAs band gap are of different nature. Usually, the levels at 0.14 eV ('Cu(*A*) level') and 0.40 eV ('Cu(*B*) level') above the valence band edge are attributed to one Cu_{Ga} acceptor type defect (i.e. substitutional copper at a gallium site), which can be singly or doubly occupied [28], though other interpretations are reported as well [39]. The other dominant Cu level at 0.24 eV above the valence band edge can be attributed to a variety of Cu related defect complexes [28]; we call it here the Cu(*C*) level. It follows that the occupation and recombination of the Cu(*A*) and Cu(*B*) levels should be not be described by the classical Shockley-Read-Hall (SRH) formalism [32] [45], but by the Sah and Shockley theory for multiply charged defects [46]; this theory has been presented conveniently for two levels / three charge states e.g. in [47].

One could expect that the SRH formalism as used in SCAPS becomes inaccurate due to the presence of multiple charge defect as in the case of Cu(*A*) and Cu(*B*). For this reason we first checked if replacing multiple level statistics by the simple SRH single level statistics will not give large error on our calculations.

The equilibrium occupation probability with single level SHR statistics is given by:

$$f(E_F,E)=\frac{1}{1+\exp\left(\frac{E-E_F}{kT}\right)} \tag{39}$$

And with multilevel statistics by [47]:

$$f^0=\frac{1}{1+2exp\left(\frac{E_F-E}{kT}\right)+exp\left(\frac{2E_F-2E-U}{kT}\right)} \tag{40}$$

$$f^+=2exp\left(\frac{E_F-E}{kT}\right).f^0 \tag{41}$$

$$f^-=exp\left(\frac{2E_F-2E-U}{kT}\right).f^0 \tag{42}$$

where: f^0 is defined as the probability that a defect level is unoccupied, f^+ as that of singly occupied and f^- as that of doubly occupied.

E_F is the Fermi level energy.

E is the energy of the first level (transition (0/-1))

U is the is the correlation energy between the two levels.

3.4.3.1 Single-level statistics (SRH)

The occupation probalities of level Cu(A) and Cu(B) as described by SRH statistics are given by:

$$f_A(E_{Fp},E_{Fn}) = \frac{c_{nA}.n(E_{Fp},E_{Fn}) + e_{pA}}{c_{nA}.n(E_{Fp},E_{Fn}) + e_{nA} + c_{pA}.p(E_{Fp},E_{Fn}) + e_{pA}} \quad (43)$$

$$f_B(E_{Fp},E_{Fn}) = \frac{c_{nB}.n(E_{Fp},E_{Fn}) + e_{pB}}{c_{nB}.n(E_{Fp},E_{Fn}) + e_{nB} + c_{pB}.p(E_{Fp},E_{Fn}) + e_{pB}} \quad (44)$$

Where: first formula (43) intermadiate second formula (44)

E_{Fp}, E_{Fn} the Fermi energy levels for holes and electrons respectively.

$C_{n,(p)\,A}$ ($C_{n,(p)B}$) the capture coefficient for electrons (or holes) of level Cu(A) (or Cu(B)).

$e_{n,(p)A}$ ($e_{n,(p)B}$) the emission coefficient for electrons (or holes) of level Cu(A) (or Cu(B)).

Assuming both Fermi levels measured from the valence band edge, the concentration of holes and electrons are:

$$p(E_{Fp},E_{Fn}) = N_v.\exp\left(-\frac{E_{Fp}}{kT}\right); n(E_{Fp},E_{Fn}) = N_c.\exp\left(-\frac{E_g - E_{Fn}}{kT}\right) \quad (45)$$

The total charge is:

$$Q_{\text{single}} = N_{t1}.f_A(E_{Fp},E_{Fn}) + N_{t2}.f_B(E_{Fp},E_{Fn}) \quad (46)$$

The recombination rate for the two levels are:

$$U_A(E_{Fp},E_{Fn}) = \frac{N_{tA}.[n(E_{Fp},E_{Fn}).p(E_{Fp},E_{Fn}) - n_i^2]}{c_{nA}.n(E_{Fp},E_{Fn}) + e_{nA} + c_{pA}.p(E_{Fp},E_{Fn}) + e_{pA}} \quad (47)$$

$$U_B(E_{Fp},E_{Fn}) = \frac{N_{tB}.[n(E_{Fp},E_{Fn}).p(E_{Fp},E_{Fn}) - n_i^2]}{c_{nB}.n(E_{Fp},E_{Fn}) + e_{nB} + c_{pB}.p(E_{Fp},E_{Fn}) + e_{pB}} \quad (48)$$

The total recombination rate is then:

$$U_{\text{single}}(E_{Fp},E_{Fn}) = U_A(E_{Fp},E_{Fn}) + U_B(E_{Fp},E_{Fn}) \quad (49)$$

3.4.3.2 Multi-level statistics (Sah and Shockley):

We follow the description given by Schropp and Zeman [47] for levels with double occupation; this description is more transparent than the original treatment by Sah and Shockley [46] which is more general, and applies to any number of possible occupations. We adapt the notation to a double acceptor: it can be occupied with zero electrons (occupation probability $f^{(0)}$, charge state 0), with one electron (occupation probability $f^{(1)}$, charge state -1) or with two electrons (occupation probability $f^{(2)}$, charge state -2). The occupation probabilities are given as:

$$f^{(0)}(E_{Fp},E_{Fn}) = \frac{P_A.P_B}{N_A.P_B + P_A.P_B + N_A.N_B} \quad (50)$$

$$f^{(1)}(E_{Fp},E_{Fn}) = \frac{P_B.N_A}{N_A.P_B + P_A.P_B + N_A.N_B} \quad (51)$$

$$f^{(2)}(E_{Fp},E_{Fn}) = \frac{N_B.N_A}{N_A.P_B + P_A.P_B + N_A.N_B} \quad (52)$$

Where:

$$N_A(E_{Fp},E_{Fn}) = c_{nA}.n(E_{Fp},E_{Fn}) + e_{pA} \quad (53)$$

$$N_B(E_{Fp},E_{Fn}) = c_{nB}.n(E_{Fp},E_{Fn}) + e_{pB} \quad (54)$$

$$P_A(E_{Fp},E_{Fn}) = c_{pA}.p(E_{Fp},E_{Fn}) + e_{nA} \quad (55)$$

$$P_B(E_{Fp},E_{Fn}) = c_{pB}.p(E_{Fp},E_{Fn}) + e_{nB} \quad (56)$$

And the total charge is:

$$Q_{multi} = -N_t.[f^{(1)}(E_{Fp},E_{Fn}) + 2.f^{(2)}(E_{Fp},E_{Fn})] \quad (57)$$

And the recombination rate is given by:

$$U_{multi}(E_{Fp},E_{Fn}) = N_t[n(E_{Fp},E_{Fn}).p(E_{Fp},E_{Fn}) - n_i^2]\times \frac{c_{nA}.c_{pA}.P_B(E_{Fp},E_{Fn}) + c_{nB}.c_{pB}.N_A(E_{Fp},E_{Fn})}{N_A.P_B + P_A.P_B + N_A.N_B} \quad (58)$$

Using parameters cited in Table 1.3 and Eqs. (46) to (58), the recombination rate and the total charge are plotted for the two statistics: SRH and Sah & Shockley. The plots are presented in Figure 23 a and b respectively. As can be deduced from this curve, the error on replacing the multiple-level statistic by the single-level statistic is not large at all.

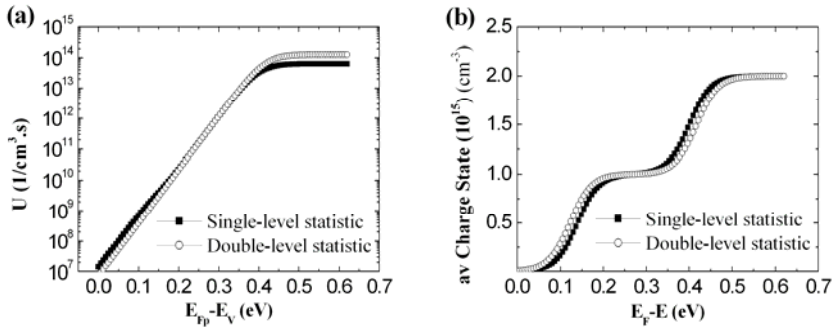

Figure 23 (a) Recombination rate in single-level statistic and double-level statistic calculated for $N_t = 10^{15}$ cm^{-3} and V = 0.8 Volts. (b) the average charge of state.

We pointed out that the occupation and recombination in such states can accurately be described by the more simple SRH formalism, provided that one attributes the same density N_t to both levels, and that one shifts the 0/-1 level (here the Cu(A) level) over an energy $kT\ln(2) \cong 17$ meV towards the valence band, and the-1/-2 level (here the Cu(B) level) with $kT\ln(2)$ towards midgap. In view of the large uncertainties about the energy levels in the literature, this small shift can be neglected.

To our knowledge, SCAPS is the only solar cell simulator available that treats the IPV effect. It has however also limitations: one can input three recombination mechanisms only. Since one is needed to adjust the recombination and the open circuit voltage to a realistic value, only two IPV levels are available, and hence we cannot examine the influence of all three copper levels Cu(A), Cu(B) and Cu(C) simultaneously. Thus we will first examine the influence of two IPV levels, and compare the result with the

effect of one IPV level. This is done in Figure 24. For only one level present, one can see that the IPV effect is more pronounced as the level is deeper, thus the largest IPV effect is with the Cu(*B*) level. This confirms results in [20]. When two levels are present, the IPV effect is somewhat lower than the IPV effect with only the deepest of the two levels present, e.g. the curves for the B + A or the B + C levels are somewhat below the curve for the 'only B level'.

It is important to note that in the case of two impurity levels as treated here, only direct transition between a trap and the conduction and valence bands are considered. The reason is that the occurrence of transitions of electrons between levels requires the distance d between neighbouring traps to be small enough to allow for tunnelling (d < 5 - 10nm) corresponding to high concentration doping. This is not the case in our calculation where we considered low concentrations due to the limited solubility of Cu in GaAs.

When we adopt the interpretation that the Cu(*A*) and Cu(*B*) levels originate from one single substitutional Cu impurity with two charge states, only *A* + *B* combination in Figure 24 is physically possible. We thus further explore this case.

However, if we assume that concentration of copper impurity in each level is equal to that in only one level, e.g. in Figure 24 comparing B level alone for $N_t = 3\times10^{16}$ cm^{-3} with *A* + *B* levels for $N_t = 6\times10^{16}$ cm^{-3} we find that the IPV effect gives an improvement in the short circuit current density in the presence of *A* + *B*, but at the same time a decrease in the open circuit voltage higher than in the presence of only level *B*. This is due to the increase of recombination in the solar cell, which increases more drastically when the concentration of the defects is around the base layer doping.

In Figure 25 we calculated occupation probability of the deep levels in the base region of the GaAs solar cell, for $N_t = 3\times10^{16}$ cm^{-3} and $N_D = 10^{17}$ cm^{-3}. From this figure we see that the lower energy level, which corresponds to Cu(*A*) is more completely occupied than the higher energy level Cu(*B*) since this latter is the deeper one (close to the energy Fermi level) as it is shown at the band diagram of Figure 26.

The generation rate calculated for two different concentrations $N_t = 10^{15}$ and 3×10^{16} cm^{-3} short circuit condition are represented in Figure 27. This curve gives more information about the limiting processes in the presence of the two copper levels *A* and *B*, as the filling of the defect can be realized optically with available photons or thermally near the valence band. The generation current when the two levels are present is governed by the Cu(*B*)

process, which is optical emission of electrons from the defect to the conduction band (IPV-n_Cu(B)) when $N_t \leq 10^{16}\text{cm}^{-3}$, and thermal emission of holes from the defect to the valence band (Th-p_Cu(B)) when $N_t > 10^{16}\text{cm}^{-3}$.

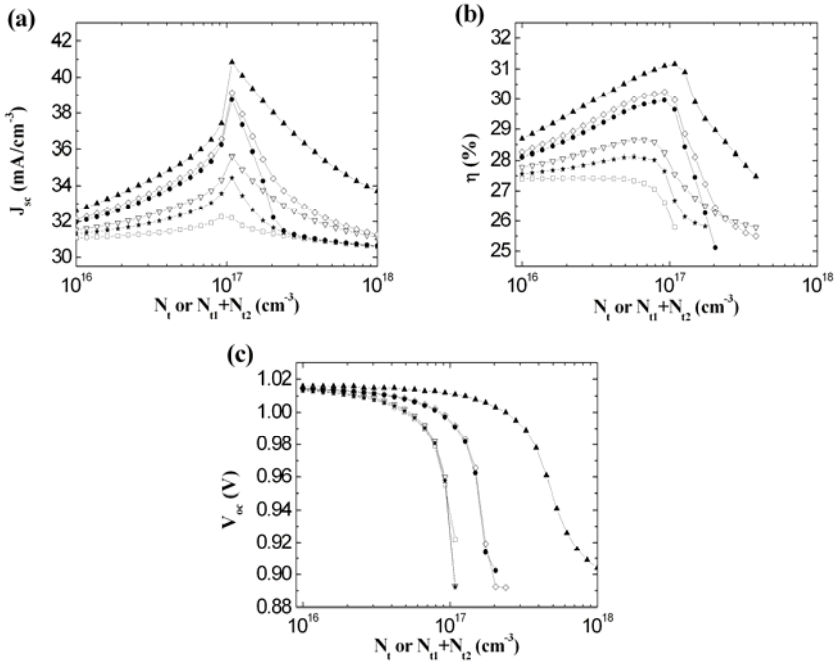

Figure 24 Solar cell parameters of an IPV GaAs cell with one or two IPV levels present. Calculated for a base doping density $N_D = 10^{17}$ cm^{-3} and for internal reflection $1\text{-}R_f = 1\text{-}R_b = 10^{-3}$. With one level (e.g. A) present, the abscissa means $N = N_t(A)$; with two levels present (e.g. A and B), the abscissa means $N_t = N_t(A) + N_t(B)$, with $N_t(A) = N_t(B)$: (□) A level, (▽) B level, (▲) C level, (★) A + C levels, (◇) B + C levels, (●) A + B levels. (a) short circuit current J_{sc} ; (b) conversion efficiency η; and (c) open circuit voltage V_{oc}.

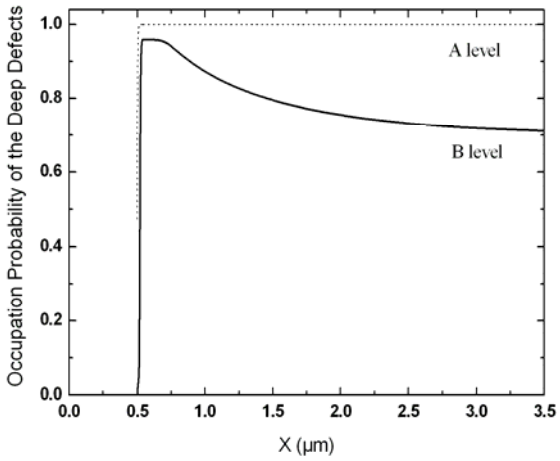

Figure 25 Occupation probability of the Cu impurity levels A and B in an IPV GaAs solar cell calculated for $N_t(A) = N_t(B) = 3\times10^{16}$ cm^{-3} and $1\text{-}R_f = 1\text{-}R_b = 10^{-4}$.

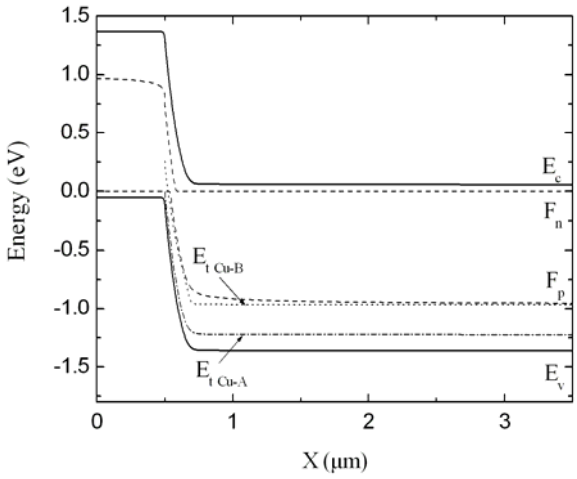

Figure 26 Energy band diagram of IPV GaAs solar cell calculated for $N_t(A) = N_t(B) = 3\times10^{16}$ cm^{-3} and $1\text{-}R_f = 1\text{-}R_b = 10^{-4}$ and under short-circuit condition.

For Cu(B) and impurity concentrations $N_t \leq 10^{16}$cm^{-3} the generation is governed by the photoemission process for both electrons and holes. For the

shallow level Cu(*A*), hole emission provided thermally (hole emission process (Th-$G_{p\text{-}CuA}$) is higher than the optical one (IPV-p_Cu(*A*)) since this level is close to the valence band. Concentrations $N_t \leq 10^{16}cm^{-3}$ keep the defect energy levels Cu(*A*) and Cu(*B*) lower to the energy Fermi level, which means that both of the defect levels are nearly fully occupied. In this case, optical electron emission processes (IPV-n_Cu(*B*) and IPV-n_Cu(*A*)) are higher than optical hole emission ones (IPV-p_Cu(*B*) and IPV-p_Cu(*A*)) and also higher then the thermal emission processes for electrons and holes (Th-n_Cu(*B*) and Th-n_Cu(*A*), Th-p_Cu(*B*), Th-p_Cu(*A*)). When copper impurity is increased, the defect levels start to pin the Fermi level in order to increase hole concentration and compensate the background doping of the base which is n-type. Two different situations can be deduced from Figure 27:

- For the shallow level Cu(*A*) increasing the defect concentration makes the hole emission strong and provided thermally.
- For the deep level Cu(*B*) increasing defect concentration leads to an increase of hole photoemission process (increase of IPV-p_Cu(*B*)) which decreases the photon flux available for the electron photoemission process (IPV-p_Cu(*B*)).

If the first one doesn't contribute to the optical generation rate due to IPV effect, the second one will compete with both, electron photoemission from the defect and with electron-hole pair creation by intrinsic band-to-band absorption, and both cases lead to a decrease in solar cell performances when increasing impurity copper concentration of Cu(*A*) and Cu(*B*).

Figure 28 shows the spectral response of the solar cell, in the four following cases: a solar cell without IPV, with Cu(*A*), with Cu(*B*) and with the two defect levels. It is confirmed that the contribution of the IPV effect to the short circuit current comes from sub-band gap absorption in the solar cell, which results in an extension of the infrared response, especially between $\lambda =$ 873 nm and $\lambda = 1250$ nm. The presence of Cu(*A*) alone gives an improvement of the spectral response at 873 nm $\leq \lambda \leq$ 1000 nm while Cu(*B*) improves the spectral response at wavelengths 873 nm $\leq \lambda \leq$ 1250 nm. The curve with light trapping but with no IPV effect present almost exactly coincides with the curve for no light trapping (not shown in Figure 28).

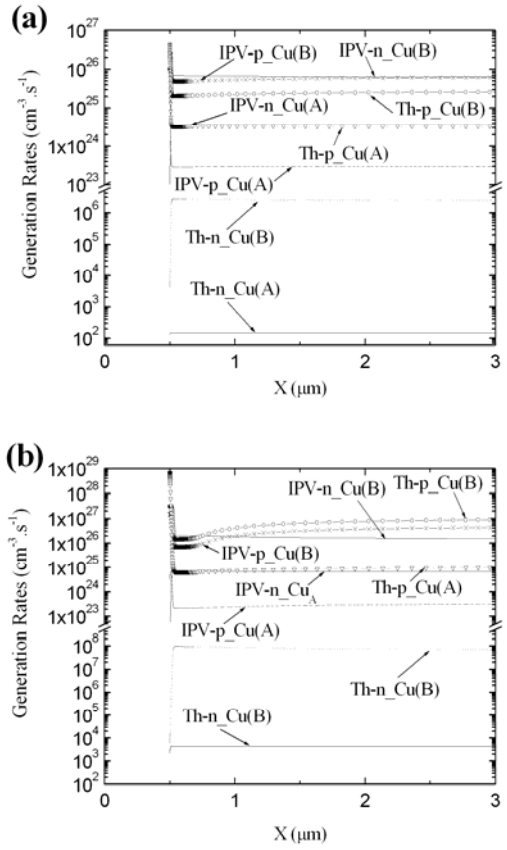

Figure 27 Optical generation rates calculated for $N_D = 10^{17}\,cm^{-3}$, $1\text{-}R_f = 1\text{-}R_b = 10^{-4}$.(a) at $N_t = 10^{15}\,cm^{-3}$; (b) at $N_t = 3\times10^{16}\,cm^{-3}$. (IPV-n_Cu(B)), (IPV-n_Cu(*A*)) are optical emission of electrons from defect Cu(*B*) and Cu(*A*) to the conduction band respectively. (IPV-p_Cu(*B*)), (IPV-p_Cu(*A*)) optical emission of holes from the defect Cu(*B*) and Cu(*A*) to the valence band respectively. (Th _Cu(*B*)), (Th-n_Cu(*A*)) thermal emission of electrons from the defect Cu(*B*) and Cu(*A*) to the conduction band respectively. (Th-n_Cu(*A*)), (Th-p_Cu(*B*)) thermal emission of electrons from the defect Cu(*A*) and Cu(*B*) to the conduction band respectively. (Th-p_Cu(*B*)), (Th-p_Cu(*B*)) thermal emission of holes from the defect Cu(*B*) ans Cu(*A*) to the valence band respectively.

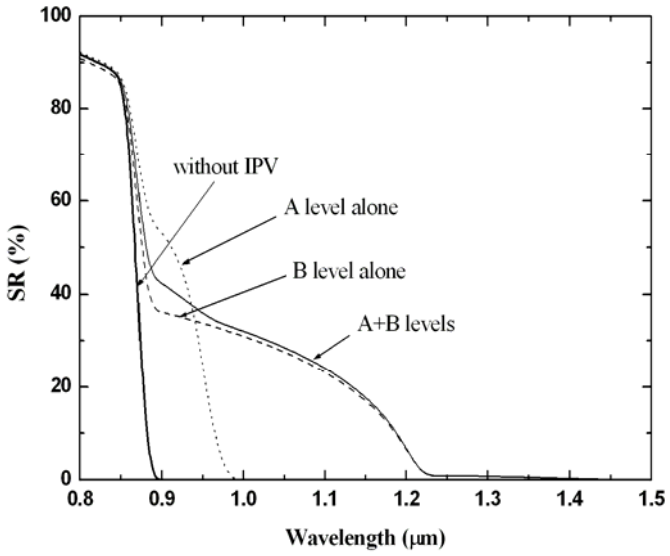

Figure 28 Spectral response curve of the IPV GaAs solar cell with and without Cu impurity levels A and B. The calculation is for $N_D = 10^{17}\text{cm}^{-3}$, $N_t(A) = N_t(\text{B}) = 3\times10^{16}\ \text{cm}^{-3}$ and $R_f = R_b = 0.9999$.

3.4.4 Effect of carriers thermal capture cross section and impurity energy level on short circuit current and efficiency

Figure 29 and Figure 30 show the IPV GaAs efficiency as function of hole and electron capture cross section respectively. The impurity energy level was varied as well in the two cases. A maximum of gain in efficiency and short circuit current is reached for an impurity energy level around 0.4 ~ 0.5 eV which represent almost E_g(GaAs)/3,and for hole capture cross sections ranging between σ_p: $10^{-22} \sim 10^{-16}$ cm^2, and σ_n: $10^{-22} \sim 10^{-20}$ cm^2, and are in agreement with the results in section 3.4.3.

A shallow impurity allows the thermal excitation process to be strong. However, deep defect level leads to a degradation of cell efficiency distinctly if its energy level is near to the mid-gap, because of electron-hole recombination through the defect. Thus, desirable impurities have small capture cross sections and large optical cross sections.

These two curves give a good approximation if one wants to investigate IPV effect in GaAs solar cells with other possible impurities which could be

more efficient as impurity photovoltaic effect, by looking at the appropriate values of the impurity energy level and thermal cross section of electrons and holes.

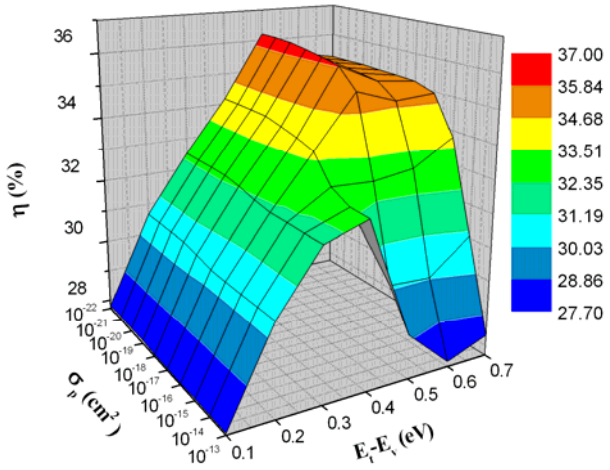

Figure 29 Efficiency of an IPV GaAs solar cell as function of Cu impurity energy level and hole capture cross section: $N_t = 9\times10^{16}$ cm^{-3}, and 1-R_f= 1-R_b=10^{-5}).

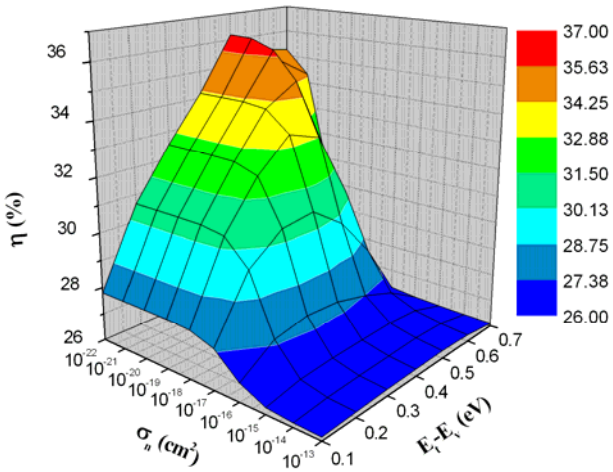

Figure 30 Efficiency of an IPV GaAs solar cell as function of *Cu* impurity energy level and electron capture cross section: $N_t = 9\times10^{16}$ cm^{-3}, and 1-R_f =1-R_b = 10^{-5}).

Chapter 4

GaAs solar cells: Selected simulation problems

4.1 Introduction

GaAs has a direct band-gap, high absorption coefficient, high carrier mobility, low sensitivity to space radiations, more favorable temperature behavior and a developed technology which make it the most efficient solar cell based material ever reported, with an extremely high efficiency of 26.1 % for a single junction solar cells at standard conditions [48].

The early high-efficiency GaAs cells have been made using liquid phase epitaxy technique. James and Moon (1975) reported a conversion efficiency of 19 % at very high concentration (C = 1735) [49]. At the beginning, a problem was conflicting the development of GaAs solar cells, is high surface recombination velocity, which causes deterioration of internal quantum efficiency at short wavelengths. To solve this problem two major approaches have been used. The most successful is the use of a $Ga_{1-x}Al_xAs$ window layer on the GaAs surface [50]. This layer was used to passivate the front surface of the cells and reduce the surface recombination velocity because of the good lattice matching of the AlGaAs/GaAs system. Thus the efficiency of GaAs cells exceeded 20 % in the late 1970s, when Woodall and Hovel produced heterostructure cells with one sun efficiency of 23 % [51]. The second approach consists of using an n^+p homojunction design, where Fan et al (1978) also produced cells of 20 % efficiency [52]. The high efficiency

was obtained in these unpassivated cells by using anodic oxidation to thin the emitter to less than 50 nm. The *n*-type emitter is so thin thus most of the photons penetrate deeper into the depletion and *p*-type region where the photogenerated carriers are not affected by the high recombination velocity. From the above discussions it follows that GaAs solar cells have a rather complicated structure. Thus, numerical simulation became necessary for a quantitative understanding of their operation. In this chapter, two problems are selected and analyzed; the effect of low concentration and temperature, and the effect of perimeter recombination on GaAs solar cells performance.

The investigated cells have different structures (*pn* or *pin*). The first part of this chapter will be devoted to simulation and discussion on GaAs solar cell performance under one sun illumination and low concentration. In the second part of this chapter, the effect of perimeter recombination on GaAs-based micro-solar cell will be treated and discussed. The results of the two problems have been reported in the *European Journal of applied Physics* [53] and in *Solar Energy materials and solar Cells* [9] respectively.

4.2 GaAs Solar cells under low concentration

It is well known that optical concentration offers an attractive and flexible approach to reducing high solar panels costs by substituting a part of the cells by a less expensive optical material. For instance, one cell operated under 1000 sun concentration can produce the same power output as 1300 cells under one sun [7].

The best GaAs concentrator cells have reached a very high level of development, comparable to that of the best Si cells and that is due to a set of advantages, including a high absorption coefficient, a good radiation resistance and especially high temperature operation, which is unavoidable at high concentration ratios. In general the GaAs solar cell performance exceeds that of Si cells. The efficiency of concentrator cells for both materials has reached 26-28 % [43].

In this section we report results obtained using both a computer simulator and a theoretical model of AlGaAs/GaAs heterojunction solar cell operating under low injection conditions. The effect of temperature, concentration ratio and series resistance were examined.

The simulation results were carried out by the software SCAPS. Note that the program was adopted the first time in 2004 for the simulation of GaAs heteroface solar cells [8] and the obtained results were in good agreement with experimental measurements.

4.2.1 Theoretical model

The effect of temperature (T) and concentration ratio (C) on photovoltaic parameters of concentrator solar cells is modelled using the expressions given in [54]:

$$J_{sc}(T,C) = C.J_{sc}(T_0,C_0) \tag{59}$$

$$V_{oc}(T,C) = V_{oc}(T_0,C_0)+\left(\frac{E_g}{e}-V_{oc}(T_o,C_0)\right)\times\left(1-\frac{T}{T_0}\right) +\left(\frac{nkT}{e}\right)\left[\ln C-\gamma\ln\left(\frac{T}{T_0}\right)\right] \tag{60}$$

$$FF = \frac{P_m}{J_{sc}.V_{oc}.A} = \frac{J_m.V_m}{J_{sc}.V_{oc}} \tag{61}$$

$$\eta = \frac{FF.J_{sc}.V_{oc}.A}{P_{inc}} \tag{62}$$

where: $J_{sc}(T_0,C_0)$ and $V_{oc}(T_0,C_0)$ are the short circuit current density and open circuit voltage respectively at temperature T_0 = 300 K and the reference concentration ratio C_0 = 1 corresponds to an illumination intensity of 1 sun. In our case, these two parameters were calculated using the software SCAPS using T_0 = 300 K and C_0 = 1 (AM 1.5D).

$J_{sc}(T,C)$ and $V_{oc}(T,C)$ are the short circuit current density and open circuit voltage respectively at temperature T and concentration ratio C.

E_g is the energy band gap of the material,

n is the ideality factor of the diode which is ranging from 1 to 3,

γ is a factor varying from 2 to 4 describing the weak temperature dependence of N_C, N_V, $\mu_{n,p}$, $L_{n,p}$.

FF is the fill factor of the cell,

A the solar cell area,

η the efficiency of the cell,

P_{inc} is the incident power,

and P_m is the maximum power point on the J-V curve, defined by the points J_m and V_m.

The *J-V* characteristic of the cell is described by the standard single-exponential model:

$$J = J_s\left[\exp\left(\frac{V - JR_sA}{nkT}\right) - 1\right] - J_{sc} \tag{63}$$

J_s is the saturation current density of the diode and R_s is the series resistance. Moderate values of R_sA, of the order of 1 $\Omega.cm^2$ can reduce the fill factor *FF*, and higher values even can reduce the the short circuit-current J_{sc}. Therefore the effect of series resistance in solar cells can lead to a remarkable degradation in fill factor and efficiency. The shunt resistance is neglected.

In concentration solar cells, the cell reached its steady temperature when the illumination power absorbed is equivalent to the electric power delivered to the load plus the dissipated power in the form of heat to the atmosphere. Dissipation is achieved through radiation, convection and conduction. In this case, the following equation must be satisfied to achieve equilibrium [54]:

$$P_{inc}.C.A\left(\alpha_i - \eta(T)\right) = h_c.A\left(T - T_0\right) + A.\varepsilon.\sigma.\left(T^4 - T_0^4\right) \tag{64}$$

where: P_{inc} is irradiance in W/m^2, C is the concentration, A is the cell area, $\eta(T)$ is the efficiency of conversion at the operating temperature, α_i is the integrated absorption of the wavelengths of the light involved, h_c is the coefficient of heat transfert (in $W.m^{-2}.K^{-1}$), ε is the surface emmisivity, σ is the Stefan-Boltzmann constant (5.67×10^{-8} $W.m^{-2}.K^{-4}$), T is the operating temperature of the cell and T_0 is the ambiant temperature (T_0 = 300 K).

To calculate the temperatures corresponding to each value of the concentration ratio, we solved numerically Eq. (64) in ambient atmosphere with different solar heat flux. In our calculation we neglected the term $\eta(T)$ in Eq. (64) which is showed a linear decrease with temperature and no dependency on concentration [55]. Combination between cooling by convection and radiation has been investigated in our study. We treated different method of cooling by convection: convection air and convection by water using different modes (Laminar and turbulent mode).

4.2.2 Details of the solar cell structure

Figure 31 shows the structure of the cell used in the simulation. The cell input parameters are those of a solar cell grown by metalorganic chemical vapor deposition technique (MOCVD). The device included a 30 nm

$(Al_{0.9}Ga_{0.1})As$ front window layer which is nearly transparent to photons with energy lower than 3 eV, thus with $\lambda > 413$ nm. It prevents minority carriers in the emitter from diffusing to the front surface of the cell, where they could recombine at high rate. The highly doped buffer layer is used as a minority carrier mirror at the rear of the cell. Additional details of the structure can be found in Ref [56].

Numerical simulations of the structure were carried out using SCAPS1D. The materials parameters used are the same as those cited in Ref [56]. For the absorption coefficient data, we used those given in [40]. The SCAPS calculations were carried out for moderately concentrated light, with C ranging from 1 to 10 sun.

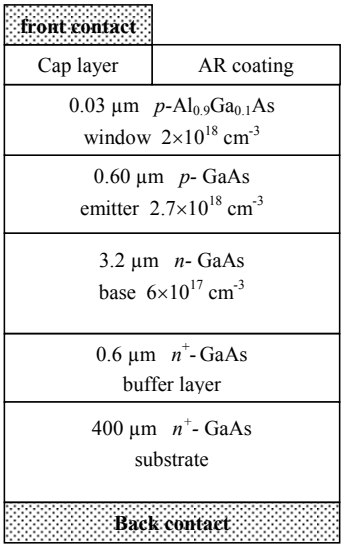

Figure 31 AlGaAs/GaAs solar cell Structure. The thickness and the shallow doping density and type of each layer in the structure are indicated.

For the calculation, knowledge of the temperature dependence of the GaAs material parameters is needed.

The band gap energy and its temperature dependence are given by [50]:

$$E_g(T) = E_g(0) - \alpha T^2 / (T + \theta) \tag{65}$$

where $E_g(0) = 1.519$ eV is the energy gap at 0 K, and $\alpha = 5.405 \times 10^{-4}$ eV.K^{-1} and $\theta = 204$ K are empirical parameters.

The measured electron and hole mobilities of GaAs materials grown with different technologies are given by an analytical formula [50] as a function of the impurity concentration $N = N_A + N_D$ and the temperature T:

$$\mu_n = 7200\left\{\left(\frac{T}{300}\right)^{2.3} + \frac{N}{10^{17}}\ln\left[1+\left(\frac{6\times10^{16}}{N}\right)^{2.3}\left(\frac{300}{T}\right)^{1.5}\right]\right\}^{-1} \quad (66)$$

$$\mu_p = 370\left\{\left(\frac{T}{300}\right)^{2.3} + \frac{N}{10^{17}}\ln\left[1+\left(\frac{4\times10^{16}}{N}\right)^{2.3}\left(\frac{300}{T}\right)^{1.5}\right]\right\}^{-1} \quad (67)$$

In these formulas, μ_n and μ_p are in cm^2/Vs, T is in K and N is in $1/cm^3$. The formulae for the diffusion length as a function of temperature are given by [50]:

$$L_{n,p} = L_{n,p}\left(300\ \mathrm{K}\right)\left(\frac{T}{300\ \mathrm{K}}\right)^{3/2} \quad (68)$$

The parameters that are temperature dependent, such as the band gap of the material, the mobility and the diffusion length of electrons and holes were calculated separately using Eqs. (65) - (68), then introduced in SCAPS.

4.2.3 Optical concentration and temperature effects

4.2.3.1 Air convection cooling

GaAs cells operating at high concentration absorb a large amount of heat, from infrared radiation, thermalization of recombined carriers and flow of high currents in resistive emitters and gridlines. Hence, the junction temperature can easily exceed 50 °C under realistic operating conditions [7].

The temperatures of the cell as function of the concentration ratio of the sun calculated using Eq. (64) are presented in Figure 32. In this case, we supposed that the cell is cooled by air, with h_c = 10 $W.m^{-2}.K^{-1}$ for air at 1 m/s [54]. As it can be seen, cooling by air convection is not enough, since a concentration ratio of 5 sun gives a rise in the temperature of around 100 °C.

In order to evaluate the effect of concentration and temperature in this case of cooling on the solar cell performances, short circuit current density (J_{sc}), open circuit voltage (V_{oc}), fill factor (FF) and conversion efficiency (η) are

calculated as function of concentration ratios, with air cooling system and also if a perfect cooling system is used (T = 300 K).

The solar cell outputs J_{sc}, V_{oc}, and η are shown in Figure 33 a, b and c respectively. The different temperatures calculated for the corresponding variations of concentration ratios are shown on the curves, which represent the temperatures of air convection cooling. The temperature of the sink is taken as 300 K.

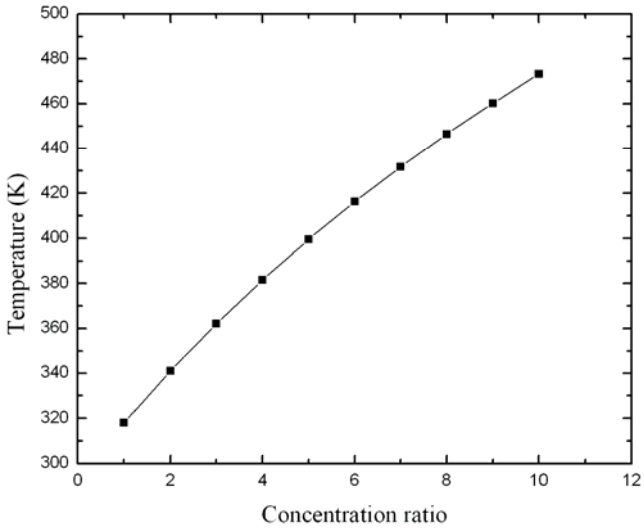

Figure 32 Temperature of the GaAs cell as function of concentration ratio calculated using Eq. (64) in the case of air cooling.

We found a good agreement between parameters calculated using equations (59) - (62) and those simulated with SCAPS.

The short circuit current increases with increasing concentration ratio C as is predicted from (59). Short-circuit current (J_{sc}) increase slightly with increasing temperature. This can be attributed to increased sun light absorption, since semiconductor band gap decreases with temperature, therefore more photons with lower energy are absorbed.

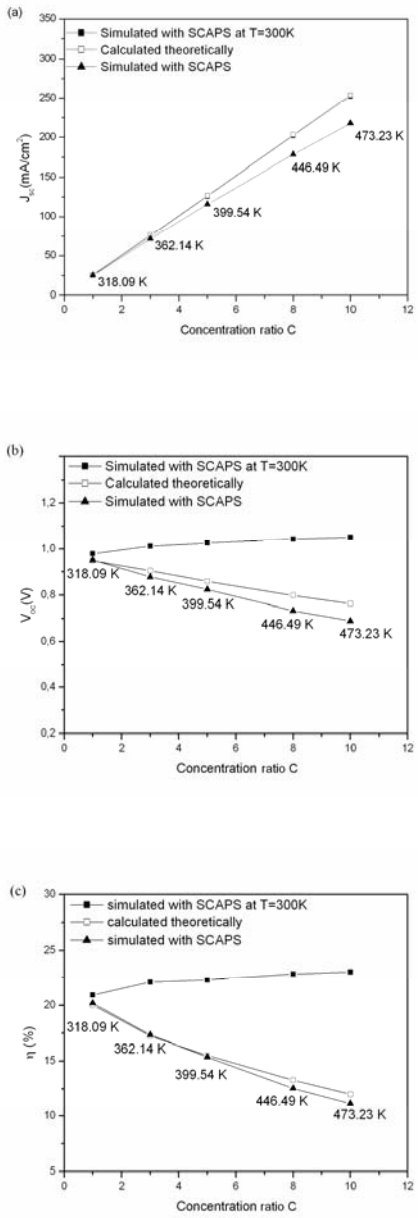

Figure 33 Simulated and calculated solar cell parameters. (a) short-circuit current J_{sc}; (b) open circuit voltage V_{oc} and (c) efficiency η versus concentration ratio at different temperatures calculated using Eq. (64) in the case of cooling by air convection (h_c = 10 W.m^{-2}.K^{-1}). Also curves calculated in the case of a perfect cooling (T = 300K) are shown for comparison.

However, the band gap narrowing with temperature leads to a reduction in (V_{oc}). The increase in (J_{sc}) is not enough to compensate the loss in (V_{oc}), so the efficiency also decreases with temperature, for this particular cooling.

In this case we conclude that it is not favourable to operate GaAs solar cell under concentrated sun light, when they are only cooled by air convection with air at 1m/s (h_c = 10 W.m^{-2}.K^{-1}). Indeed, the efficiency decreases with concentration right from $C > 1$ on. Thus, in order to extract the maximum advantage from the use of optical concentrators, we must keep the temperature of the cell as close as possible to ambient temperature, by applying more efficient cooling.

4.2.3.2 Water convection cooling

We solved Eq.(64) by taking into account the operation of the solar cell under radiation and water convection cooling simultaneously. For water convection, two different modes have been investigated in this thesis, Laminar mode with h_c = 380 W.m^{-2}.K^{-1} [54] and Turbulent mode with h_c = 3683 W.m^{-2}.K^{-1} [54].

The temperatures of the cell corresponding at each concentration ratio are presented in Figure 34 as well as the thermal resistance. Temperatures of the cell in the case of air convection are also shown for comparison. It is clear from this figure that water cooling is better solution of removing heat from the solar cell. The thermal resistance in water cooling (with $R_s.A$ = 2.6 Km^2/kW in Laminar mode and $R_s.A$ = 0.26 Km^2/kW in Turbulent mode), is much lower than in cooling by air (with $R_s.A$ = 22 Km^2/kW).

The solar cell efficiency calculated for each cooling system is presented in Figure 36. The performances are significantly better with water cooling than air cooling and allow for heat recovery if a suitable system is used.

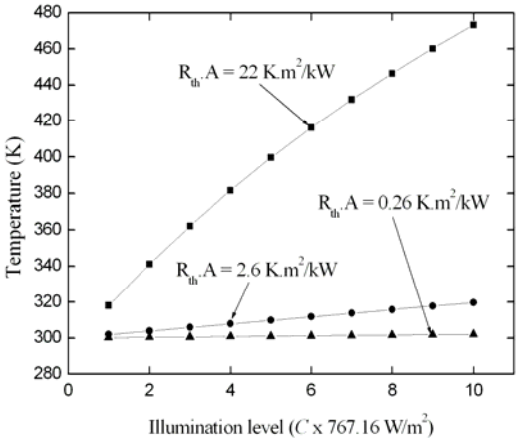

Figure 34 Solar cell temperatures as function of illumination under different cooling system, calculated using Eq. (64). (■) Air convection (at 1m/s; $h_c = 10\ W.m^{-2}.K^{-1}$); (●) Water convection in Laminar mode ($h_c = 380\ W.m^{-2}.K^{-1}$ [54]) and (▲) Water convection in Turbulente mode ($h_c = 3683\ W.m^{-2}.K^{-1}$ [54]). Thermal series resistance deduced from each cooling system is also shown.

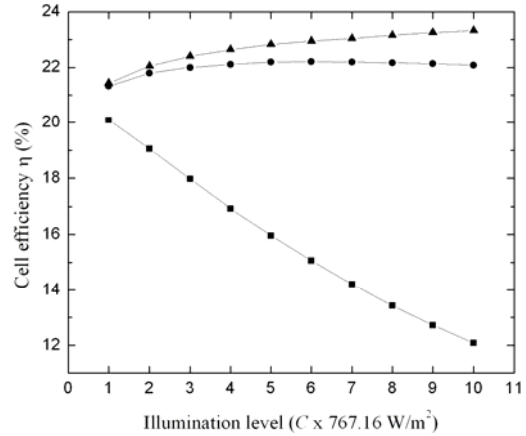

Figure 35 Solar cell efficiency as function of illumination under different cooling system, calculated using Eq. (64). (■) Air convection (at 1m/s; $h_c = 10 W.m^{-2}.K^{-1}$); (●) Water convection in Laminar mode ($h_c = 380\ W.m^{-2}.K^{-1}$ [54]) and (▲) Water convection in Turbulente mode ($h_c = 3683\ W.m^{-2}.K^{-1}$ [54]).

In concentration solar cell technology this can be achieved by cooling. There are two types of cooling: passive cooling and active cooling [54][55], and the optimum cooling solution differs between the various types of concentration geometry: single solar cells geometry, linear geometry or densely packed modules geometry.

- In single solar cells geometry, sunlight is usually focused onto each cell individually. So each cell has an area equal that of the concentration available for heat sinking. These cells typically only need passive cooling even for very high concentrations, such as cooling by convection. The cooling device is made up of linear fins on all available heat sink surfaces. It was recognized that passive cooling is more efficient for cells if their size is reduced (~ 5mm diameter) [57][58]. Heat sinks for such small cells would be similar to those used for power semiconductor devices.
- In linear geometry, where parabolic troughs or linear Fresnel lenses are used to focus the light onto a row of cells, both passive and active cooling can be used. For passive solution, cells are cooled using heat sinks or by a heat pipe approach. Also some new solutions were suggested for passive cooling by forced convection, such as microchannel heat sinks, which are very promising because they have the option of being incorporated in the cell manufacturing process [55]. For active cooling, the row of cells is cooled by fluid (liquid or gaseous) flow through channels or an internally finned aluminum pipe. The fluid should be capable of absorbing and releasing heat by transporting it through its movement [55].
- In the case of densely packed modules geometry, each of the cells has only its rear side available for heat sinking, which implies that passive cooling cannot be used in this configuration. The active cooling concept is based on water cooling circuit, in which water flow through small parallel channels in thermal contact with the cells.
- In other technologies, the cells are submerged in a circulating coolant liquid, by this way heat is transferred from two cell surfaces instead of one. Also the coolant acts as a filter by absorbing the incoming low-energy radiation before it reaches the cells. The coolant liquid must be dielectric to provide electrical insulation of the cells [55].

This was a short summary of cooling solutions for concentration solar cells. Nonetheless, experimental work is needed to know the best method of

cooling for each system and to determine the costs of these performance cooling options which are not yet confirmed in the literature.

4.2.4 Series resistance effect

There are several physical mechanisms responsible for the series resistance, the major contributors are the bulk resistance of the semiconductor, the sheet resistance of the metallic contacts and interconnections, the contact resistance between the metallic contacts and the semiconductor, and the resistance of the two-dimensional geometry of the contact.

In concentrator solar cell it is important to minimize series resistance, as the flow of high currents in emitters and gridlines causes a resistive voltage loss.

In the structure shown in Figure 31, the emitter and the base were relatively highly doped to minimize bulk resistance [56]. Values of contacts resistance (between the gridlines and the cap layer) less than $10^{-5}\,\Omega.cm^2$ are usually acceptable and can be realized using a thin alloyed layer of Au/Zn/Au (for a *p*-type emitter) or Au/Ge/Ni/Au (for *n*-type emitter) [43]. The series resistance reported in Ref [56] is quite low (~ 5mΩ).

In SCAPS, one can introduce different series resistance values, to study its effect on the solar cell output. In this work we calculated the fill factor and the efficiency of the concentrator solar cell versus concentration ratio, for different series resistance.

From Figure 36 a and b of the (*FF*) and (η) respectively we can easily observe that the (R_s) has a significant effect. A series resistance of only 1 $\Omega.cm^2$ can lead to a crucial degradation in the fill factor and the efficiency particularly for high concentration ratio *C*, when (*FF*) decreases at a rate of about 0.5 % per decade, while (η) decreases at rate of 2 % per decade.

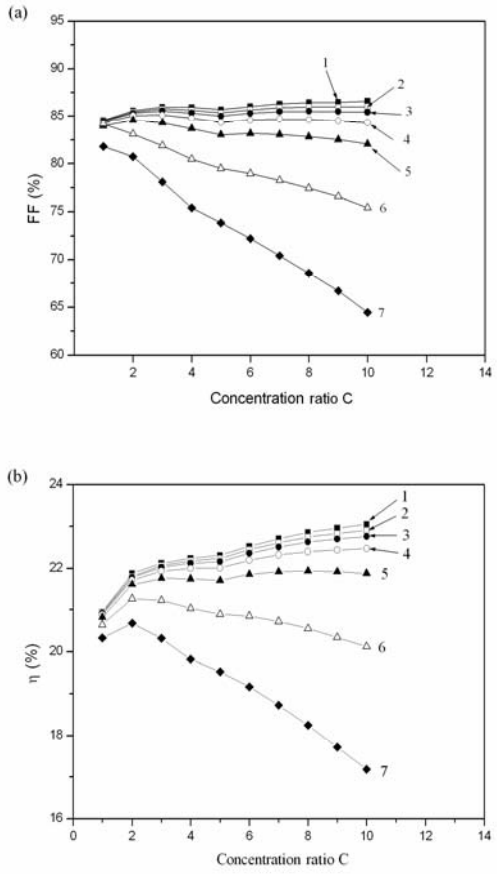

Figure 36 Effect of series resistance on: (a) solar cell fill factor and (b) solar cell efficiency at T = 300K. (1) $R_s.A = 0\ \Omega.cm^2$; (2) $R_s.A = 2.5\times10^{-2}\ \Omega.cm^2$; (3) $R_s.A = 5\times10^{2}\ \Omega.cm^2$; (4) $R_s.A = 10^{-1}\ \Omega.cm^2$; (5) $R_s.A = 2\times10^{-1}\ \Omega.cm^2$; (6) $R_s.A = 5\times10^{-1}\ \Omega.cm^2$; (7) $R_s.A = 1\ \Omega.cm^2$.

4.3 Perimeter recombination effect in GaAs-based mico-solar cell

The most important parameter for micro solar cells is the open circuit voltage since most MEMS use either electrostatic or piezoelectric actuators which means that a high voltage is preferred to a high current, and that usually several tens of micro solar cells have to be connected in series to obtain useful working voltage. In solar cells with very small area, an effect that is normally totally negligible can become dominant: the perimeter recombination, this is explained below.

Gallium arsenide surfaces contain a high density of defects. These defects affect the electrical characteristics of the solar cell because they cause surface recombination and because they carry charge and hence influence the band bending and the solar cell behaviour. With reference to Figure 37 we call the recombination at the upper GaAs surface "surface recombination", and the recombination at the sidewalls of the mesa structure "perimeter recombination". While the surface recombination reduces the photocurrent of the solar cell, the recombination along the cell's perimeter increases its dark current. The perimeter recombination considerably increases the dark current, particularly for small area cells, where the perimeter to area is important. In solar cells, an efficiency loss of 3 – 4 % (relative) has been reported [59]. When the cells are in mesa form, recombination at exposed side-walls is very important, some technical measures could be taken to reduce this effect. These techniques also reduce the surface recombination, and are generally called surface passivation. A technological description is out of the scope of this thesis. A result of our analysis of perimeter recombination will be that, in order to produce 100 V using 100 μm × 100 μm micro solar cells, 96 unit cell will be sufficient if there were no perimeter recombination current, whereas due to the perimeter effect 102 unit cells are necessary.

To calculate accurately the effect of perimeter recombination it is important to understand the mechanism of recombination at GaAs surface. The first model of the perimeter recombination current was proposed by Henry el al. [60]. They developed an analytical expression for the perimeter current at the junction surface, based on a number of assumptions including Fermi level pinning, density of donor and acceptor defects with energies uniformly distributed across the energy gap and a constant ratio of electron and hole density at the surface. Their results showed that the $n = 2$ recombination current did not correlate with the area and was not primarily due to recombination at the perimeter. Tobin et al. [34] found by measuring a series of mesa-isolated diodes with different areas, that the $n = 2$ dark current measured in small GaAs solar cells arose from recombination within the space-charge region exposed at the perimeter of the mesa. In this section we present simulation of the perimeter recombination current in a mesa form solar cell. The perimeter recombination current is known to have an ideality factor of 2 ($2kT$ behaviour) for low and moderate voltages, but at higher voltages an ideality factor of 1 (kT behaviour) is dominant. Most of the available solar cell simulators are one-dimensional models which proved to be accurate for large-area solar cells. As far as small-area solar cells are

concerned one-dimensional description leads to inaccurate results. One of the shortcomings of one-dimensional modelling is the perimeter recombination current and its contribution to the cell dark current. For this purpose we modify the results obtained by the one dimensional software SCAPS. The perimeter recombination current is introduced into the bulk dark current calculated by this software. After this correction the solar cells are analysed and the photovoltaic parameters are calculated. The perimeter recombination current is evaluated using an analytical expression obtained by modifying the model of Dodd et al. [61].

4.3.1 The model

In the case of a mesa GaAs solar cell, as shown in Figure 37, perimeter recombination current constitutes an important proportion of the dark current, when the lateral dimensions become comparable to the cell thickness. This is the case of "mico solar cells" which are studied for application in micro-electromechanical systems (MEMS). The density of surface states at the GaAs surface is known to be very high and distributed across the entire forbidden energy band gap with a total density ranging from 10^{12} to 10^{14} cm^{-3} [7][62]. Surface states generally introduce energy levels lying in the forbidden energy band gap between the valence and the conduction bands. They arise either from the effect of abrupt termination boundary of the crystal structure at the surface or from the adsorption of impurities on the surface.

In this analysis the perimeter recombination occuring at the surface of an heteroface GaAs solar cell is treated. In this case, the perimeter recombination current can be decomposed into two components: one resulting from carrier injection where the space charge region intersects the surface and the other due to injection from the bulk region outside the junction (quasi-neutral region). The contribution of the latter to the total dark current is generally negligible, particularily at low bias voltage. The maximum rate of carrier injection into the surface occurs close to the metallurgical junction then they drift along the surface channel created by band bending. To calculate this current we adopt a similar approch to that of Dodd et al. [61], besides we are able to estimate the electric field at the surface of the depleted layer using a simple analysis. This model is based on the Fermi level pinning phenomenon.

In the case of an *n*-type semiconductor a number of electrons from the conduction band will fill the surface states which lie below the Fermi level,

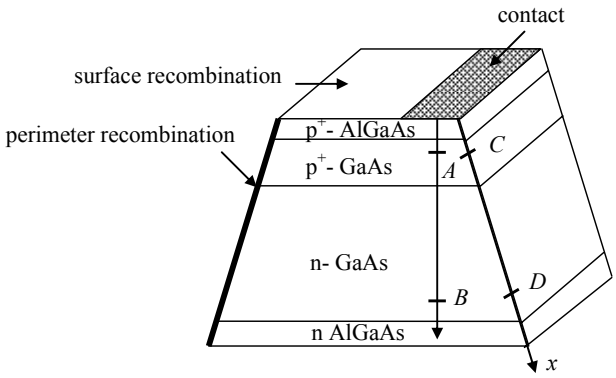

Figure 37 Schematic of a *n-p* mesa heteroface diode structure. The band diagrammes of Figure 38 are along AB (Bulk) and CD (surface). The analysis of Eq. (74) and the subsequent equations is along the *x*-axis.

then the surface will acquire a negative charge. This will cause a depletion region from which almost all electrons are removed and creation of an electric field directed towards the surface so as to oppose the flow of more electrons into the surface states. The result will be that the energy of the surface is raised with respect to the bulk (surface band bending). In order to maintain equilibrium between the surface and the bulk an electron current of magnitude en_sS_0 (where n_s is the surface electron density), must flow to the surface to replace the carriers that are lost due to recombination. In addition to the electron current, a hole current of equal magnitude must also flow to the surface. The position of Fermi level E_{Fn} and E_{Fp} of electrons and holes, respectively are determined by the applied voltage as well as the charge of the depletion layer which is equal and opposite to the charge on the surface. When the applied voltage is gradually increased from zero, as long as $p_s \ll n_s$ (p_s is the hole density at the surface), E_{Fn} remains constant and E_{Fp} moves downward by eV. When p_s becomes nearly equal to n_s and E_{Fn}, E_{Fp} are approximately equidistant from the band edges, both E_{Fn} and E_{Fp} approach the band gap edges at almost equal rates and p_s, n_s increase at approximately the same rate.

When the density of surface states N_s is high enough as in the case of GaAs, and when the energy position of surface states is mid gap, the surface Fermi level is almost pinned near mid gap at equilibrium ($V = 0$). When a forward bias voltage is applied, both quasi-Fermi levels move towards the band

edges at approximately the same rate. However, the average quasi-Fermi level E_F^*

$$E_F^* = \frac{1}{2}\left(E_{Fn} + E_{Fp}\right) \tag{69}$$

stays pinned at near mid gap. Figure 38a displays the energy band diagram of a *p*–*n* homojunction at equilibrium. Both Fermi levels of the *n*- and *p*- sides of the junction at the mesa surface are pinned near mid gap, therefore at equilibrium the edges of the valence and conduction bands are aligned throughout the structure. Consequently, the built-in potential drop along the surface is negligible and there is no electric field along the surface. As the applied forward bias is increased the average quasi-Fermi level at the surface of the space-charge region is pinned, and far from the junction (quasi-neutral regions) Fermi levels are pinned too. Since the emitter and the base thicknesses are considerably lower than hole and electron diffusion lengths, respectively (short diode case), E_{Fn} and E_{Fp} could not meet before reaching the contacts of the *p* and *n* regions. Thus we suggested that the energy band diagram of the structure could be represented by the diagram in Figure 38b, using a linear potential variation, where the edges of the valence and the conduction bands decrease linearly from the *n*-side to the *p*-side. In this case we could assume that the electric field at the surface may be approximated by a uniform electric field E_s with:

$$E_s \approx \frac{V}{H} \tag{70}$$

where H is the thickness of the active layer (emitter plus base). Note that, this approximation is used to determine the recombination current at the surface of the depleted layer.

The surface recombination rate can be described using the Shockley–Read–Hall statistics as:

$$R = N_s \frac{\sigma_n v_n \sigma_p v_p \left(n_s p_s - n_t p_t\right)}{\sigma_n v_n \left(n_s + n_t\right) + \sigma_p v_p \left(p_s + p_t\right)} \tag{71}$$

Where N_s is the density of surface states at level E_s, σ_n, σ_p, v_n and v_p are the capture cross-section and thermal velocity of electrons and holes respectively, n_t and p_t are the electron and hole densities when their respective Fermi levels are at the surface states level E_s.

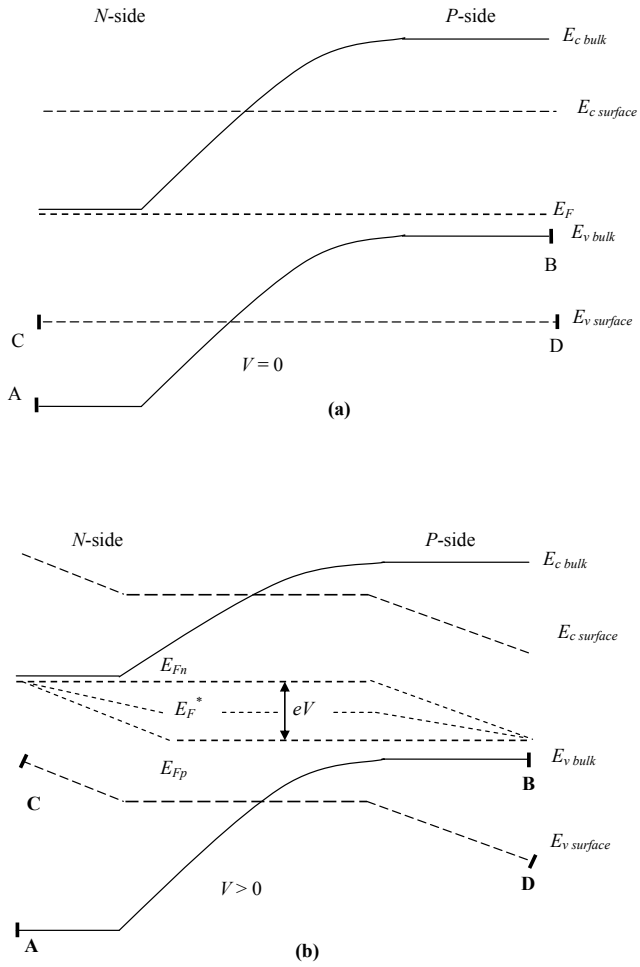

Figure 38 Energy band diagram of GaAs *p*-*n* junction, in the bulk along line AB in Figure 37 (solid lines) and at the surface along line CD in Figure 37 (dashed lines). (a) at equilibrium ($V = 0$); (b) under forward bias condition.

If we assume that E_s is close to the mid-gap level, then $n_t = p_t = n_i$ (deep defect levels as recombination centers). We also assume that the product σv is the same for electrons and holes, thus $\sigma_n v_n = \sigma_p v_p$. The electron and hole densities n_s and p_s apply to the surface. The surface is assumed to be sufficiently depleted so that $n_s p_s \gg n_i^2$, where n_i is the intrinsic carrier density. These assumptions allow to simplify Eq. (71) to:

$$R = S_0 \frac{n_s p_s}{n_s + p_s} \tag{72}$$

where $S_0 = \sigma v N_s$ is the surface recombination velocity. Here, N_s is the density of surface states assumed to be isolated deep levels and having energies uniformly distributed across the energy band gap.

With the same assumptions,

$$f_t = \frac{n_s}{n_s + p_s} \text{ and } 1 - f_t = \frac{p_s}{n_s + p_s} \tag{73}$$

Thus the knowledge of density of electrons and holes at the surface is necessary for determination of the recombination rate. In the model of surface recombination proposed by Dodd et al. [61], the band diagram is linearised around the position x_0 where the surface concentration of electrons and holes are equal: $n_s(x_0) = p_s(x_0)$. Together with assumption that $E_i = \frac{1}{2}\left(E_{Fp} + E_{Fn}\right)$ is constant in the depletion layer, it follows that:

$$n_s = n_i \exp\left(\frac{eV}{2kT}\right)\exp\left(-\frac{eE\left(x - x_0\right)}{kT}\right) \text{ for } x > x_0 \tag{74}$$

$$p_s = n_i \exp\left(\frac{eV}{2kT}\right)\exp\left(\frac{eE\left(x - x_0\right)}{kT}\right) \text{ for } x < x_0 \tag{75}$$

Where e is the elementary electron charge, V is the applied voltage and E is the electric field at x_0.

By integrating across the surface of the space-charge region we find the perimeter recombination current density J_{peri}:

$$J_{\text{peri}} = e \int_{-x_n}^{x_p} R(x)dx \tag{76}$$

where x_n and x_p are the edges of the space-charge region, the metallurgical junction is located at $x = 0$. Integrating (76) from $-\infty$ to $+\infty$, using (72), (74) and (75), the well known expression for surface recombination current is obtained:

$$J_{\text{peri}} = e n_i S_0 L_s \exp\left(\frac{eV}{2kT}\right) \tag{77}$$

$$\text{with } L_s = \frac{\pi kT}{2eE} \tag{78}$$

We can derive the perimeter current J_{peri} with a more rigorous approach, taking account of the finite integration interval ($-x_n$, x_p) of (76) and replacing E by E_s, the electric field at the surface. The expression of J_{peri} then becomes:

$$J_{\text{peri}} = en_i S_0 \exp\left(\frac{eV}{2kT}\right) \times \int_{-x_n}^{x_p} \frac{dx}{\exp\left(\frac{eE_s(x-x_0)}{kT}\right) + \exp\left(-\frac{eE_s(x-x_0)}{kT}\right)} \tag{79}$$

After integration we obtain

$$J_{\text{peri}} = en_i S_0 \exp\left(\frac{eV}{2kT}\right)\frac{k_B T}{eE_s} \times \left[\arctan\left(\exp\left(\frac{eE_s(x_p - x_0)}{kT}\right)\right) - \arctan\left(\exp\left(\frac{-eE_s(x_n + x_0)}{kT}\right)\right)\right] \tag{80}$$

It is verified easily that Eq. (80) reduces to the simpler expression (77) when x_p and $x_n \to \infty$. Adopting the fully depleted layer model of the space-charge region which is generally appropriate for junction solar cells, the values of x_n and x_p are calculated according to

$$x_0 = x_p - \sqrt{\frac{2\varepsilon_s}{e^2 N_A}\left(E_i - \frac{eV}{2} - kT\ln\left(\frac{N_v}{N_A}\right)\right)} \tag{81}$$

where N_v is the density of states at the valence band and E_i is the intrinsic level with respect to the valence band ($E_i \approx E_g/2$). The surface electric field E_s is computed using (70). A surface recombination velocity S_0 of 4×10^5 cm/s is used in the calculation.

Numerical simulation of the bulk properties of GaAs solar cell is carried out using the software SCAPS. The perimeter current density calculated using Eq. (80) is inserted into the bulk dark current density computed with SCAPS, thus the total current density is

$$I(V) = I_{ph} - \left(I_B(V) + \frac{P}{A}J_{\text{peri}}(V)\right) \tag{82}$$

I_{ph}, $I_B(V)$ are the photocurrent and the dark current densities obtained by SCAPS, $J_{peri}(V)$ is the perimeter recombination current density, calculated using Eq. (80), expressed in Ampères per centimeter and P/A is the perimeter to area ratio.

4.3.2 Details of the solar cell structure under analysis

The solar cell structure analysed is a heteroface GaAs similar to that grown by MOCVD technology by Tobin et al. [34] as displayed in Figure 39. It is composed of a double-layer anti-reflection coating of ZnS and MgF_2 on the top of an $Al_{0.83}Ga_{0.17}As$ window layer. The BSF layer consisted of a 1 μm $Al_{0.3}Ga_{0.7}As$ thick layer. This layer acts as a barrier to minority-carrier holes in the *n*-GaAs region, which increase their collection across the junction. The recombination velocity used at the front of the emitter was less than 4×10^4 cm/s and less than 4×10^3 cm/s at the back of the base layer [34]. The effect of the double anti-reflection coating is inserted as a data in SCAPS via its reflectance $R(\lambda)$ obtained from its experimental curve given in [34]. The absorption in this layer is neglected. The other material parameters, defect characteristics and optical data are adopted from Blood et al. [36], Adachi [40] and Blakemore [63] respectively.

In their experimental investigation, Tobin et al. [34] were able to obtain a best fit of the *I-V* dark characteristics with a double exponential model using the following expression:

$$I = I_{s1}\left[\exp\left(\frac{eV}{kT}\right)-1\right]+I_{s2}\left[\exp\left(\frac{eV}{2kT}\right)-1\right] \tag{83}$$

The cell area was 0.25 cm^2 with a perimeter to surface ratio P/A = 8 cm^{-1}. The obtained fitting parameters were: I_{s1} = 7.98×10^{-20} A/cm^2 and I_{s2} = 6.22×10^{-12} A/cm^2 (I_{s1} and I_{s2} are the saturation currents). The effect of series resistance was not included in the model (for currents below 10^{-2} A/cm^2 series resistance is negligible). The tests were carried out under standard conditions, 1-sun AM1.5, 1000 W/m^2 and T = 300 K. The short circuit current was about 27.89 mA/cm^2.

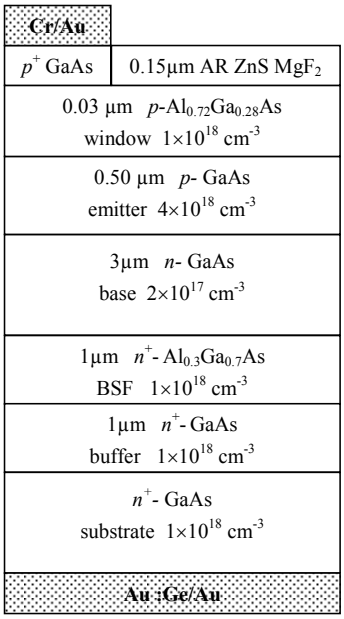

Figure 39 Schematic of the solar cell structure used in the analysis showing layer thicknesses and doping densities.

4.3.3 Perimeter recombination effect analysis

Figure 40 shows the dark and the illuminated current densities versus forward bias, both the fitted curve of Tobin et al. [34] and the simulated results are plotted. For low bias the effect of perimeter current is observable in the dark current, the curve with P/A = 8 cm^{-1} is closer to that of Tobin et al. [34] compared to P/A = 0 cm^{-1} curve. For low bias the perimeter current constitute more than 10 % of the total dark current. At high bias the three curves coincide, this means that the $n = 2$ current of the perimeter recombination current which originates from surface recombination outside the space-charge region is negligible and the results of SCAPS are correct. For this region of bias the bulk dark current is dominant, the $n = 1$ current is essentially due to minority carriers (electrons) diffusing into the quasi-neutral base. Thus the contribution of perimeter current to the dark current could not be neglected in the simulation of solar cells and particularly in small area solar cells. One-dimensional modelling does not consider this effect and error increases as the ratio P/A increases.

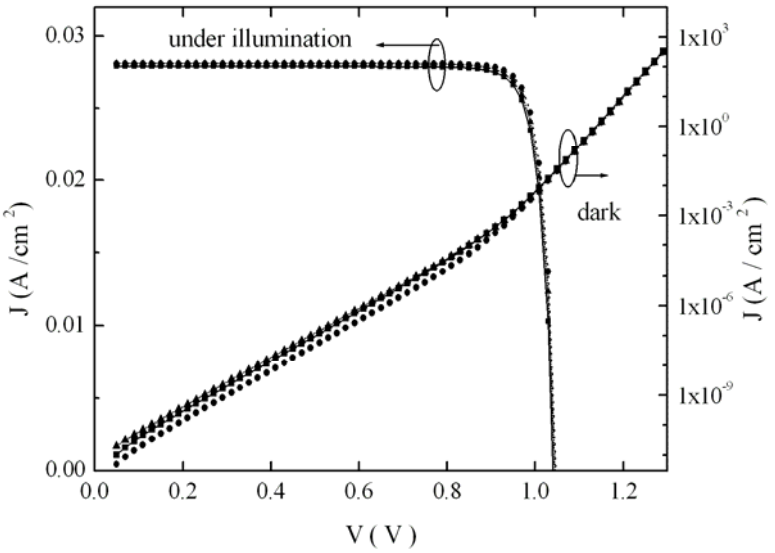

Figure 40 Dark current and illuminated current densities vs. voltage of 0.25 cm^2 cell. (■) experimental results of Tobin et al. [34]; (●) SCAPS Simulation with P/A = 0; (▲) P/A = 8 cm^{-1}.

To illustrate the effect of perimeter current on the cells' performance, the experimental, fitted and simulated photovoltaic parameters are listed in Table 4. In general the simulated results with the inclusion of perimeter effect are much closer to both fitted and experimental data of Tobin et al. [34].

Table 4 A comparison of photovoltaic parameters of a simulated 0.5×0.5 cm GaAs solar cell with experimental and fitted parameters of Tobin et al. [34] (A.M1.5 Global, 1000 W/m^2, 25° C).

	Experiment [34]	Fitted data [34]	P/A = 0 cm^{-1} (SCAPS)	P/A = 8 cm^{-1}
V_{oc} (V)	1.029	1.041	1.047	1.045
J_{sc} (mA/cm2)	27.89	27.89	28.1	28.1
FF (%)	86.43	87.17	87.89	87.07
η (%)	24.8	25.31	25.87	25.57

Part of the difference between experimental and fitted data could be assigned to series resistance, which was not included in the two diodes fitting model. This is equally true for the simulated results. The consideration of perimeter current into the calculation improves the efficiency estimation, instead of a relative error of 4.31 % we obtain 3.10 % with the perimeter effect included. This is not very significant, simply because the ratio P/A is too low to have a notable effect.

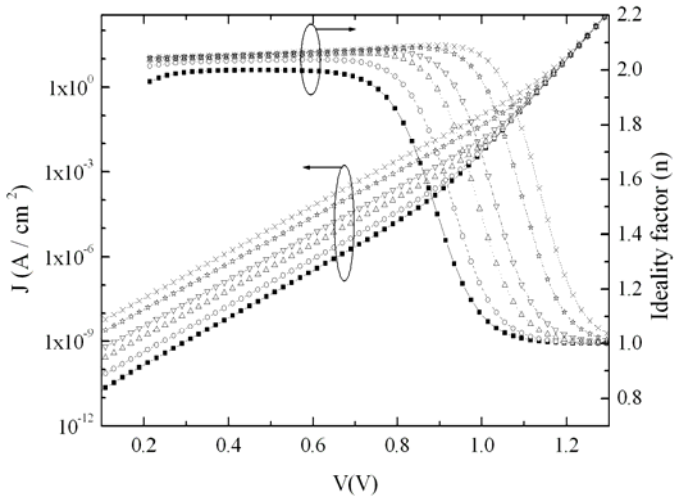

Figure 41 Dark current and ideality factor vs. Voltage of a GaAs solar cell with different P/A ratios. (■) SCAPS simulation P/A = 0; (○) P/A = 8 cm^{-1}; (△) P/A = 40 cm^{-1}; (▽) P/A = 100 cm^{-1}; (☆) P/A = 400 cm^{-1}; (×) P/A = 1000 cm^{-1}.

Dark current density and current ideality factor for different P/A ratios versus applied forward bias are shown in Figure 41, the curve P/A = 0 corresponds to the result of SCAPS without the perimeter effect. For a cell of 0.25 cm^2 the dark current is augmented by about 25 % when the perimeter effect is introduced. As the ratio P/A is increased the perimeter current takes over the bulk dark current. As the ratio P/A approaches 800 cm^{-1}, surface recombination current goes to three orders of magnitude higher than bulk recombination current. Recombination current in bulk space-charge region could be neglected for P/A > 100 cm^{-1} and the cell dark current is entirely due to perimeter surface recombination. The perimeter current at higher P/A ratios is characterized by an ideality factor slightly greater than 2 (about 2.1) for voltages above 0.8 V. This could be due to a vanishing depletion width,

leading to a slower increase of the perimeter recombination current than $\exp(eV/2kT)$ as in Eq. (80). From the curves of the ideality factor it can be remarked that the transition from $2kT$ to kT voltage is shifted towards higher values.

This is due to the sharp increase of the $n = 2$ perimeter current, and the other reason is the perimeter $n = 1$ current which is negligible and has no contribution to the $n = 1$ total current.

To examine closely the effect of perimeter current on the performance of small area solar cells we analyse the open circuit voltage (V_{oc}), the fill factor (FF) and the efficiency (η) of a number of solar cells with a P/A ratio varying from 0 (large area cells) to 10^3 cm^{-1} (40 μm × 40 μm). The results are shown in Figure 42. An apparent decrease of all photovoltaic parameters is observed. The most remarkable deterioration is recorded in the efficiency η, dropping from 25.87 % to 20.54 % for $P/A = 10^3$ cm^{-1} that is a relative loss of 20.6 %. This problem may be masked if monochromatic illuminating light with a wavelength corresponding to the maximum of responsivity is used. This solution was adopted by Ohsawa et al. [64] when they used a wavelength of $\lambda = 0.815$ μm which is close to GaAs fundamental absorption threshold of $\lambda_g = 0.86$ μm. The open circuit voltage and the fill factor drop from 1.047 V to 0.93 V and from 87.89 % to 78.57 %, respectively.

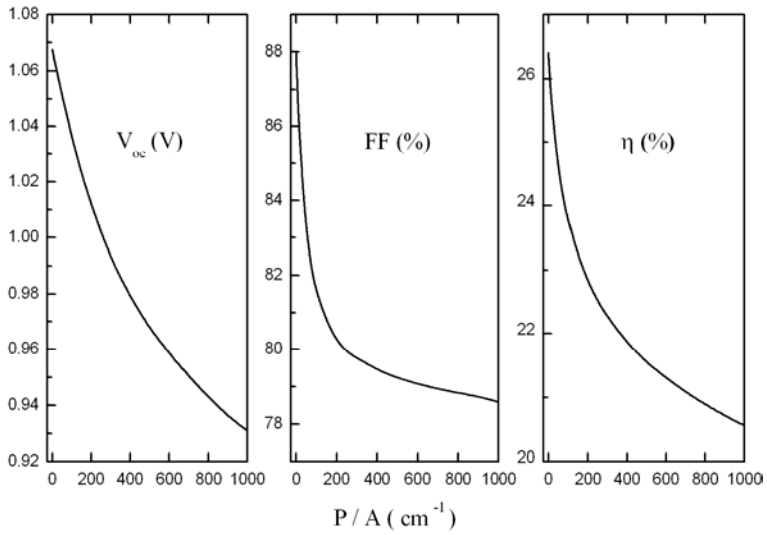

Figure 42 Open circuit voltage (V_{oc}), fill factor (FF) and efficiency (η) versus the perimeter-to-area ratio P/A.

Chapter 5

Electrical Characterization of GaAs Solar Cells

5.1 Introduction

The use of *pin* diodes instead of *pn* diodes is a common practise in thin film solar cells based on materials with rather poor semiconductor properties, such as the a-Si solar cell family. The better performance of *pin* cells as compared to *pn* cells is well documented for these cells, e.g. [47][65]. The improvement is ascribed to an apparent enhancement of minority carriers lifetime due to the electric field in the *i*-layer. However, a *pin* structure is also used with high quality III-V materials, e.g. GaAs and GaInP [66][67][68]. The motivation for a *pin* structure in GaAs based solar cells is unclear: sometimes a field enhanced effective minority carrier lifetime is invoked, as for a-Si cells [68]; in other cases, technological reasons are invoked [66].

In our PhD work, we had the opportunity to measure a set of GaAs based *pn* and *pin* solar cells, grown by MBE at the University of Heraklion, Crete, Greece. In this chapter we report on the electrical characterization under dark and illumination of these GaAs cell structures, and numerical modelling work to interpret the results. The aim of this work is to shed light on the role of the *i*-layer in GaAs based solar cells.

5.2 Structure and device technology

The GaAs samples were grown by MBE on a monocrystalline n^+-GaAs substrate, at the institute of Electronic Structure and Laser, in Heraklion, Crete, Greece (courtesy prof. Elias Aperathitis [68]).

To investigate the influence of the *i*-layer width (w_i) on the solar cell performance, three different samples were prepared in Crete and delivered to us: one *pn* cell, sample 1272 (w_i = 0 μm), and two *pin* cells with different intrinsic layer width: 1275 (w_i = 0.2 μm) and 1274 (w_i = 0.5 μm).

0.6 μm p^+-GaAs cap layer $N_A = 1\times10^{19}$ cm^{-3}
0.03 μm p-$Al_{0.8}Ga_{0.2}As$ window $N_A = 3\times10^{18}$ cm^{-3}
0.30 μm p-GaAs emitter $N_A = 3\times10^{18}$ cm^{-3}
i-GaAs, thickness w_i variable intrinsic
2.6 μm n-GaAs base $N_D = 1\times10^{17}$ cm^{-3}
0.11 μm n^+-$Al_{0.36}Ga_{0.64}As$/GaAs superlattice BSF $N_D = 2\times10^{18}$ cm^{-3}
1 μm n^+-GaAs buffer $N_D = 2\times10^{18}$ cm^{-3}
n^+-GaAs wafer substrate $N_D = 2\times10^{18}$ cm^{-3}

Figure 43 Diode structure of the *pn* and *pin* GaAs solar cells under study. The thickness of the *i*-layer was w_i = 0, 200 nm and 500 nm.

The structure of the samples is given in Figure 43. The back surface field (BSF) layer consisted of a 20-period superlattice of 2.8 nm wide $Al_{0.36}Ga_{0.64}As$ barriers and 2.7 nm wide GaAs wells. The use of a superlattice as a BSF layer is common practise in MBE GaAs based solar cells. A GaAs layer grown on such superlattice exhibits a better electrical interface than when the GaAs layer were grown on a bulk AlGaAs BSF layer [69]. Also, the superlattice BSF can act as a dielectric Bragg mirror for near infrared light. The role of the $Al_{0.8}Ga_{0.2}As$ window layer is to act as a front surface field layer (FSF), which decreases the effective surface recombination at the front surface of the cell.

An ohmic contact was formed to the back side of the n^+ GaAs substrate by evaporating and alloying AuGe layer followed by the evaporation of a Ni-Au contact. The front contact constitutes some technological challenge due to the presence of the AlGaAs window layer. First, a pattern for the front grid metallization was formed using standard photolithographic techniques. After etching the SiO_2 in the grid openings, TiPt, Pt and Au were evaporated for front contacts. Both contacts were activated in a rapid thermal annealing system at 400 °C for ohmic contact formation. For the case of heteroface cells with high aluminium content window layer, the direct contacting of this layer is possible but can be problematic in practice. Hence in GaAs solar cells technology, two different options have been developed. In the first one, windows are opened in the AlGaAs layer and the metal contact is evaporated directly on the GaAs region of the junction. In the second approach and the most successful one, a cap GaAs layer is grown on the top of AlGaAs window layer for contacting purposes and then etched off in the areas not covered by the metal grid [50]. Note that window layers with high aluminum content are prone to oxidation which leads to a degradation of the AlGaAs/GaAs solar cells. The degradation is mainly caused by the formation of oxides and other aluminum compounds which make the ohmic contacts unstable and therefore increase the contact resistance. A cross-section of the cells is shown in Figure 44.

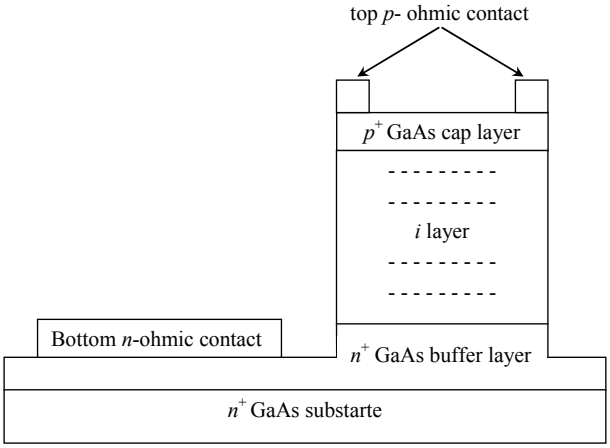

Figure 44 Cross-section of the solar cells and the contact structure. In this case, the contact has been deposited onto a GaAs cap layer. Before measurement, the cap layer has to be etched away from the active cell area.

The etching of the GaAs cap layer was done in the clean room ELINTEC of the University of Gent (courtesy Dr. Nadine Carchon, ELIS). The samples were etched in solution of 2:1:1 H_2O_2:NH_4OH:H_2O diluted in H_2O. This etching removed the GaAs cap layer everywhere except under the lines of the top contact grid. More details about the contact are shown in the top view of the diode in Figure 45.

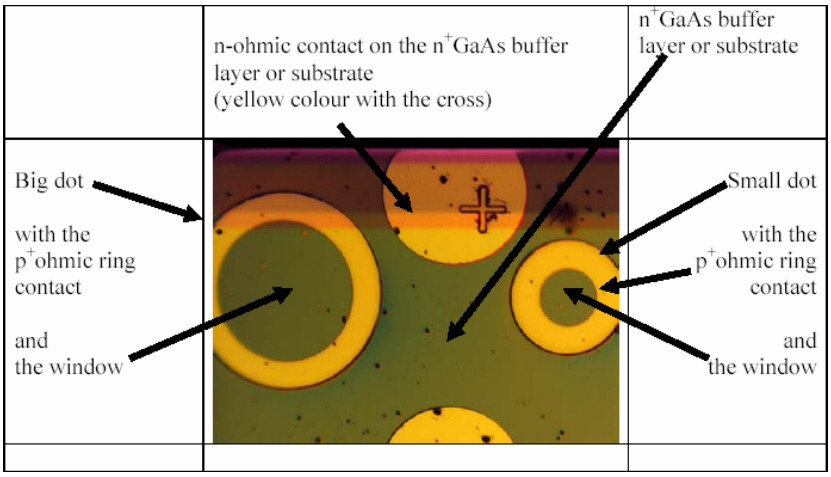

Figure 45 Top view of the GaAs solar cells with their contact structure from the Heraklion University.

5.3 Electrical characterization: results

5.3.1 Dark Characteristics

Figure 46 compares the *J-V* characteristics of the best cell from each sample. The diode ideality factor, derived from the slope of these curves at forward voltage, approximately equals $n = 2$. This is an indication that the dominant dark current mechanism is recombination-generation in mid-gap defects in the space charge layer (*pn* junctions) or the intrinsic layer (*pin* cells). We see in Figure 46 that the dark current of the *pin* cells is lower than that of the *pn* cell. As mentioned before, the reason for this is yet unclear. Possibly the quality of the weakly doped (or nominally undoped) *i*-layer is better than the quality of the strongly doped base and emitter layers. It is also possible that the presence of an electric field in the *i*-layer is reducing the recombination in that layer, and hence the dark current.

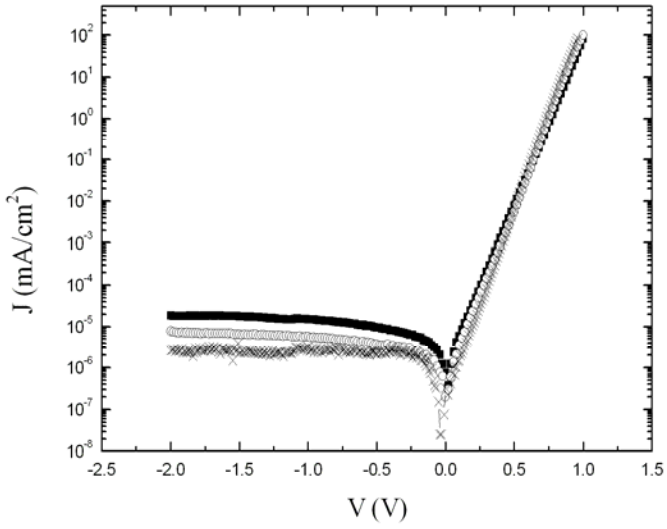

Figure 46 *J-V* curves measured in dark and at room temperature of one representative cell on each of the the three substrates. (■) sample 1272 (w_i = 0 µm); (○) sample 1275 (w_i = 0.2 µm); (×) sample 1274 (w_i = 0.5 µm).

By analyzing the dark *J-V* characteristics of Figure 46 we can quantify the apparent lower recombination in the *pin* cells compared to the *pn* cells. According to the Shockley-Read-Hall recombination theory and assuming the existence of recombination level near the mid-gap in the SCR, the recombination current can be expressed as:

$$J_{rec} \approx \frac{qwn_i}{2\tau_w}\exp\left(\frac{qV}{2kT}\right) \tag{84}$$

where w is the SCR width, τ_w is the lifetime of carriers in the SCR (*pn* cell, [7]) or in the *i*-layer (*pin* cell, [65]).

We can extract the value of

$$J_0 = \frac{qwn_i}{2\tau} \tag{85}$$

from the *J-V* curves by linear extrapolation the current to the zero-voltage axis. The thickness w follows from a capacitance measurement (see below), and the intrinsic concentration n_i in GaAs is well known in the literature. We thus could estimate the (effective) carrier lifetime inside the SCR or in the *i*-

layer: these values are presented in Table 5. We observe an increase of (effective) minority carrier lifetime with increasing intrinsic layer width w_i. This is compatible with the observed better solar cell performance, especially J_{sc} and V_{oc}, as is also displayed in Table 5 and will be discussed below.

Table 5 Room temperature (T = 300 K) solar cell parameters measured in dark (τ) and under A.M 1.5 illumination (V_{oc} , J_{sc}, FF and η). From each substrate, the best cell is represented.

	Sample	1272	1275	1274
	w_i (nm)	0	200	500
τ	ns	0.727	14.8	20.8
V_{oc}	mV	875.76	957.82	938.42
J_{sc}	mA/cm^2	17.18	20.70	20.97
FF	%	79.20	75.41	79.75
η	%	11.92	14.95	15.69

To further study the current mechanism, the current-voltage characteristics of all cells were also measured as a function of temperature. An example of such measurement is presented in Figure 47 for sample 1274 (w_i = 500 nm). We determined the activation energy of the reverse current for different values of the reverse voltage. The result is shown in Figure 48. For all samples, the activation energy determined in that way is hardly dependent on the reverse bias voltage, and its value is always close to the half of the band gap, thus $E_a \cong E_g/2$. This is a further indication that the dominant current mechanism is associated with recombination in centres near the middle of the energy gap.

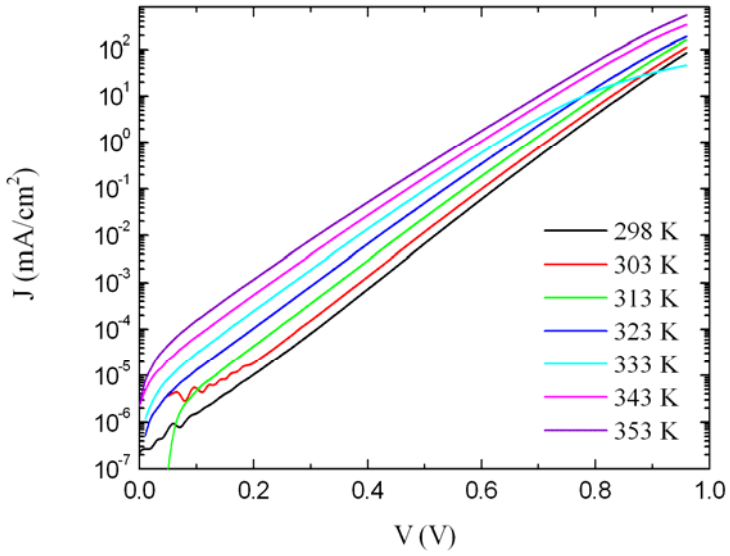

Figure 47 *J-V* characteristic of *pin* sample 1274 (w_i = 500 nm) measured at different temperatures above room temperature.

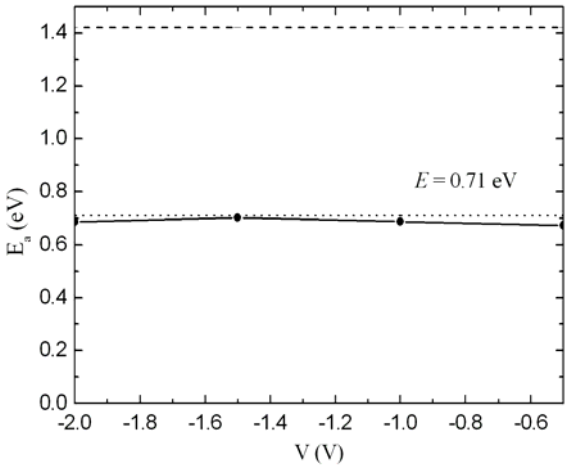

Figure 48 The variation of activation energy with reverse voltage for sample 1274 (w_i = 500 nm).

The capacitance voltage profile (*C*-*V* curves) for the three samples are presented in Figure 49. The total depletion layer width *W* is proportional to the inverse of the capacitance

$$W = \frac{\varepsilon_s \varepsilon_0}{C} \tag{86}$$

were *C* should be the capacitance per unit area.

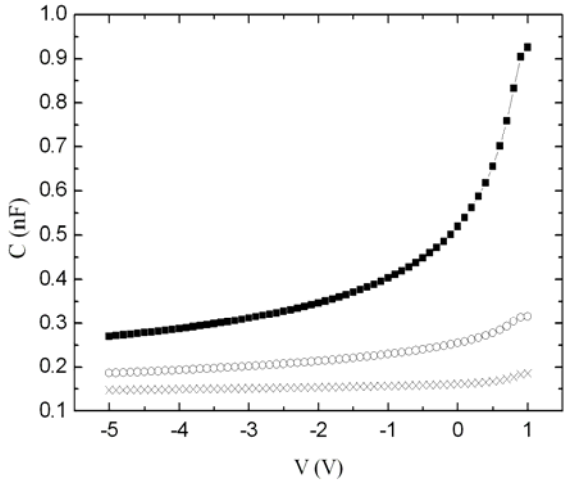

Figure 49 Capacitance-voltage curves of the three samples measured at f = 100 kHz. (■) sample 1272 (w_i = 0 μm); (○) sample 1275 (w_i = 0.2 μm); (×) sample 1274 (w_i = 0.5 μm).

The result is shown in Figure 50. In an asymmetrically doped *pn* cell, *W* is the depletion width at the weakest doped side of the junction; in this case, it should be the depletion width in the base layer. In a *pin* cell, *W* is the sum of the *i*-layer thickness w_i and the depletion width in the base (in this case). As the base is much stronger doped than the *i*-layer, *W* should approximately equal w_i and be independent of bias voltage (unless the *i*-layer is not completely depleted; this could be the case for a thin *i*-layer at high forward voltage). We see in Figure 50 that this is not really the case for the cell with w_i = 200 nm (*W* is dependent on *V* over the whole voltage range), and that it is more or less the case for the cell with w_i = 500 m. But then we should measure a *W* value slightly larger than 500 nm, and we measure $W \cong 300$ nm. We observed the same for several measurements on several different

cells on substrate 1274. This sheds some doubt on the validity of the fabrication data on the cells as communicated.

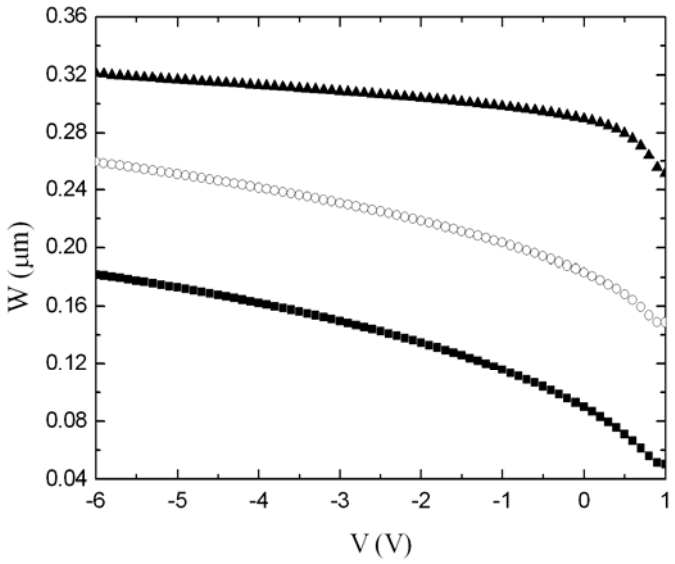

Figure 50 Total depletion layer width W deduced from the C-V measurements of Figure 49, for the three samples. (■) sample 1272 (w_i = 0 μm); (○) sample 1275 (w_i = 0.2 μm); (×) sample 1274 (w_i = 0.5 μm).

The apparent doping density was extracted from the classical Mott-Schottky plot ($1/C^2$ vs V) by taking the local slope of the curves. The resulting N-W profiles are presented in Figure 51. The apparent doping density in these cells is not uniform. An increase of the doping gradient from the junction to the bulk can be observed in Figure 51. The increase of the space charge region as function of the intrinsic layer width w_i is also be seen. Again, the apparent i-layer width of cell 1274 is ≅ 300 nm rather than the nominal 500 nm. The effect of the i-layer width w_i on the solar cell performance will be discussed in 5.3.2.

The doping concentration for the base region calculated from the C-V measurements was around 3×10^{17}cm^{-3} for sample 1272 and 1275 and around 4×10^{17}cm^{-3} for sample 1274, slightly higher than the nominal doping density of the n-type GaAs base region (Figure 43).

According to Ref [70] the non uniformity of the doping density determined from the *C-V* profiling as was observed in all the samples, can also be attributed to the presence of trap levels in the SCR.

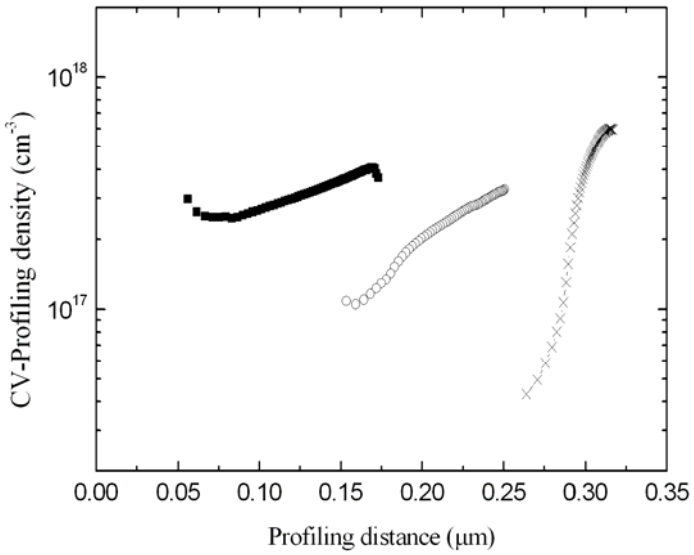

Figure 51 Apparent doping profile of the three samples deduced from the *C-V* measurements. (■) sample 1272 (w_i = 0 μm); (○) sample 1275 (w_i = 0.2 μm); (×) sample 1274 (w_i = 0.5 μm).

5.3.2 Solar cell characteristics under illumination

The *J-V* curves measured under illumination are given in Figure 52. The average efficiencies and standard deviation measured for each sample are summarized and shown in Figure 53. We observed a very good uniformity of efficiency across the samples in most cases. The photovoltaic parameters characteristics of the best cells measured for the three samples are reported in Table 5. All performance parameters J_{sc}, V_{oc}, *FF* and η are larger for the two *pin* cells then for the *pn* cell. The dependence of these parameters on the *i*-layer width w_i is less clear, and sometimes varies between the different cells on a substrate. This is also obvious from Table 6 were a typical cell on each substrate is chosen for comparison between measurement and simulation (see below). The highest cell efficiency measured was 15.69 %

which is quite comparable with the previously best reported solar cell fabricated from MBE material without an anti-reflection coating [71]. The external quantum efficiency *EQE* of the cells is shown in Figure 54.

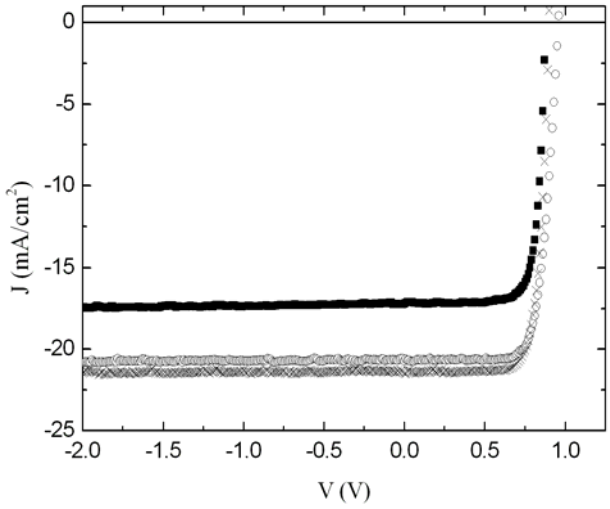

Figure 52 *J-V* characteristics of all samples measured under illumination. (■) sample 1272 (w_i = 0 μm); (○) sample 1275 (w_i = 0.2 μm); (×) sample 1274 (w_i = 0.5 μm).

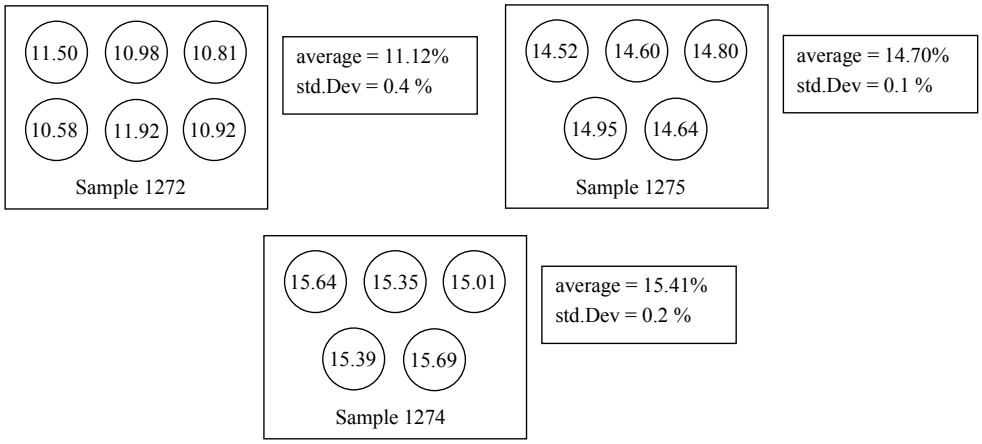

Figure 53 Efficiency map of all samples showing average efficicency and standars deviation. Sample 1272 (w_i = 0 µm); sample 1275 (w_i = 0.2 µm); sample 1274 (w_i = 0.5 µm).

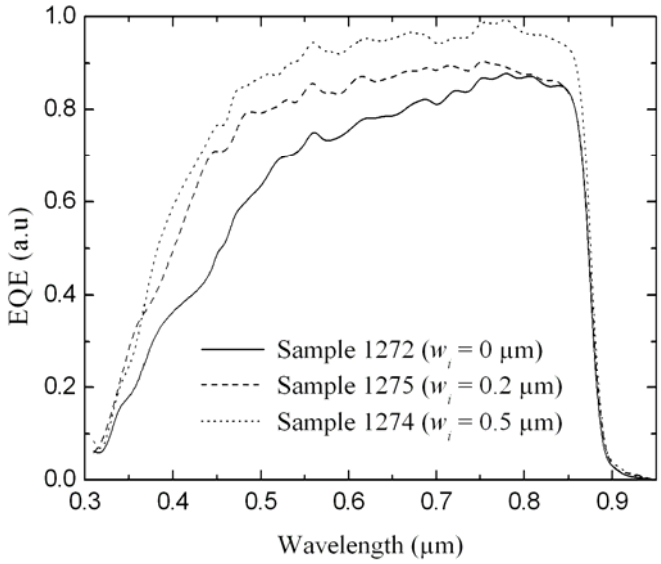

Figure 54 Measured external quantum efficiency *EQE* of all samples: 1272 (w_i = 0 µm); sample 1275 (w_i = 0.2 µm); sample 1274 (w_i = 0.5 µm).

In all cases, the measured V_{oc} is consistent with the dark *J-V* measurement in the sense that a higher V_{oc} corresponds to a lower dark current *J* and a larger value of the effective or apparent minority carrier lifetime τ (Figure 46 and Table 5). This can be understood from [72]:

$$V_{oc} \propto \frac{kT}{q} \ln\left(\frac{J_{sc}}{J_0}\right) \tag{87}$$

where J_0 is the saturation current density and J_{sc} the short circuit current density: an improvement in V_{oc} is associated with a reduction of J_0. And a reduction of J_0 is associated with an increase of apparent minority carrier lifetime τ (85). It is however not possible with such analysis to determine the cause of an increase of apparent lifetime: field enhanced transport through the *i*-layer or a better material quality of this *i*-layer. We will attempt to study this further with numerical simulations.

5.4 Simulation with SCAPS

The purpose of this simulation work is to check the hypothesis of reduced recombination in the *i*-layer due to the electric field in this region. Therefore we want to set-up a SCAPS problem definition that can simulate as good as possible our measurements: dark *J-V*, illuminated *J-V*, *C-V* and *QE*. Then we will be able to study the electric field and the recombination in the *i*-layer numerically as a function if the *i*-layer width w_i, and to check if the electric field alone can explain our measured trends, without any further assumptions about defect in the *i*-layer.

Setting up a problem in SCAPS or any other simulation programme means finding a large number of parameters describing the problem. From Figure 43 it is clear that our structure will contain at least six to seven layers. In each layers, a variety of parameters should be input: thickness *d*, band parameters E_g and χ, effective density of states N_C and N_V, thermal velocity $v_{th,n}$ and $v_{th,p}$, mobility μ_n, μ_p, shallow doping density N_D , N_D , defect characterisation (N_t, E_t, σ_n, σ_p, …), dielectric constant, optical absorption $\alpha(\lambda)$. Typically the number of input parameters largely exceeds 100. Even if many parameters are known from literature (this is fortunately the case for the well known GaAs-AlGaAs materials family), the number of unknown parameters remains high. In view of this excessive number of parameters, it is not realistic to expect that a decent parameter set, that very well fits all measurements, could be found in a finite time. We will have to downscale our ambitions to obtaining a more or less reasonable fit within a practical

time frame that was available for a part of a doctorate's work. We will esteem that a fit is reasonable when the characteristic features of a measurement are all reproduced (e.g. curve shapes, slopes, kinks, extremes,…); it is out of reach to obtain a simulation that would fit nicely through all measurement points. We will describe now the main lines along which we worked to obtain such reasonable simulation parameter set.

5.4.1 Obtaining a rough parameter set for simulation.

The starting point is of course the structure of Figure 43 with the values of the layer thickness and shallow doping density as reported by the colleagues of the University of Heraklion, who produced the cells. We treat the GaAs substrate and highly doped buffer layer as an ohmic contact. The base layer is split in two parts, a junction side part of 0.3 μm thickness and a bulk side part of 2.3 μm thickness. This has a purely numerical motivation: it is a way to ensure (in SCAPS) that there are enough mesh points in the base close to the *i*-layer (*pin* cell) or close to the emitter (*pn* cell). Without this, the simulation of the capacitance of the *pn* cell is very inaccurate. The materials parameters of the GaAs layers are taken from a text book, e.g. Sze [7]. In particular, the carrier mobilities are chosen as a function of the doping density ([7], p. 29, Fig.18): they vary with a factor 2 to 3 between the strongest doped and the weakest doped layer i.e. the emitter and the *i*-layer. The data for the two AlGaAs compounds come from the Ioffe Institute in Petersburg, Russia ([73]). The optical absorption $\alpha(\lambda)$ of GaAs is taken from Adachi [40]. For the window material $Al_{0.8}Ga_{0.2}As$ we use the Adachi-data for $Al_{0.804}Ga_{0.196}As$, as an $\alpha(\lambda)$ table for this composition is listed in [40]. For the $Al_{0.36}Ga_{0.64}As$/GaAs superlattice, we use 'effective properties' inspired on the information of the Ioffe Institute: see Appendix A.

Ohmic front contact optical property: reflection $R(\lambda)$ = parameter
non etched residue of cap layer, p^+-GaAs thickness = parameter; $N_A = 1\times10^{19}$ cm^{-3}
window, p-$Al_{0.8}Ga_{0.2}As$ $d = 0.03$ μm; $N_A = 3\times10^{18}$ cm^{-3}
emitter, p-GaAs $d = 0.30$ μm; $N_A = 3\times10^{18}$ cm^{-3}
intrinsic layer, i-GaAs thickness w_i = parameter, doping from in-diffusion
junction side of base, n-GaAs $d = 0.3$ μm; $N_D = 1\times10^{17}$ cm^{-3} + in-diffusion
bulk side of base, n-GaAs $d = 2.3$ μm; $N_D = 1\times10^{17}$ cm^{-3}
BSF, n^+-AlGaAs/GaAs superlattice: "effective material" $d = 0.11$ μm; $N_D = 2\times10^{18}$ cm^{-3}
Ohmic back contact

Figure 55 Structure of the *pn* and *pin* GaAs solar cells used for the SCAPS simulation. The parameters are discussed in the text.

We have no information about the defects (nature, density, energy levels, capture cross sections) in the semiconductor layers of our cell. A survey of deep states in GaAs layers grown by MBE was given by Blood and Harris [36]. They conclude that the dominant recombination in weakly doped *n*-GaAs is through a defect called 'M4' and which has an energy level $E_t = E_C - 0.5$ eV and an electron capture cross section $\sigma_n = 6.9\ 10^{-13}$ cm^2. We assume that this applies to the base layer (*pn* cell) or *i*-layer (*pin* cells) of our samples. We will assume that this defect is present in all GaAs layers of our cells, with uniform density N_t and with $\sigma_p = \sigma_n$. We then adapt the defect density N_t to simulate approximately the open circuit voltage of our cells. This is done in Figure 56 for the *pin* cell with $w_i = 200$ nm. We observe that $N_t = 4\times10^{13}$ cm^{-3} is a suitable value. We call the parameter set obtained in this way 'parameter set 1'.

This parameter set 1 is a first, rough parameter set that can serve as a starting basis for further refinement. From our methodology we can expect that this rough parameter set will roughly simulate the *C-V* measurement (if the

nominal geometry and doping conditions would apply to the real cell) and the open circuit voltage. However we have no reasons to expect that this rough parameter set will reproduce decently our other measurements (dark *J-V*, J_{sc}, shape of illuminated *J-V* (thus *FF*), *G-V*, *QE*). We now refine this parameter set in a few successive steps.

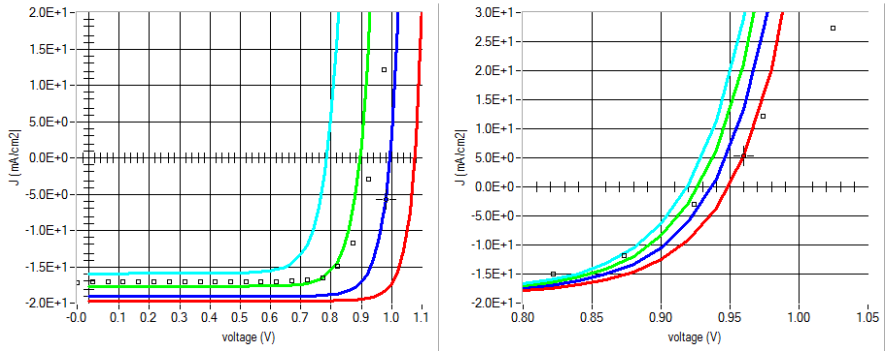

Figure 56 First tuning of the 'rough SCAPS parameter set' for the trap density N_t (uniform over all GaAs layers). The open symbols are the illuminated *J-V* measurement for cell 1275 (w_i = 200 nm). Left: N_t varies from 10^{12} cm^{-3} (red, best *J-V* curve) to 10^{13}, 10^{14} and 10^{15} cm^{-3} (cyan, worst *J-V* curve). Right: N_t varies from 7×10^{13} cm^{-3} (red, best *J-V* curve) to 5×10^{13}, 3×10^{13} and 1×10^{13} cm^{-3} (cyan, worst *J-V* curve). The value $N_t = 3\times10^{13}$ cm^{-3} is retained for parameter set 1.

5.4.2 Fitting the *QE*(λ) measurement: from parameter set 1 to 2 and 3

In Figure 57, the measured external quantum efficiency *EQE* of cell 1275 (w_i = 200 nm) is compared with a SCAPS simulation of the internal quantum efficiency *IQE*. This SCAPS simulation is based on parameter set 1, but the trap density N_t in the bulk side of the base layer (Figure 55) is varied from 10^{12} cm^{-3} to 10^{15} cm^{-3}.

With parameter set 1, the shape of the quantum efficiency measurement *QE*(λ) cannot be fitted well: it lies between the cyan and the green curve in Figure 57. We will refine parameter set 1 to parameter set 2, where N_t is set to 2×10^{12} cm^{-3} in the bulk-part of the base layer.

With this parameter set 2, and with a minimal cap layer thickness of 1 nm, we overestimate the light current and the quantum efficiency. A plausible assumption is that the cap layer was not etched away completely, and that d_{cap} > 1 nm. Indeed, the end-point detection of our etch process was 'on

sight', which might not have worked out perfect. In Figure 58, the d_{cap} value in SCAPS was varied from 1 nm to 100 nm (values 1, 2, 5, 10, 20, 50 and 100 nm); all other parameters had their value of parameter set 2. The simulation is compared to the measurement. We see that $d_{cap} \cong 5$ - 10 nm could better fit the blue part of the measurement ($\lambda < 450$ nm), whilst maintaining the $QE(\lambda)$ shape in the red part ($\lambda > 700$ nm) of the spectrum. Before we adopt such tuned d_{cap} value in a next parameter set 3, we will examine the optical behaviour of our cells in some more detail.

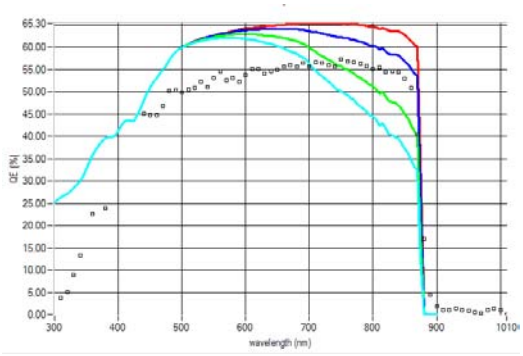

Figure 57 Measured (open symbols) external quantum efficiency *EQE* and SCAPS simulation (solid lines) of the internal quantum efficiency *IQE* of cell 1275 (w_i = 200 nm). The simulation is based on parameter set 1, where the trap density N_t in the bulk side of the base layer (Figure 55) is varied from 10^{12} cm^{-3} (red, best *QE*) to 10^{13}, 10^{14} and 10^{15} cm^{-3} (cyan, worst *QE*). A value $N_t = 2\times10^{12}$ cm^{-3} is retained for parameter set 2.

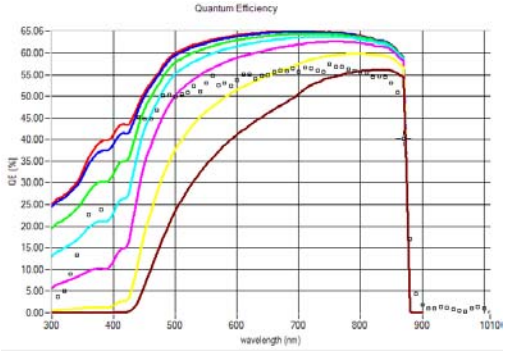

Figure 58 Simulation of the internal quantum efficiency *IQE* with parameter set 2 (see text). The GaAs cap layer thickness is varied from 1 nm (upper curve, red) to 2, 5, 10, 20, 50 and 100 nm (lower curve, brown). The measurement of cell 1275 (*pin* cell, w_i = 200 nm) is shown as open squares.

Our cells are optical smooth crystals, and look rather shining and slightly coloured to the eye: they have a non-negligible reflection $R(\lambda)$. SCAPS has only very rough optical calculations implemented: the user can specify an optical filter (a reflection file with $R(\lambda)$ data or a transmission file with $T(\lambda)$ data) at both contacts; the light in the semiconductor layers is supposed to undergo one specular internal reflection at the back contact, and is extinguishing exponentially in the semiconductor layers, as specified by an $\alpha(\lambda)$ file. No interference or scattering is considered in SCAPS. In a first attempt we have specified the front contact reflection with $R(\lambda)$ data for a bare GaAs substrate. However, the GaAs substrate is coated with 30 nm of AlGaAs and an unknown thickness of a GaAs film (the residue of the cap layer). We had thus to calculate the reflection and transmission of a cap / window / GaAs bulk structure.

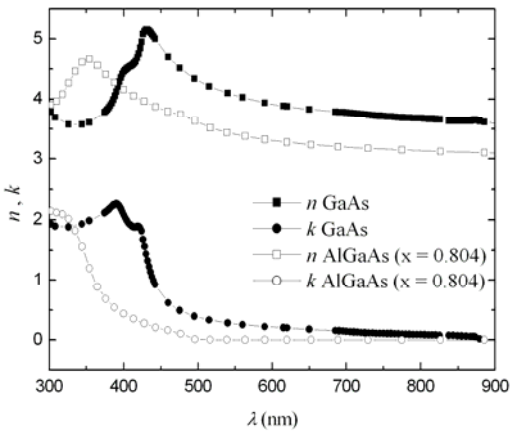

Figure 59 The index of refraction of GaAs and $Al_{0.804}Ga_{0.196}As$: the real part n and the imaginary part κ .

The optical data, the real and imaginary parts of the refractive index, thus $n(\lambda)$ and $\kappa(\lambda)$, of GaAs and $Ga_{0.804}Al_{0.196}As$ are taken from Adachi [40] (Figure 59). To calculate $R(\lambda)$ and $T(\lambda)$ of this structure, we used McLeod's method [74] (the 'ABCD matrix' method). The result is shown in Figure 60. We observe that the optical reflection $R(\lambda)$ strongly depends on the details of the optical structure, and that a cap layer of a few nm thickness has a large influence on $R(\lambda)$. Thus, we should vary (manually) the $R(\lambda)$ reflection file together with the cap thickness d_{cap} in the SCAPS simulations.

We now use the d_{cap} - $R(\lambda)$ combinations of Figure 60 in a SCAPS simulation of $EQE(\lambda)$; the result is shown in Figure 61. We see that our effort of a more detailed treatment of the optical behaviour of our cells is not rewarded with a better fit of the *EQE* curves. We obtain the best fit by assuming the reflection $R(\lambda)$ of a bare GaAs substrate, combined with a thin cap layer residue of $\cong$ 5 nm (Figure 58). Thus, in parameter set 3, we adopt $R(\lambda)$ of bare GaAs and d_{cap} = 5 nm.

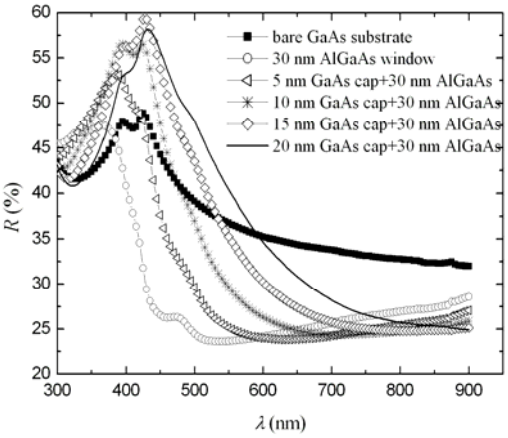

Figure 60 Calculated reflection from a bare GaAs substrate, a GaAs substrate with a 30 nm thick AlGaAs window, and an $Al_{0.804}Ga_{0.196}$ structure with GaAs cap layers of 5, 10, 15 and 20 nm thicknesses.

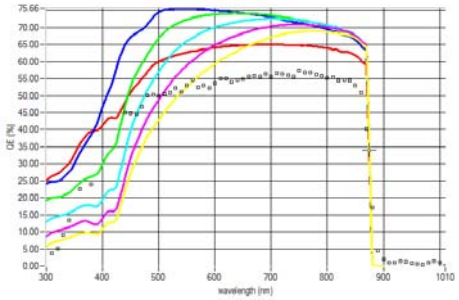

Figure 61 SCAPS simulation of *EQE* based on parameter set 2, with varying $R(\lambda)$ – d_{cap} combinations. Red: d_{cap} = 1 nm and $R(\lambda)$ of a bare GaAs substrate; Blue: d_{cap} = 1 nm and $R(\lambda)$ of GaAs substrate + 30 nm AlGaAs. Green to yellow: d_{cap} = 5, 10, 15 and 20 nm and the corresponding $R(\lambda)$ of GaAs + 30 nm AlGaAs + d_{cap} GaAs. The measurement of cell 1275 (*pin* cell, w_i = 200 nm) is shown as open squares.

5.4.3 Fitting the *CV* measurements: from parameter set 3 to 4

The parameter set 3 obtained so far can more or less simulate the shape of the *C-V* measurement, but the quantitative agreement between simulation and measurement is rather poor, see Figure 62.

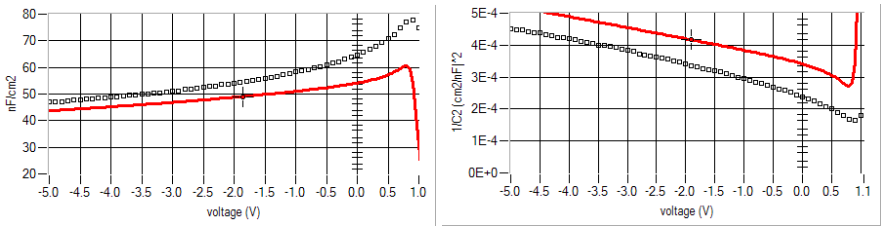

Figure 62 Measurement versus SCAPS *C-V* simulation. The measurement of cell 1275 (*pin* cell, w_i = 200 nm) is shown as open squares. The simulation is with parameter set 3. Left: $C(V)$ curves. right: Mott-Schottky plot $1/C^2(V)$.

To obtain a better fit, the doping profiles N_D (x) and $N_A(x)$ should be fine-tuned over the complete cell. We should realise that abrupt doping profiles as suggested in the structure of Figure 55 are not realistic: doping profiles will always be smeared out to some extent by diffusion during the high temperature process steps. Even the simplest case of interdiffusion turns out to be mathematically rather complicated. Suppose that we have two semi-infinite slabs, one for $x < 0$ with a uniform doping density N_{D01} and one for $x > 0$ with a uniform doping density N_{D02}. When interdiffusion of donors between the two media is allowed from $t = 0$ on, and with diffusion constant D, the diffusion profiles will be

$$\begin{aligned} N_D(x,t) &= N_{D20} + (N_{D0} - N_{D20}) \cdot \mathrm{erfc}\left(\frac{x}{\sqrt{2Dt}}\right), \; x \geq 0 \\ &= N_{D10} + (N_{D0} - N_{D10}) \cdot \mathrm{erfc}\left(\frac{|x|}{\sqrt{2Dt}}\right), \; x \leq 0 \end{aligned} \tag{88}$$

where erfc() is the complementary error function, and with

$$N_{D0} = \frac{N_{D01} + N_{D02}}{2} \tag{89}$$

It is noticed that the density at the interface has a constant value N_{D0} thoughout the transient. A snapshot of the diffusion profile is shown in Figure 63. SCAPS can handle solar cells with graded properties, including grading of the doping density N_D (x) and $N_A(x)$. Though many grading laws are implemented in SCAPS (linear, parabolic, logarithmic, exponential, power law, Beta function), two grading laws particularly interesting for diffusion phenomena are not implemented: the complementary error function erfc(ax) and a gaussian distibution function exp($-ax^2$). However, we see in Figure 63

that a simple exponential grading function is providing a very reasonable approximation to the erfc-profile.

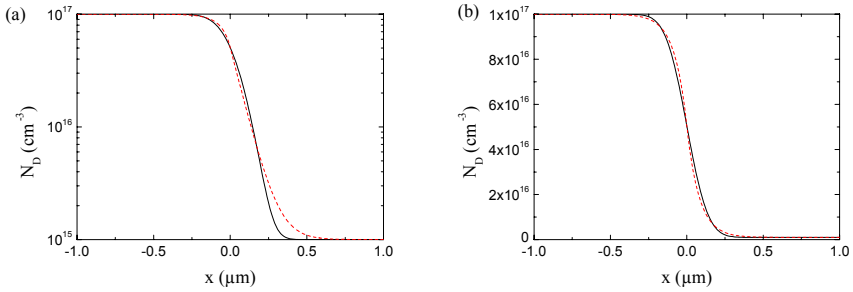

Figure 63 Interdiffusion profile of the doping density calculated with Eq. (88) and $N_{D01} = 10^{17}$ cm^{-3}, $N_{D02} = 10^{15}$ cm^{-3}, $D = 10^{-12}$ cm^2/s and $t = 2$ minutes (solid line). The exponential approximation $\exp(\pm x/L)$ with L = 80 nm is also shown, in red dashed lines. (a): logarithmic N_D scale. (b): linear N_D scale.

In our parameter set 3, the doping densities N_D and N_A were uniform in each layer. We changed these into exponentially graded doping profiles in the window, emitter, intrinsic and base layers. We varied the densities N_{D0} and N_{A0} (Eq. (88)) and the exponential decay length L at the left and right side of each layer. After experimenting quite some time with these parameters, we obtained parameter set 4, which gives a very reasonable fit of the *C-V* measurements, see Figure 64, and compare with Figure 62. The doping profiles N_D (x) and N_A(x) retained in parameter set 4 are shown in Figure 65.

Unfortunately this parameter set does not reproduce the *C-V* measurement of cell 1274 (w_i = 500 nm) and of the *pn* cell 1272 (w_i = 0) very well. This is very plausible for the *pn* cell: the high acceptor density diffusing out of the emitter now directly affects the base, since there is no *i*-layer as a buffer between emitter and base. However, also for the 1275 (*pn* cell, w_i = 200) cell slight adaptions to the doping profiles were necessary, and most important, w_i = 500 had to be used in the simulation. The doping profiles for cells 1272 and 1274 are shown in Figure 66.

A few more sophistications were introduced in parameter set 4. A discrete series resistance R_s and a discrete shunt resistance R_{sh} were necessary for a better fit of the conductance measurements $G(V)$. All doping profiles were not introduced in SCAPS as 'shallow doping', but as a 'defect'. This is because SCAPS assumes that shallow dopants are fully ionized, which might

not be the case for the doping levels here, that are comparable to the density of states N_C and N_V. We introduced the doping as a shallow defect: 6 meV below the conduction band for the donors (this is appropriate for typical donors S and Se [7]), and 30 mV above the valence band for the acceptors (this is appropriate for typical acceptors Mg and Zn [7]). These defects were given a low capture cross section ($\sigma_n = \sigma_p = 10^{-20}$ cm^2). This, together with the very shallow energy position, ensures that these 'defects' do carry charge and act as dopants, but do not contribute to the recombination.

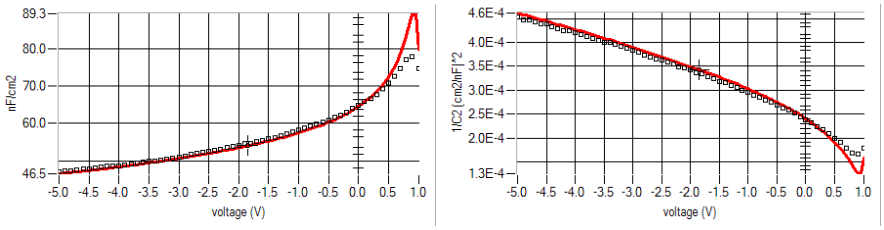

Figure 64 Measurement versus SCAPS *C-V* simulation. The measurement of cell 1275 (*pin* cell, w_i = 200 nm) is shown as open squares. The simulation is with parameter set 4, where the doping profiles of are implemented. Left: $C(V)$ curves. right: Mott-Schottky plot $1/C^2(V)$.

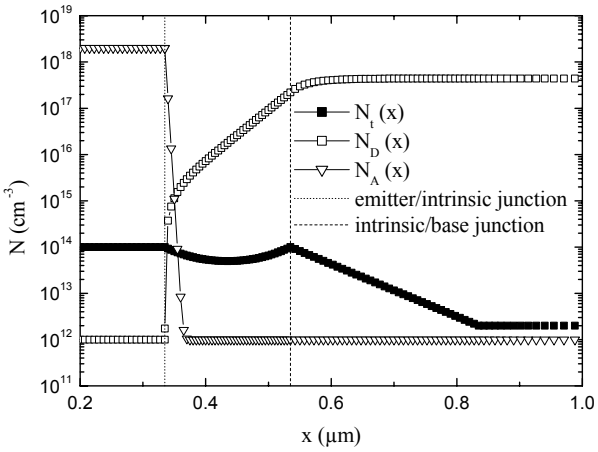

Figure 65 Diffusion profiles N_D (x) (□) and $N_A(x)$ (▽) set in parameter set 4 to simulate cell 1275 (*pin* cell, w_i = 200 nm). The defect density profile $N_t(x)$ (■) set in parameter set 5 is also shown.

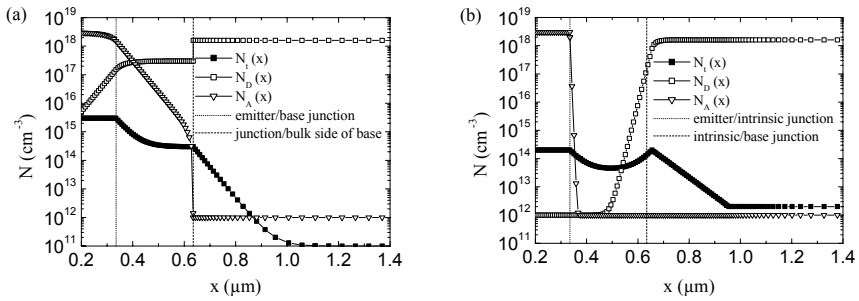

Figure 66 The diffusion profiles N_D (x) (□) and N_A(x) (▽) set in parameter set 4. The defect density profile N_t(x) (■) set in parameter set 5 is also shown. (a): profiles for cell 1272 (*pn* cell, w_i = 0). (b): profiles for cell 1274 (*pn* cell, w_i = 500 nm).

5.4.4 The final parameter set

The parameter set 4 now obtained is provide a reasonable good fit of the *C-V* and *G-V* measurements, while conserving the agreement with the *QE* measurements. However, the agreement between simulated and measured V_{oc} degraded somewhat compared to parameter set 1. Thus, a final tuning of the defect profiles N_t(x) was done to obtain parameter set 5, which is our final parameter set. In this fine tuning step, the recombination defects were given a concentration profile, the parameters of which were varied to obtain a decent fit of the dark and illuminated *J-V* curves. The N_t(x) profiles of parameter set 5 are already shown in Figure 65 and Figure 66.

The final fitting results are shown below: the dark *J-V* curves in Figure 67, the illuminated *J-V* curves in Figure 68, the *C-V* curves in , the *G-V* curves in Figure 69, and finally the *QE* curves in Figure 70.

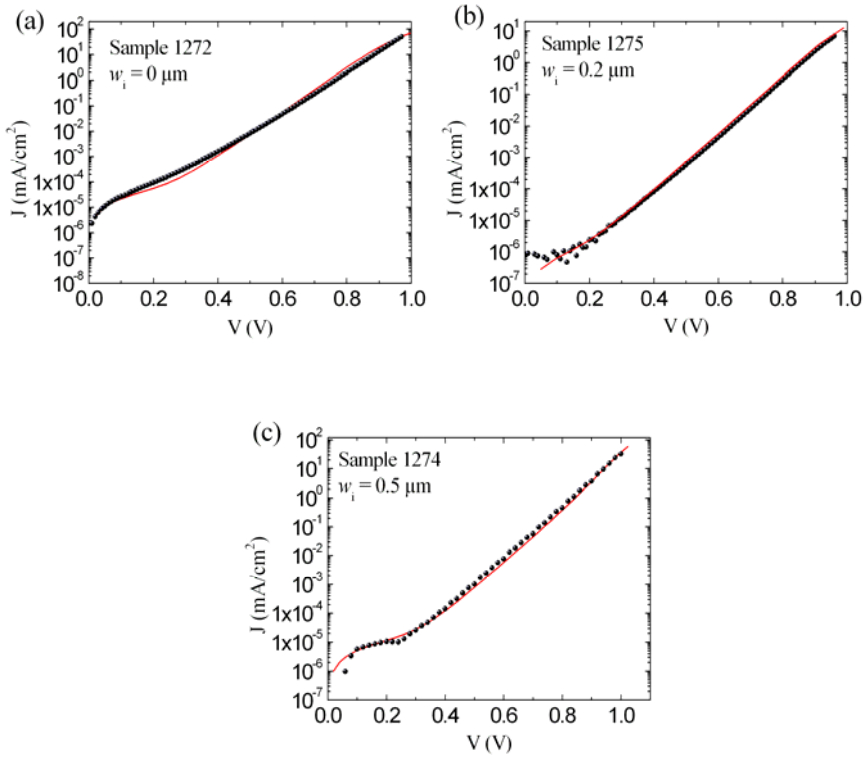

Figure 67 Dark *J-V* characteristics for all samples. Sample 1272 (w_i = 0 µm), sample 1275 (w_i = 0.2 µm), sample 1274 (w_i = 0.5 µm). Full circles: measurement points; solid lines: SCAPS simulation with the final parameter set 5.

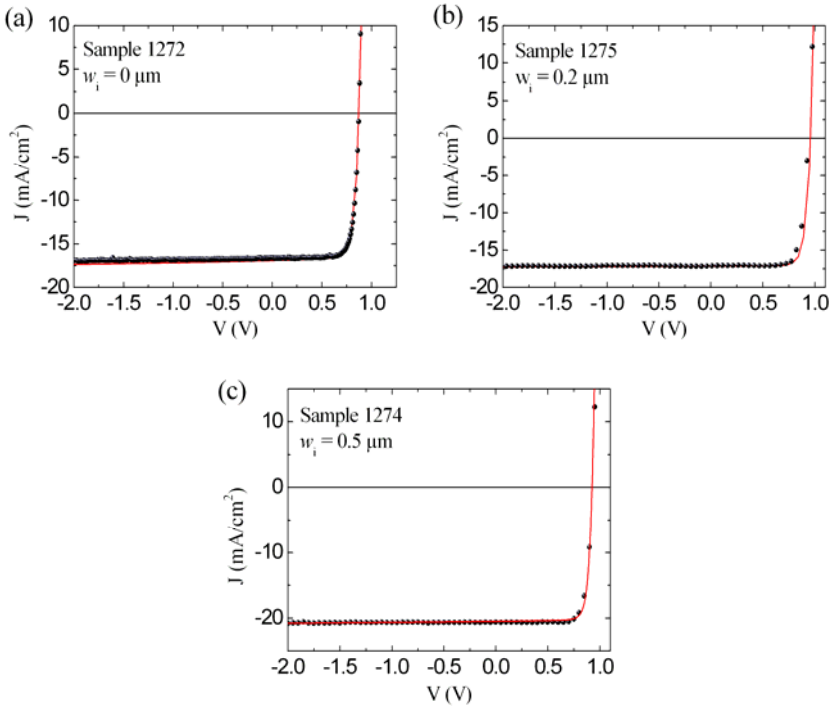

Figure 68 *J-V* charactersitic of all samples under illumination condition, A.M 1.5 and T = 300 K . Sample 1272 (w_i = 0 µm), sample 1275 (w_i = 0.2 µm), sample 1274 (w_i = 0.5 µm). Full circles: measurement points; solid lines: SCAPS simulation with the final parameter set.

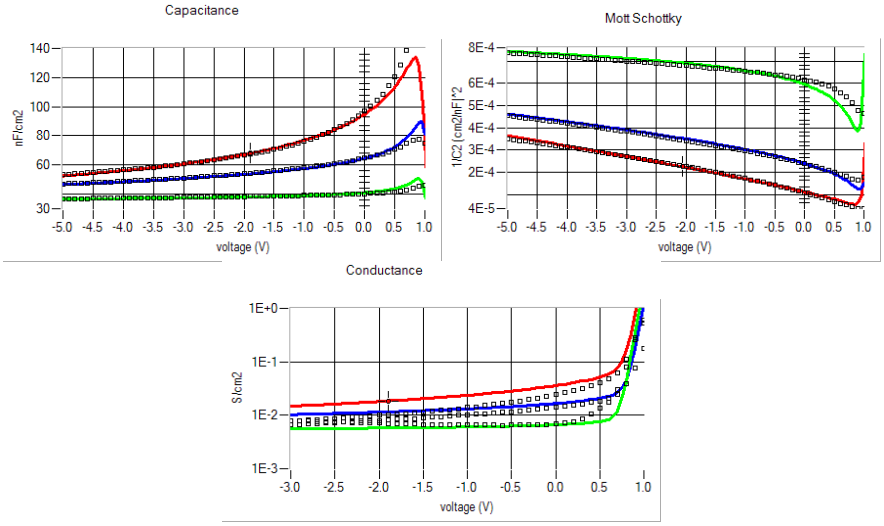

Figure 69 Capacitance *C-V*, Mott-Schottky ($1/C^2$ vs. *V*) and conductance *G-V* charactersitics of all samples in dark, and for $T = 300$ K and $f = 1$ MHz. Red: Sample 1272 ($w_i = 0$ µm). Blue: sample 1275 ($w_i = 0.2$ µm). Green: sample 1274 ($w_i = 0.5$ µm). Full circles: measurement points; solid lines: SCAPS simulation with the final parameter set.

Table 6 GaAs solar cell outputs deduced from *J-V* characteristic (comparison between measurement and SCAPS simulation data). Values of series and shunt resistance used in SCAPS simulation are also shown.

Sample	Solar cell output	Measurement	SCAPS Simulation
1272 ($w_i = 0$ µm)	V_{oc} (V)	0.872	0.881
$R_s.A = 0.02$ Ω.cm^2	J_{sc} (mA/cm^2)	16.61	16.91
$R_{sh}.A = 4\times10^6$ Ω.cm^2	FF (%)	79.37	77.55
	η (%)	11.5	11.55
1275 ($w_i = 0.2$ µm)	V_{oc} (V)	0.943	0.959
$R_s.A = 0.7$ Ω.cm^2	J_{sc} (mA/cm^2)	17.13	17.13
$R_{sh}.A = 4\times10^8$ Ω.cm^2	FF (%)	80.9	81
	η (%)	13.08	13.3
1274 ($w_i = 0.5$ µm)	V_{oc} (V)	0.925	0.938
$R_s.A = 0.4$ Ω.cm^2	J_{sc} (mA/cm^2)	20.58	20.46
$R_{sh}.A = 4\times10^7$ Ω.cm^2	FF (%)	80.44	82
	η (%)	15.32	15.76

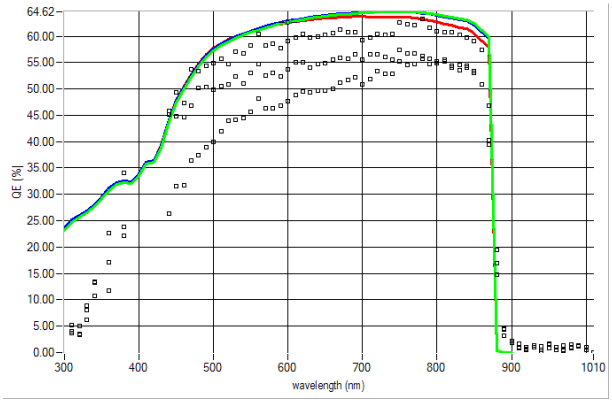

Figure 70 Simulated internal quantum efficiency *IQE* and measured external quantum efficiency *EQE* of all samples. Bias voltage $V = 0$, no bias illumination. Red: Sample 1272 ($w_i = 0$ µm). Blue: sample 1275 ($w_i = 0.2$ µm). Green: sample 1274 ($w_i = 0.5$ µm). Full circles: measurement points; solid lines: SCAPS simulation with the final parameter set.

The merits and shortcomings of this simulation work are obvious from these figures and from he remarks in the above discussion. The dark and light *J-V* measurements are fitted quite well, and also the capacitance measurements are simulated decently. The fitting conductance measuremenst is somewhat less good. The quantum efficiency is only simulated very roughly. Several reasons where already invoked for this. It is probable that a small residue (a few nm) of the GaAs cap layer remains after etching. This is considerably complicating the optical structure of the cell. We are not well enough equipped to carry out quantitatively reliable $R(\lambda)$ and $T(\lambda)$ measurements on these very small samples. Also, SCAPS has a rather rudimental treatment of the solar cell optics. All these may very well affect our parameter fitting of the quantum efficiency, and hence of the cell's short circuit current. However, we are convinced that these optical sophistications affect the electrical behaviour of the cell only to a minor extent. Also, we must observe a certain cell-to-cell and measurement-to-measurement variation of these *QE* and J_{sc} measurements. We thus will deem our obtained final parameter set as good enough for the purpose of this work: the study of recombination in the intrinsic layer.

5.5 Discussion of the numerical simulations

With the final parameter set for cell 1275 (*pin* cell with $w_i = 200$ nm), we will now numerically investigate the recombination in the cell for the

different *i*-layer thicknesses: we assign to w_i the parameter values 1, 200, 500 and 1000 nm (1 nm is the minimal layer thickness in SCAPS). Note that the case w_i = 1 nm will not reproduce the properties of the *pn* cell 1272 (w_i = 0), and that the case w_i = 500 nm (or 300 nm) will not reproduce our *pin* cell 1274 (w_i = 500 nm): for a good fit of cells 1272 and 1274 we hade to adopt different doping profiles N_D (x) and $N_A(x)$ and defect profiles $N_t(x)$. By keeping the N_D (x), $N_A(x)$ and $N_t(x)$ profiles of cell 1275, and only varying w_i in the simulation, we simulate the mere effects of thickness w_i and electric field in the *i*-layer, and not the effect of doping and defect profiles.

The simulated *J-V* caharcteristics under one sun AM1.5G illumination are shown in Figure 71. We see that V_{oc} is decreasing with increasing w_i: this is opposite to the trend of our measurements. We now want to numerically study the internal cell parameters $R(x)$ (the recombination), $E(x)$ (the electric field) and $n(x)$ and $p(x)$ (the carrier densities), especially in the intrinsic layer. We will not do this study at $V = V_{oc}$ for all w_i values: doing so, each w_i value would correspond to a different V, and hence different conditions for $E(x)$, $n(x)$ and $p(x)$, and hence $R(x)$ in the *i*-layer. In order to compare the recombination around V_{oc}, we will use the same applied voltage V = 0.9 V for all cells. In Figure 71 we see that this V value is below V_{oc} for w_i = 1 nm and 200 nm, almost precisely at V_{oc} for w_i = 500 nm and above V_{oc} for w_i = 1000 nm.

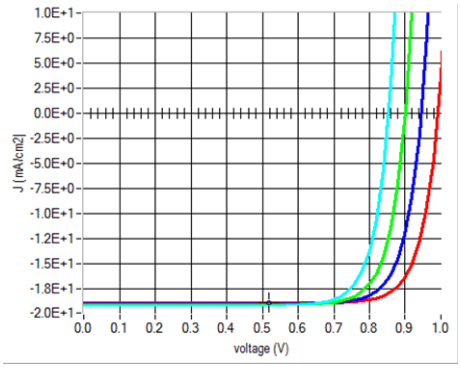

Figure 71 Simulated *J-V* characteristics under one sun AM1.5G illumination, with the final parameter set for cell 1275 (w_i = 200 nm). The parameter is the *i*-layer thickness: 1 nm (red), 200 nm (blue), 500 nm (green) and 1000 nm (cyan).

In Figure 72 (a) we plot the recombination $R(x)$ and in Figure 72 (b) the integrated recombination

$$R_{\text{integrated}}(x) = \int_0^x R(x')\,dx' \tag{90}$$

In Figure 73 (a) the electric field $E(x)$, and finally in Figure 73 (b) the carrier densities $n(x)$ and $p(x)$. All plots are focussing on the intrinsic region. The borders between the emitter and the *i*-layer, and between the *i*-layer and the base are also drawn.

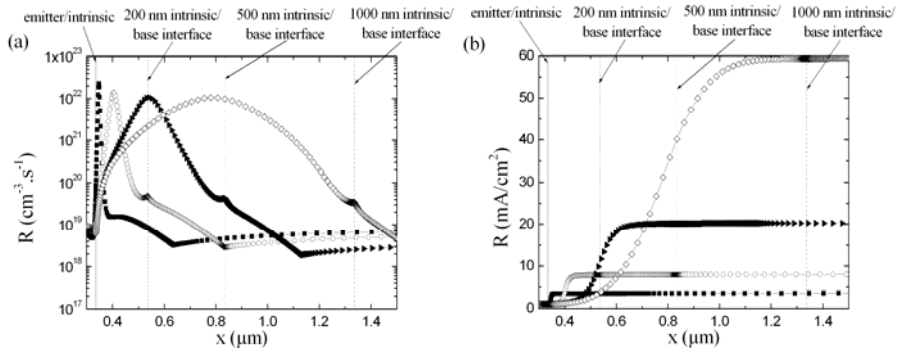

Figure 72 SCAPS simulation with the final parameter set for cell 1275 (w_i = 200 nm). The parameter is the *i*-layer thickness w_i: 1 nm (■), 200 m (○), 500 nm (▶) and 1000 nm (◇). (a): recombination rate $R(x)$. (b): integrated recombination $R_{\text{integrated}}(x)$ according to Eq. (90).

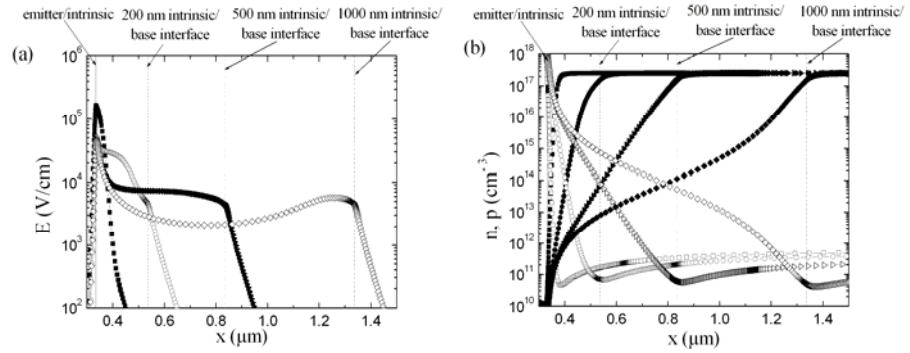

Figure 73 SCAPS simulation with the final parameter set for cell 1275 (w_i = 200 nm). The parameter is the *i*-layer thickness w_i: 1 nm (■), 200 m (○), 500 nm (▶) and 1000 nm (◇). (a): electric field $E(x)$. (b): the carrier densities $n(x)$ (full symbol) and $p(x)$ (open symbol).

These results can be understood with the standard equations for Shockley-Read-Hall recombination; these are similar to Eqs. (72), (77) and (78)

presented for surface recombination at the perimeter. We reproduce them here for the case of bulk recombination, with $\tau_n = \tau_p = \tau$ and for $E_t = E_C - 0.5$ eV $\cong E_i + 0.178$ eV:

$$R(x) = \frac{1}{\tau} \frac{pn - n_i^2}{p + n + 2n_i \cosh\left(\frac{E_t - E_i}{kT}\right)} \tag{91}$$

In the depletion layer or in the intrinsic layer, and under forward voltage bias, the *pn* product is very well approximated by

$$p(x) \cdot n(x) = n_i^2 \exp\left(\frac{qV}{kT}\right) \tag{92}$$

The maximum recombination is at the position x_0 where $p = n = n_0$. Assuming that this n_0 is larger than the cosh-term in Eq. (91) (in our case, that is if $n_0 = 2\times10^9$ cm^{-3}), the maximum recombination rate is

$$R_{\max} = \frac{n_i}{2\tau}\left[\exp\left(\frac{qV}{2kT}\right) - 1\right] \tag{93}$$

The total recombination current can then be obtained as in section 4.3.1, by linearising the energy bands around x_0 and integrating. The result is:

$$J_{rec} = \frac{qn_i}{2\tau}\frac{\pi kT}{qE}\left[\exp\left(\frac{qV}{2kT}\right) - 1\right] \tag{94}$$

This Eq. (94) states that the total recombination can be obtained assuming that the recombination rate has it's maximal value in a slab of width $\pi kT/qE$ and is zero outside.

The numerical results support these analytical approximations quite well. In Figure 72 (a) we see that the peak value of the recombination rate $R(x)$ is independent of the *i*-layer thickness w_i, as predicted by Eq. (93). Indeed, n_i, τ and V are the same for the four cells with different w_i (this is also the reason why we studied all cells at the same voltage, instead of each at it's own V_{oc}). It is also seen in Figure 72 (a) that the width of the $R(x)$ profile is decreasing, roughly as $1/w_i$; this is predicted by Eq. (94) and by an estimation of the electric field in the *i*-layer:

$$E \approx \frac{V_{bi} - V}{w_i} \tag{95}$$

The built-in voltage V_{bi} is somewhat lower than the band gap E_g, we take $V_{bi} \cong 1.4$ V. This, at $V = 0.9$ V, Eq. (95) estimates $E = 2.5$, 1.0 and 0.5×10^4 V/cm for $w_i = 0.2$, 0.5 and 1.0 μm respectively. The actual simulated $E(x)$ profiles (Figure 73 (a)) are lying somewhat below this rough estimate, but the trend 'E decreases with w_i' is confirmed. This is why the highest w_i value yields the highest recombination current J_{rec} (Eq. (94) and Figure 72 (b)) and thus the lowest V_{oc} (Figure 71). It is confirmed in Figure 72 that the recombination occurs almost exclusively in the *i*-layer, and assumption that underlies Eqs. (92) to (94). It is important to note that also in the *pn* cell with w_i = 1 nm, the recombination occurs in a high electric field region (the depletion layer). It can be seen that at the position of maximum recombination rate in the *pn* cell ($x_0 \cong 0.35$ μm, see Figure 72 (a)), the electric field is very high ($E > 5\times10^4$ V/cm, Figure 73 (a)). This field is higher than that in the *pin* cells, and thus the recombination current in the *pn* cell will be lower than that in the *pin* cells. This is confirmed in Figure 72 (b), and also in Figure 71 where we see that the *pn* cell has a higher V_{oc} than the *pin* cells.

Thus, our study confirms the conclusion that the presence of an electric field in the *i*-layer (or depletion layer, *pn* cell) reduces the recombination and improves V_{oc}. But it also shows that the highest field, the lowest recombination current and the highest V_{oc} occur in the *pn* cell, which is the limiting case of a *pin* cell for $w_i \to 0$.

However, in our measurements, we have observed the opposite trend. The measured characteristics of the two *pin* cells are better than those of the *pn* cell: lower dark current, higher V_{oc} and J_{sc} and thus efficiency. The features of lower dark current and higher V_{oc} are direct indications of lower recombination. Therefore, we must conclude that the two *pin* cells show reduced recombination due to their materials parameters and not because of the electric field in the *i*-layer.

We acknowledge that the belief in a reduction of recombination in an intrinsic region is wide-spread and in most cases well founded. This is definitely the case in *pin* cells based on amorphous or microcrystalline silicon. These materials have materials properties (minority carrier lifetime, carrier mobility or diffusion constant) that are far inferior to those if crystalline GaAs based materials under study here. In particular, the *p* nd *n*

layers of a-Si cells show a very high defect density, much higher that the intrinsic layer. The rationale for *pin* a-Si cells is thus clear: the cell operation should take place almost completely in the less defected *i*-layer, that should consequently be as wide as possible. However, also intrinsic a-Si is a rather defected material, whith short diffusion length L. This puts a limit to the practical *i*-layer width w_i. If there were no electric field in the *i*-layer, the above argument would limit w_i to about L: $w_i < L$. However, due to the electric field in the *i*-layer, this condition is relaxed to $w_i < 5L$ or so [65]. In all cases, it is not advantageous to widen the intrinsic layer beyond the optical absorption depth.

Now that we have derived a parameter set that reliably describes our GaAs *pn* and *pin* cells, we can do another numerical experiment to check the above statements for the GaAs case. The starting point is again our final parameter set for cell 1275 with w_i = 200 nm. To mimic the a-Si situation, we set the defect density very high, $N_t = 10^{18}$ cm^{-3} in all layers except the *i*-layer, where N_t is lower. We took $N_{t,i} = 10^{14}$, 10^{15}, …, 10^{18} cm^{-3}. For each $N_{t,i}$ value, we varied the *i*-layer thickness from 100 nm to 10 μm. We then simulated the illuminated *J-V* characteristics, and plotted the performance parameters V_{oc} , J_{sc}, *FF* and η as a function of *i*-layer thickness w_i. This is shown in Figure 74. We see that the improvement (or not) of the solar cell performance parameters by inserting a low-defective intrinsic layer between the highly defective emitter and base layers depends on the actual parameters.

There is an optimum *i*-layer thickness (that is, to optimise the efficiency) of 1 to 2 μm when $N_{t,i} \geq 10^{15}$ cm^{-3}. The short circuit current shows an optimal value for w_i = 3 to 4 μm, whereas the open circuit voltage only shows such optimal value for a much lower $w_i \cong 0.2$ μm, and only for a very defected intrinsic layer, that is $N_{t,i} = 10^{18}$ cm^{-3}. Since, in this numerical experiment, the materials quality does not depend on the *i*-layer thickness, the dependence of V_{oc}, J_{sc}, *FF* and η on w_i is brought about by the assumed better recombination properties of the *i*-layer compared to all other layers.

The difference in the behaviour $J_{sc}(w_i)$ and $V_{oc}(w_i)$ on the other hand is caused by the difference in the other determining parameters for recombination: the free carrier density n and p in the *i*-layer, which are higher in open circuit than under short circuit.

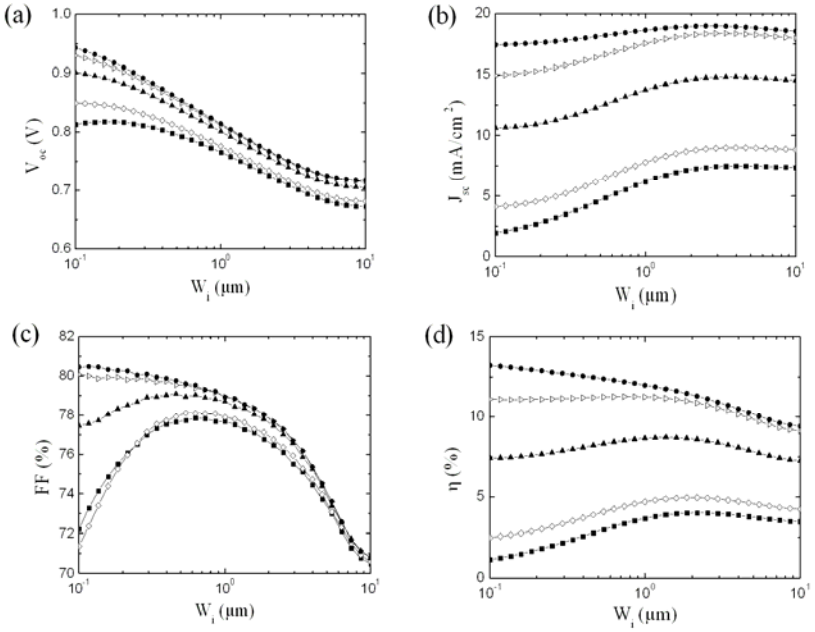

Figure 74 Numerical experiment to show the dependence of the solar cell performance parameters on *i*-layer thickness, based on the final parameter set. The defect density is high $N_t = 10^{18}$ cm^{-3} in all layers but for the *i*-layer, where $N_{t,i}$ varies from 10^{14} cm^{-3} (●) (best curce in all graphs) to 10^{15} cm^{-3} (▷), 10^{16} cm^{-3} (▲), 10^{17} cm^{-3} (◇) and 10^{18} cm^{-3} (■) (worst curve in all graphs). (a): open circuit voltage V_{oc}. (b): short circuit current J_{sc}. (c): fill factor *FF*. (d): efficiency η.

Chapter 6

Characterisation of CIGS thin film solar cells

6.1 Introduction

The CIGS absorber material belongs to the multinary Cu-chalcopyrite system where the band gap can be modified by varying the group III (on the periodic table) cations among In, Ga and Al, and the anions between Se and S [75][76]. The band gap range of interest for this technology is between 1 and 1.7 eV [77].

CIGS thin film solar cells are usually grown on glass substrate, but flexible CIGS solar cells are expected to be attractive due to their lightweight and flexibility. Among the tested metals are Cr-steels, Mo, Ti, Al, Cu and stainless steel (SS), but Cr-steel (low cost) and Ti (low weight) seem to be appropriate candidates. Higher conversion efficiencies have been achieved on metal foils with 17.5 % on SS [78] and 17.4 % on Ti [79].

In this chapter electrical measurements on flexible thin flim CIGS solar cells are reported. The cells were fabricated by the PVFlex company and the Helmholtz Zentrum Berlin (both Germany) and sent to the solar cells laboratory at the ELIS department (University of Gent) for electrical characterization. The main characterizations consist of current-voltage (*J-V*), quantum efficiency, admittance spectroscopy (AS) and deep-level transient

spectroscopy (DLTS) measurements. The results of this chapter have been reported in [82][83].

6.2 CIGS thin films solar cells grown on flexible metallic foils

Thin film solar cells with CIGS absorbers have obtained quite high efficicencies, up to 20 % [2], which is the highest efficicency obtained for any thin film cells. In these record cells, a glass substrate is used and the CIGS layer is deposited at a temperature of around 550° C. In all industrial developments going on to fabricate large CIGS modules, the substrate is always glass, and the CIGS deposition and/or annealing temperature is always in the 500 °C range. This elevated temperature is needed for the CIGS material to obtain excellent crystallographic and electronic properties, this causes a serious problem when CIGS cells have to be deposited on flexible substrate. Such substrates can distinct advantages over rigid CIGS cells on glass substrates: they are light weight, offer more possibility in building integration, can be advantageous for roll-to-roll production systems. However, the cell performance on flexible substrate is lower than on a glass substrate. When plastic foils are used as a substrate, a process temperature of around 550 °C is of course out of reach. With polyimide (PI) the process temperature can be as high as 420 °C [85], and the resulting CIGS absorber will be lower. When metal foils are used, a high processing temperature can be used in principle, but at the risk of out diffusion of impurities from the metal substrate into the CIGS absorber. Especially, iron (Fe) impurtities in CIGS are detrimental for the solar cell performance. Hence, all iron-based substrates (e.g. stainless steel foil) should be specially treated, e.g. with diffusion barrier layers. Other substrates (Ti or Mo foils) are showing less contamination issues, but can add substantially to the cell cost. Thus, it is clear that CIGS cells on flexible substrates offer also in their electronic operation from their countparts on glass substrates. The study of the internal electronic operation of CIGS cells on flexible metallic foil substrates is the subject of this chapter.

Flexible thin-film solar cells have attracted an important interest within the past years and several results have been reported on the development of flexible and lightweight copper-indium-gallium-selenide modules. Prime candidate for CIGSe flexible substrate are metals or polymers. CIGSe layers on PI (polyimide) substrates should be grown at low temperature. Therefore a poor crystal quality is obtained (small grain sizes) which is expected to increase recombination at numerous grain boundaries [82]. Unlike PI,

metallic foils offer the possibility to deposit the CIGSe absorber at temperatures similar or higher than those used for high-quality absorber on glass substrate.

6.2.1 Cell technology

The CIGS solar cell starts with sputtered molybdenum (Mo) on the substrate material (glass or metallic foil). The Mo film properties have to be optimized for adhesion, sheet resistance and morphology where it alloys sodium (Na) from the glass to diffuse through to the CIGS layer. Sodium aids the CIGS grain growth and increases the carrier concentration. Growth on non-Na-containing substrates requires the dosing of the CIGS film by introducing a 6 to 12 nm thick NaF layer on the Mo back contact or by introducing NaF during the CIGS deposition.

The growth of the *p*-type CIGS absorber layer can be done by co-evaporation from elemental sources or by the deposition of metal precursor layers and subsequent selenization. The deposition of precursor layers and the subsequent selenization is suited for large area processing because the individual steps are straightforward and compatible with thin film technology [83]. Co-evaporation of the elements offers a precise control of the source flux and generally it results in more homogenous absorber layers.

The heterojunction is then completed by chemical bath deposition (CBD) of CdS, followed by sputter deposition of a bilayer consisting of intrinsic and conducting ZnO, which is denoted as the window layer of the solar cell. In addition to that a Ni/Al grid is evaporated onto the finished devices in order to facilitate current collection. Figure 75 shows an image of flexible ZnO/CdS/Cu(In,Ga)Se_2 based solar cell device on a steel foil fabricated at the Helmholtz Zentrum, Berlin (HZB, Germany) (formely known as Hahn Meitner Institute (HMI)), as well as its SEM micrograph cross section taken at University of Gent. The sample shown in Figure 75 is one of serial samples sent by the company PVFlex (Fürstenwalde, Germany) to the ELIS department for electrical characterization.

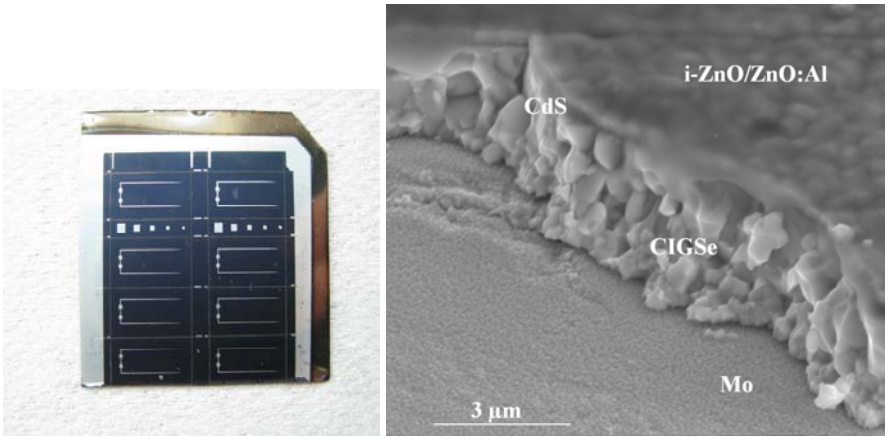

Figure 75 Flexible Cu(In,Ga)Se_2 thin film solar cell grown on steel foil. Cell fabricated at Helmholtz Zentrum, Berlin, Germany (sample 25) (at the left); and SEM (scanning electron microscope) image (at the right).

The CIGSe absorber layer of the cell shown in Figure 75 was grown using co-evaporation in a three-stage process. This process is known as the most successuful one and currently leads to the best solar cells efficiency. Figure 76 illustrates the three stage co-evaporation process as it is used at HZB. The three phases are identified by the sequence of metal selenides that are deposited onto the substrate. First, an $(In,Ga)_2Se_3$ precursor layer is grown at a substrate temperature $T_1 \cong 330$ °C. During phase 2, the In and Ga flux is turned off and only Cu and Se are evaporated at an elevated substrate temperature $T_2 \cong 525$ °C. After having reached the point of stoichiometry in deposition phase 2, i.e., [Cu]/([In] + [Ga]) > 1, Cu and Se evaporation are continued for a duration t_1. By turning down the Cu flux and taking back up the In and Ga evaporation rate, the deposition process enters stage 3, where the composition of the deposited layer is taken back into the Cu-poor regime. Thus, the Cu-content of the complete CIGSe layers is determined purely by the duration of the 3rd phase t_3 of the process.

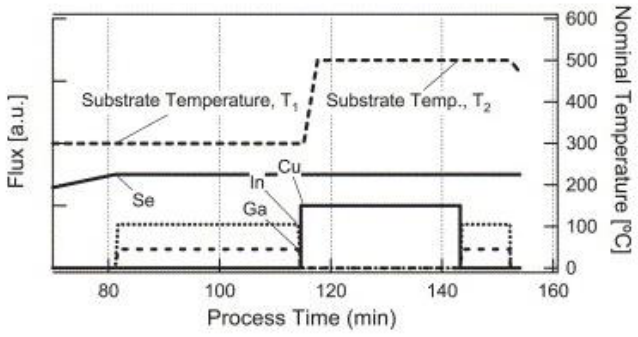

Figure 76 Schematic rate and substrate temperature profiles for a standard CIGS three stage co-evaporation process [85].

6.2.2 Defects in Cu(In,Ga)Se_2 solar cells: short literature survey

Investigation on shallow and deep defect levels in CIGSe based solar cells from optical and electrical characterization are very important for a better understanding the nature of these electronic defects, their origin and their influence on the device performances. The doping of $CuInSe_2$ is obtained by intrinsic defects. The Se vacancy V_{Se} is considered to be the dominant donor in *n*-type material and Cu vacancy V_{cu} the dominant acceptor in Cu-poor *p*-type material. Deviations from the the ideal $CuInSe_2$ stoichiometry introduces defects in the chalcopyrite lattice, e.g. incorporation of excess In results in unoccupied Cu-sites. These defect chalcopyrite phases have a tendency to segregate at the surface of polycristalline thin-films. In addition, the lattice defects (Cu vacancies) can have well defined positions, which has lead to the term ”ordered vacancy compound” or OVC. Two phases have been identified in literature, specifically $CuIn_3Se_5$ and $CuIn_2Se_{3.5}$. This OVC layer displays *n*-type conductivity and thus shows a type inversion at the CIGSe surface [86].

Table 7 sumarizes some intrinsic defects, their charge states, and associated energy levels as were calculated by Zhang et al. [87][88]. The table contains vacancies, two types of substantial defects (Cu on In site and In on Cu site) and one type of interstitial defects (interstitial Cu).

Experimentally two major defect levels have been detected in CIGSe devices and reported by several groups from deep level transient spectroscopy (DLTS) and admittance spectroscopy (AS) measurements. These defects are referred to as N1 and N2, and their origin is still under debate. Interpretation

of the nature of level N1 ranges from an electron interface trap [89], to a bulk compensating donor (In_{Cu}) [90], to a hole bulk trap [91]. The level N2 was attributed to a hole trap with a level about 270-380 meV [92]. It was shown that the concentration of that level is inversely proportional to the solar cell efficiency, thus it was considered as a major recombination center [93]. Recently, Igalson et al. [94] showed that N1 (and N2) is a combined response of interface states and bulk levels crossing the Fermi-level very close to the interface.

Table 7 Defect formation energies in $CuInSe_2$ and $CuGaSe_2$ as calculated by Zhang et al. [87][88].

Defect	Charge states	CGS ($M = Ga$)	CIS (M = In)
V_{Cu}	(- /0)	$E_V + 0.01$	$E_V + 0.03$
V_M	(- /0)	$E_V + 0.19$	$E_V + 0.17$
V_M	(2 - / -)	$E_V + 0.38$	$E_V + 0.41$
V_M	(3 - /2 -)	$E_V + 0.66$	$E_V + 0.67$
Cu_M	(- /0)	$E_V + 0.29$	$E_V + 0.29$
Cu_M	(2 - / -)	$E_V + 0.61$	$E_V + 0.58$
M_{Cu}	(0/ +)	$E_C - 0.49$	$E_C - 0.25$
M_{Cu}	(+ /2 +)	$E_C - 0.69$	$E_C - 0.34$
Cu_i	(0/ +)	$E_C - 0.21$	$E_C - 0.20$

6.3 Effect of metallic foils material on CIGS thin film solar cells performance

The main problem in CIGS solar cells grown on metallic foils is unwanted diffusion of impurities from the metal into the absorber, especially Fe which is known to have a very detrimental effect on the absorber quality. In order to reduce absorber contamination by diffusion of Fe or other elements, barrier layers such as SiO_x, Al_2O_3 or Cr can be applied on the metal foil substrate [95].

Several stainless steal substrates with different contact layers and with or without barrier have been supplied by PVFlex company (Berlin, Germany). The substrate structures were completed to CIGSe solar cells at HZB with

their standard process developed for CIGSe cell on Ti foil, which has lead to 16.2 % efficiency [85].

In this section we report on the electrical characterization of these cells in order to correlate the CIGSe cells properties with the substrate/treatment combination and investigate the nature of defects limiting or not the CIGSe solar cell performances. The main characterization consisted of room temperature and temperature dependent *I-V*, *C-V*, *QE*(λ). Defect levels investigation was performed by the means of Admittance Spectroscopy (AS) and DLTS (Deep-Level Transient Spectroscopy) measurements in a temperature range of 100 K to 360 K. The DLTS have been carried out in the Solid-State Sciences department of UGent (courtesy J. Lauwaert) using a Fystech 1030 Fourier Transform DLTS system in combination with a Leybold and Hereaus contact gas cryostat. Also, X-ray Photoelectron Spectroscopy (XPS) analysis were performed to investigate the presence or not of metallic impurities, diffused into the CIGSe absorber from substrate materials.

6.3.1 Absorber properties

The thicknesses of various layers of one of the samples (sample 25, see Table 8) as determined by SEM on cross section cut with a FIB (Focussed Ion Beam) are presented in Figure 77. The SEM image shows a 140 nm thick transition layer between the absorber and the back contact layer. This layer can be a $MoSe_2$ resulting from the reaction of Mo with Se during the deposition [96]. However, further studies are necessary to confirm this. The experiment also gives the thicknesses of all layers, this is an essential input to our interpretation and simulation work below.

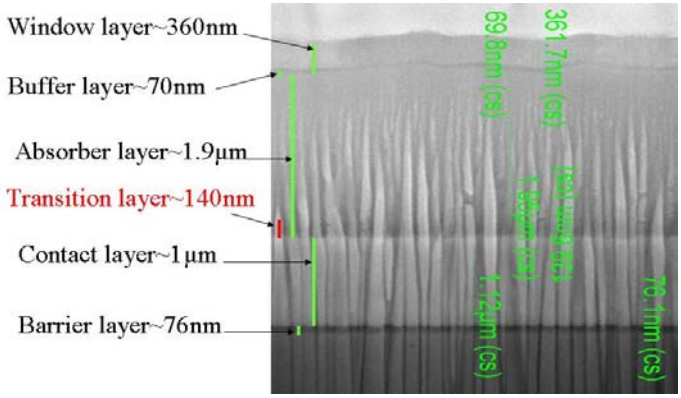

Figure 77 Scanning electron microscope (SEM) images of CIGSe solar cells grown on stainless steel foils at T = 525 °C (sample 25) done at ELINTEC, UGent. The columnar structure results from the ion beam preparation process, and does not reflect the grain structure.

6.3.2 Electrical characteristics

Four different samples were measured with different substrate/back contact combinations. The solar cells parameters of the best cells extracted from current–voltage characterization under dark condition are summarized in Table 8. The highest series resistance and shunt conductance were measured for a cell of sample 13, with series resistance $R_s.A$ = 1.47 Ω.cm^2 and G_{sh}/A = 9.48 mS/cm^2. Note that series resistance of 0.7 Ω.cm^2 is acceptable for devices with reasonable open circuit voltage [97].

Table 9 summarizes the best photovoltaic output parameters and standard deviation in efficiency measured under illumination conditions. The values of Cu and Ga content were measured at Helmholtz Zentrum using XRF (X-Ray Fluorescence) measurement. The statistics in Table 9 include all processed cells, removing one or two low efficiency cells from each sample. The best efficiencies were measured for samples 11 and 25 with a better efficiency uniformity being observed in sample 25. This can be attributed to the smoother surface of the steel used as a substrate for this sample. The smoothing (or polishing) was carried out to remove irregularities from the surface, which could be possible causes of pin holes and shunts during subsequent processing. Note that the metallic foil used as substrate in samples 25 and 13 was the same but in this latter without smoothing and with a CrN back contact layer.

Table 8 Solar cells parameters extracted from *I-V* measurements under dark conditions for various substrate/treatment combinations. (SS): Stainless steel; (S) Steel.

Sample	11	25	4	13
Steel foils	SS1 (polished)	S (polished)	SS2 (polished)	S (not polished)
Barrier Layer	Cr	Cr	CrN	CrN
Contact layer	Mo	Mo		
J_{01} (mA/cm^2)	7.8×10^{-8}	5.9×10^{-6}	3.5×10^{-7}	1.3×10^{-5}
n_1	1.6	1.4	1.5	1.5
$Rs.A$ (Ω.cm^2)	0.79	0.15	1.37	1.47
J_{02} (mA/cm^2)	1.9×10^{-4}	4.5×10^{-5}	2×10^{-4}	2.9×10^{-4}
n_2	2.24	2.2	2.4	2
G_{sh}/A (mS/cm^2)	1.05	0.26	0.28	9.48

Increasing Ga content should lead to an increase in the V_{oc} which is not the case for sample 13 with the highest value of gallium content (x = 0.4). The lower V_{oc} values measured for samples 4, 13 could be caused by the out-diffusion of substrate impurities into the absorber layer, since these cells were grown on steel substrate with the combined CrN back contact. It is also important to note that Cr from the CrN layer reacts with Se during the CIGSe deposition therefore affecting the absorber quality [98].

Table 9 Solar cells output measured for all samples. Ga and Cu content measured with XFR measurement at the Helmholtz Zentrum Berlin. III is the total content of group III elements, thus [In]+[Ga] and x is the Ga content: x = [Ga] / ([In]+[Ga]). T_1 = 330 °C ;T_2 = 525 °C (T1 and T2 are the temperatures of phase 1 and 2 respectively of the deposition process)

Sample	*Cu/III*	x	V_{oc} (mV)	J_{sc} (mA/cm^2)	*FF* (%)	η (%)	# Cells measured	Std.Dev. η (%)
11	0.88	0.35	589.2	33.64	69.72	13.82	8	1.71
25	0.88	0.39	560.6	34.85	70.1	13.69	13	1.53
4	0.88	0.34	465.5	32.62	64.6	9.8	5	0.66
13	0.89	0.40	443.6	36.95	40.74	6.7	13	0.72

In some cases, elements can diffuse from the barrier itself through the contact layer into the absorber [99]. Therefore, barrier layers can reduce the amount of diffusion elements from the metallic foil but are in general not perfect blocking layers.

From the external quantum efficiency measurements presented in Figure 78, it is clear that the band gap of CIGSe absorber is affected by the type of the substrate and the choice of back contact layers. A decrease in the spectral response in sample 4 is clear and probably due to an increase of recombination process inside the absorber. However, the increase in the spectral response in the spectrum range $800 \leq \lambda \leq 1000$nm observed in sample 11 shows a better quality of the absorber in this sample compared to the others. The shift in band gap observed in these cells could be due to a change in the maximum process temperature during the different stage of the deposition processes [101]. The temperatures referred in Table 9 are apparent temperatures, measured in the experimental set up and depends on the position of the thermocouple during the deposition process.

The doping density profile as determined by the standard Mott-Schottky analysis at 100 kHz for the best cell on each sample is displayed in Figure 79. The samples grown with a CrN back contact have higher apparent doping density (samples 4 and 13).

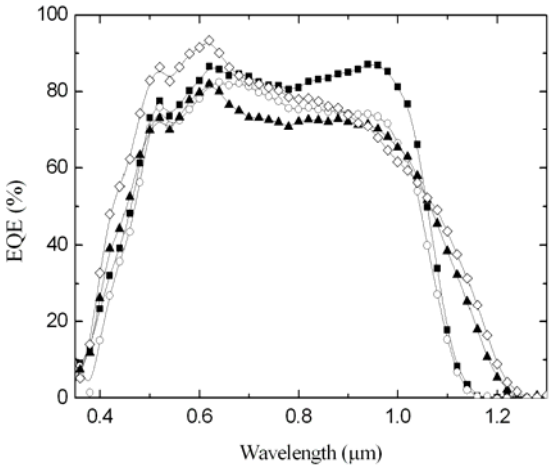

Figure 78 External quantum efficiency of all samples. (■) sample 11 (Mo/Cr/SS1); (○) sample 25 (Mo/Cr/S); (▲) sample 4 (CrN/SS2); (◇) sample 13 (CrN/S).

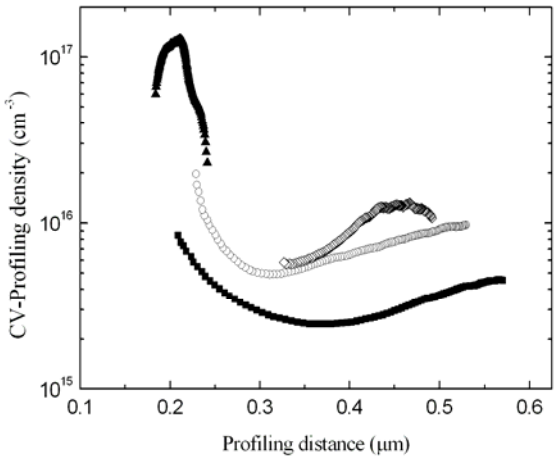

Figure 79 Apparent doping profile $N(x)$ from the C-V measurements at f = 100 kHz at room temperature. (■) sample 11 (Mo/Cr/SS1); (○) sample 25 (Mo/Cr/S); (▲) sample 4 (CrN/SS2); (◇) sample 13 (CrN/S).

Figure 80 shows the C-V behaviour of cell 11 (Mo/Cr/SS1). These measurements are fitted using Eq. (22) (Chapter 2) to obtain the built-in-voltage V_{bi} and the exponent β. All the cells have an exponent β higher than 2, which means that the doping is not uniform. Such highly non-uniform profiling density was also reported by others [102].

An increase in the apparent doping density towards the junction (with CdS) can be seen in these samples, in agreement with to what was reported in [102], and attributed to the presence of an acceptor level localised near the heterointerface. This agrees well with the capacitance-voltage-temperature measurement of sample 11 (Mo/Cr/SS1) shown in Figure 81. At higher temperature the acceptor level is discharge which lead to an increase of the SCR near the interface.

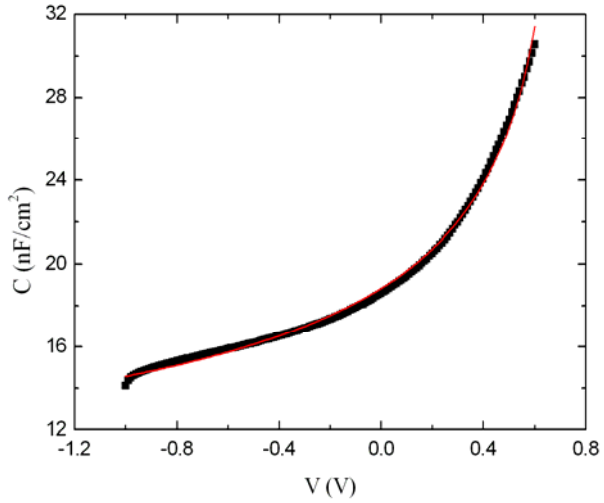

Figure 80 C(V) curve of cell 11 (Mo/Cr/SS1) measured at 100 kHz and room-temperature. The soild line represents a fit using Eq. 21, giving $V_{bi} = 0.73$ and $\beta = 3.36$.

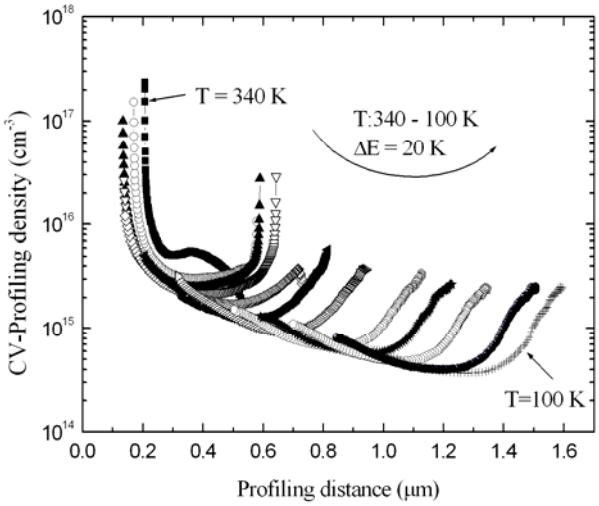

Figure 81 Doping profile of sample 11 (Mo/Cr/SS1) calculated from *C-V* measurements in temperature range 340-100 K in steps of 20 K and $f = 100$ kHz.

6.3.3 XPS analysis

X-ray Photoelectron Spectroscopy (XPS) profiling was done in the Solid-State Science Department of Ugent. The results of XPS profiling performed on sample 4 is shown in Figure 82. The concentrations of Cu, In, Ga, Se from the absorber layer, as well as Cr and Fe from the back contact layer and the stainless steel substrate respectively, are plotted vs. the sputter time. It can be clearly seen that there is a diffusion of Fe and Cr into the CIGS layer. Also, the inhamogenous distribution of Ga is apparent. There is gallium enrichment at both edges of the absorber, i.e. torwards the buffer layer and towards the contact. Ga accumulation near the back contact within the final CIGSe thin film has also been observed by other authors [102][103].

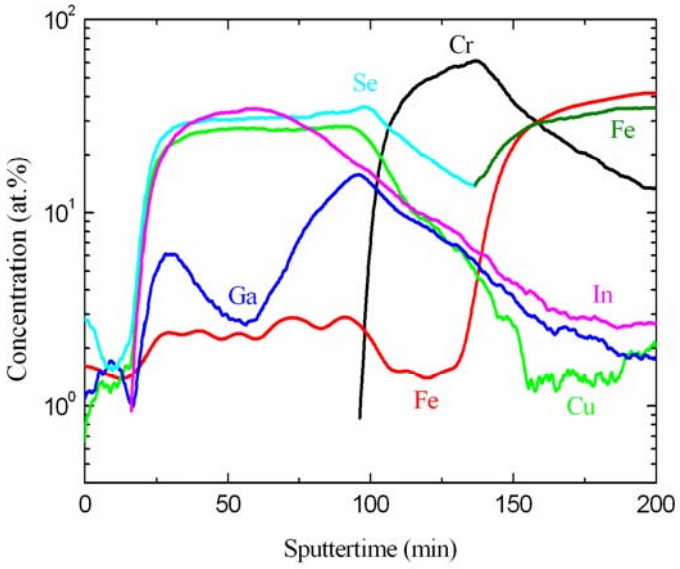

Figure 82 Concentration profile of sample 4 (CIGSe/CrN on SS foil) measured by XPS, X-ray photoelectron spectroscopy.

6.3.4 Current-voltage-temperature measurement under dark and different light intensities

Current-voltage-temperature measurements under dark and different light illimunation were performed to characterize the gap within the CIGS absorber and also the recombination mechanism occurring in these cells.

Figure 85 presents an Arrhenius plot of the saturation current $J_s(1/T)$ and Figure 88 a $V_{oc}(T)$ measurement, both of sample 25 (Mo/Cr/S). The activation energies extracted from Figure 85 and Figure 88 were approximatevely the same (~1.15 eV). However, the band gap of the absorber deduced from the external quantum efficiency (Figure 78) is 1.107 eV.

In Ref [104] the following expression was given to calculate the band gap of the absorber as function of the Ga content x ($x = \frac{[Ga]}{[Ga]+[In]}$):

$$E_g = 0.998 + 0.291x + 0.430x^2 \tag{96}$$

Thus a band gap of about 1.17 eV is calculated for sample 25 (Mo/Cr/S) using the measured value of x given in Table 9, which is quite equal to that deduced from the external quauntum efficiency. This indicate that the band gap of the absorber material is the relevant activation energy for recombination and also that the recombination in this cell takes place in the volume of the CIGSe.

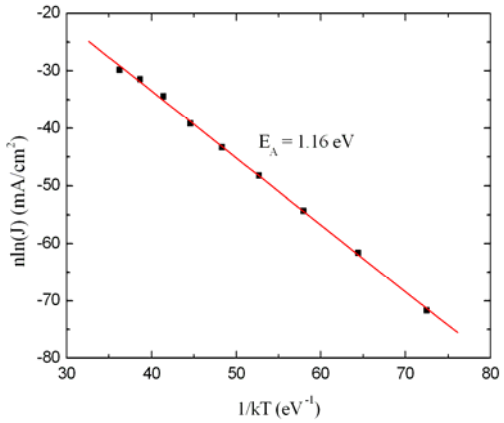

Figure 83 Arrhenius plot of the dark saturation current of sample 25 (Mo/Cr/S) shown an activation energy of E_A = 1.16 eV.

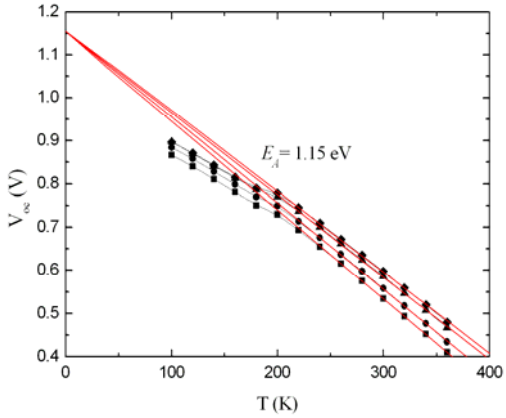

Figure 84 The temperature dependent of the open-circuit voltage of sample 25 (Mo/Cr/S) under different illumination intensity extrapolated at 0 K ($E_g \cong 1.15$ eV).

6.3.5 Defect spectroscopy

Admittance spectroscopy measurements were carried out on all the samples to investigate the presence or not of defects in these cells and their effect on the solar cells performances. Figure 85 shows capacitance-temperature measured at frequency of 100 kHz. A highest step from cryogenic to room temperature is observed in sample 4, which can be caused by a high concentration of deep defects.

Figure 86 shows the measured *C-f-T* curves for sample 11 (Mo/Cr/SS1). The frequency dependent increase of the capacitance for temperature above 100 K is due to the contribution of a trap level. In order to analyse this step, we use the Arrhenius plot of Eq.(27), which is presented in Figure 87. The measured activation energy was $E_A = 0.121$ eV, which is quite comparable to the value identified in [102] by photoluminescent (PL) measurements and attributed to an acceptor level caused by In vacancies. However, an activation energy of 0.170 eV was attributed to this defect in the calculation of Zhang and and Wei (see Table 7)

The defect densities over activation energy for all samples are calculated by temperature dependent admittance spectroscopy using the method of Walter et al. [15] given at Chapter 2, section 2.4.4. The defect density spectra are presented in Figure 88.

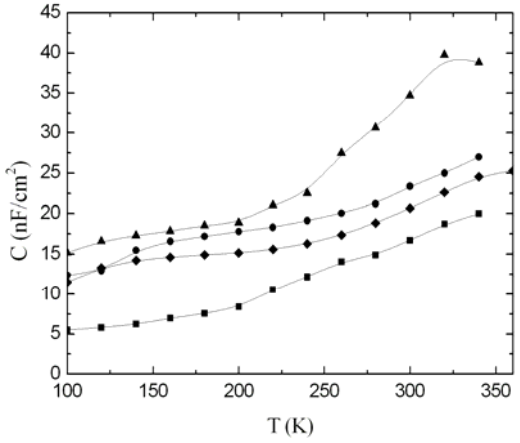

Figure 85 Capacitance-temperature measured at a frequency of 100 kHz for all samples. (■) sample 11 (Mo/Cr/SS1); (●) sample 25 (Mo/Cr/S); (▲) sample 4 (CrN/SS2); (◆) sample 13 (CrN/S).

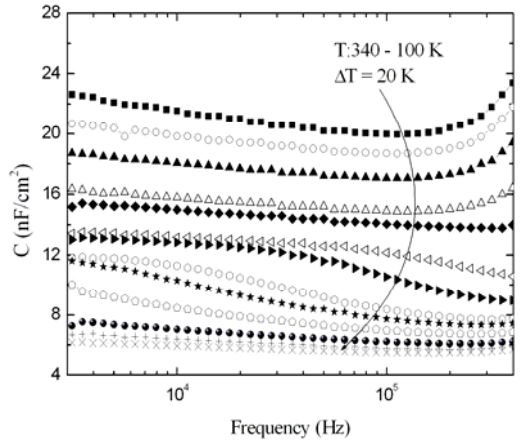

Figure 86 Measured capacitance frequency of sample 11 (Mo/Cr/SS1) in temperature range 100 - 340 K in steps of 20 K.

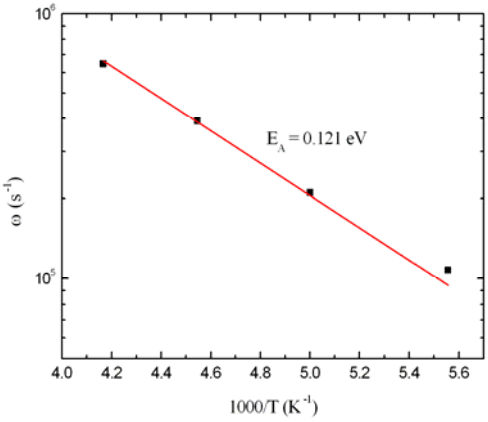

Figure 87 Arrhenius plot of the inflection frequencies deduced from Figure 86.

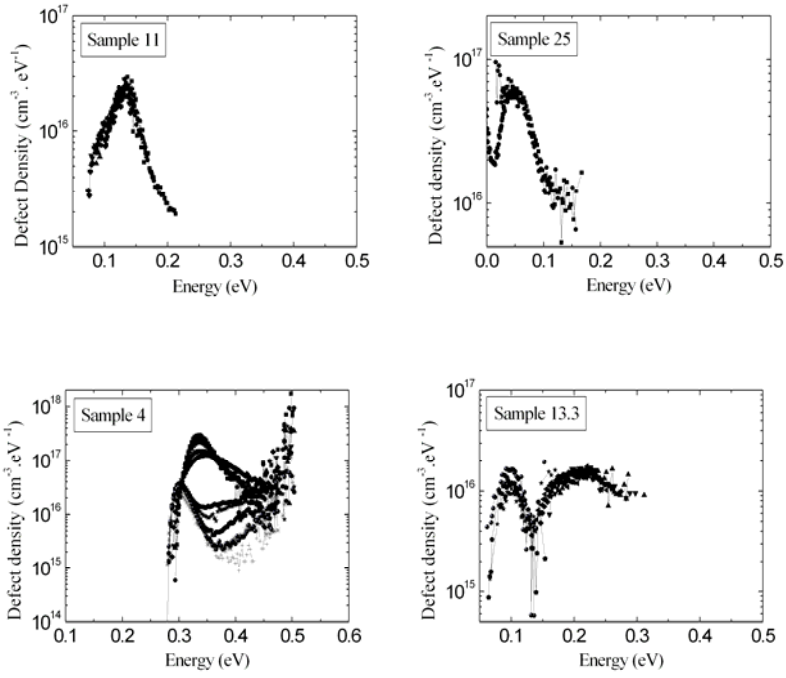

Figure 88 Defect density vs. activation energy calculated from the *C-f-T* spectra for all the samples. Sample 11 (Mo/Cr/SS1); sample 25 (Mo/Cr/S); sample 4 (CrN/SS2); sample 13 (CrN/S).

An energy level with an activation energy varying from 50-120 meV was found in samples 11, 25 and 13, with an apparent defect energy concentration of 3×10^{16} $cm^{-3}.eV^{-1}$, 6×10^{16} $cm^{-3}.eV^{-1}$ and 1.64×10^{16} $cm^{-3}.eV^{-1}$ respectively. This defect seems most likely to the so called N1, which was reported in CIGSe-based solar cells [77][91][105] and attributed to interfacial defects with activation energy between 50 meV and 250 meV [97].

Other defects were detected only in samples having CrN back contact (samples 4 and 13), which have a broad distribution centered at around 330 meV ($N_T = 3\times10^{17}$ $cm^{-3}.eV^{-1}$) and 300 meV ($N_T = 3.4\times10^{16}$ $cm^{-3}.eV^{-1}$) in sample 4 and 220 meV in sample 13 ($N_T = 1.6\times10^{16}$ $cm^{-3}.eV^{-1}$). These defects seem to have similar admittance spectrum as the trap commonly referred as N2 and considered as major recombination center leading to a degradation of CIGS solar cell performances, especially the open circuit voltage [93][105]. However this N2 is often observed in cells grown on a glass substrate and in these cells the level was only observed in samples grown on steel substrate with CrN as a back contact and the level is clearly absent if Cr barrier was deposited, thus we tentatively assign this level to a defect related to impurities diffusing from the substrate or the CrN back contact. We conclude that the increase of the doping density profile observed in sample 4 is probably caused by the high density of defect present in this sample. Therefore, the lower open circuit voltage values measured in samples 4 and 13 are certainly due to the presence of these defects in the CIGS absorber, grown with a CrN back contact.

6.3.6 DLTS measurements

Deep level transient spectroscopy measurements were performed on samples 11 and 4. The convention DLTS signal for the samples is shown in Figure 89. Here the negative peaks correspond with minority carrier emission, i.e. electron emission in the *p*-type CIGS absorber. For both samples a reverse biased pulse was applied which was not favourable for the observation of minority carrier traps , this observation suggests an inversion layer close to the buffer (CdS)/ absorber (CIGS) interface.

The Arrhenius plot of the emission rates presented in Figure 90, shows the apparent activation energy (E_T) and the apparent electron capture cross section (σ_{na}) observed for these samples. The emission energy obtained for sample 11 (E_t = 150 meV) and sample 4 (E_t = 300 meV) are in good agreement with those calculated from the AS measurements. From the

DLTS-spectra it could be concluded that not only the N1 level observed in sample 11, but also the level observed in sample 4 is negative and thus the energy position is relative to the conduction band. This confirms that this level originates from impurities related to the metallic substrate and is not the well-known N2 level. However, it is not obvious if the defect detected in sample 11 (Mo/Cr/S) with (E_t = 120 meV) by AS measurement and with (E_t = 150 meV) by DLTS measurement is the same or not. It could be that they are two defects presents in this sample, one an acceptor level at E_t = 120 meV (related to In vacancies) and the other one an interface defect layer N1 with E_t = 150 meV.

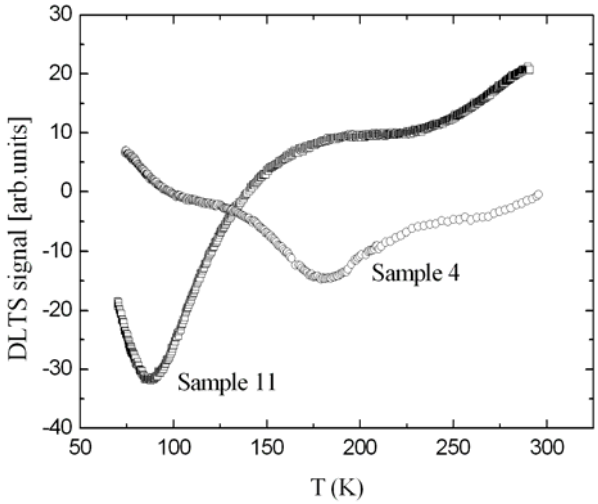

Figure 89 DLTS spectra measured for sample 11 (Mo/Cr/SS1) and sample 4 (CrN/S).

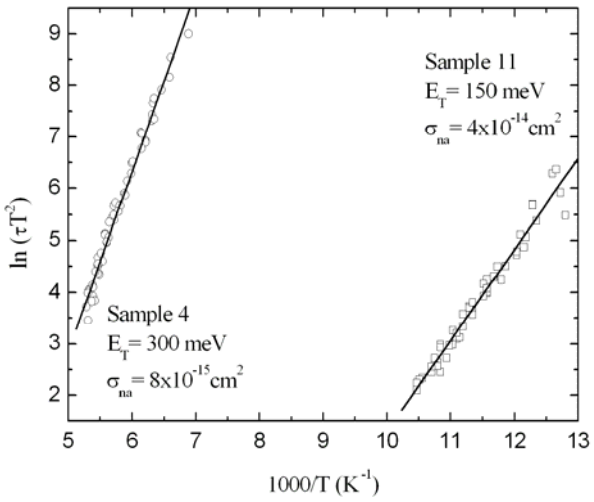

Figure 90 Arrhenius plots of DLTS peaks observed in Figure 5.7 in samples 11 and 4.

6.3.7 Simulation with SCAPS

From our measurements and the discussion above, it can be deduced that the structure, the composition and the morphology of the cells are not all the same (different CIGSe absorber layers grown on different metallic foils with or without barrier). Thus, it will be difficult to find one set of parameters which can fit all the cells. Nevertheless, we found a set of parameters for sample 25 (Mo/Cr/S) and sample 4 (CrN/SS2) which provided a reasonable good fit for *J-V*, *C-f* and *G-f* measurements.

The thicknesses of the different layers are those deduced from the SEM picture given in Figure 77. The doping density in the *p*-type CIGSe absorber layer is taken from the *C-V* measurement (Figure 79). In sample 25 (Mo/Cr/S) three types of defects have been implemented in the simulation. Two acceptors levels at 120 meV (N_t=10^{14} cm^{-3}) and 550 meV (N_t=3×10^{16} cm^{-3}) [107]. For the defect N1 detected in the AS measurement, we choose a donor level located in the OVC (ordered vacancy compound) layer at energy 50 meV below E_C, a defect density of 7×10^{16} $cm^{-3}.eV^{-1}$ as calculated from the admittance spectra in Figure 88. The *J-V* simulation is shown in Figure 91. Figure 92 a and b show *C-f* and G(ω)/ω respectively. It can be seen that the simulation agrees well with the measured data for sample 25.

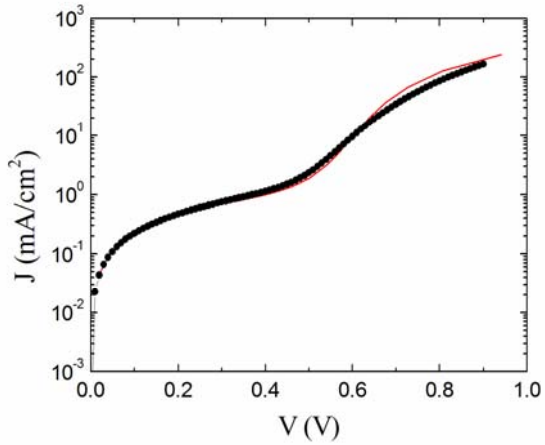

Figure 91 Simulation of the dark current-voltage characteristics of sample 25 (Mo/Cr/S) at room temperature. Closed circles: measurement points, red line: SCAPS simulation.

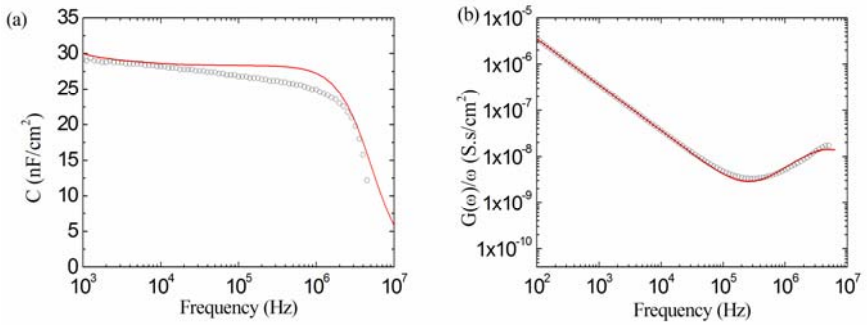

Figure 92 Simulation of admittance *C-f* and $G(\omega)/\omega$ for sample 25 (Mo/Cr/S) at room temperature. Open circles: measurements points, red line: SCAPS simulation.

By comparing the activation energies of 300 meV and 330 meV obtained for sample 4 (CrN/SS2) with the calculation of Zhang et Wei (see Table 6), one would assign these levels to the donor level indium-copper antisite In_{Cu}: (0/+) and (+/2+) with E_c-250 meV and E_c-340 meV repectively. In our simulation we include these two defects as donor-type defects with the respect concentrations deduced from the AS spectra. In Ref [97] this defect is considered as a deep recombination centre, which would explain the decrease in the open-circuit voltage observed in this sample. The

capacitance-frequency spectra are presented in Figure 93 in the temperature range 360-280 K. We found a good agreement between our simulation and the measurement.

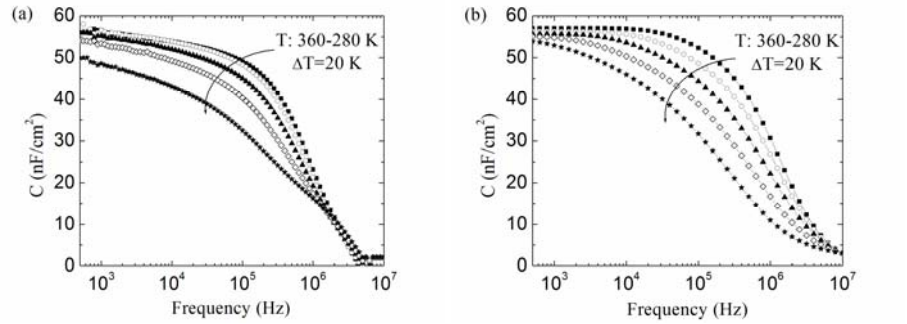

Figure 93 Capacitance-frequency spectra of sample 4 (CrN/SS2) in a temperature range 360-280 K in 20K step. (a) Measurement; (b) Simulation.

The effect of the defect concentration In_{Cu} on the open-circuit voltage is illustrated in Figure 94. As it can be seen increasing the concentration of both defects leads to a decrease in the open-circuit voltage. But the deeper one (330 meV) has a strong effect, since concentrations higher than 10^{17} $cm^{-3}.eV^{-1}$ decrease drastically the open-circuit voltage.

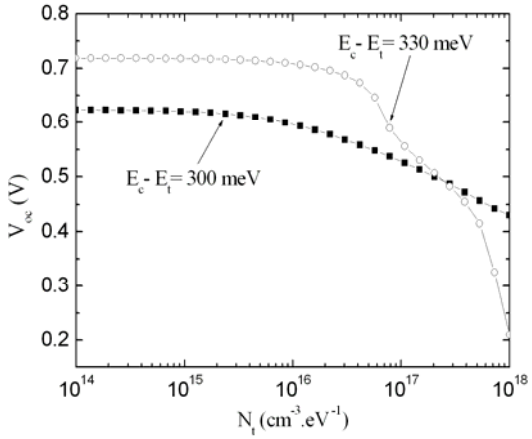

Figure 94 Open-circuit voltage vs. trap density of level In_{Cu} (E_c-E_t = 330 meV and E_c-E_t = 300 meV).

Even though the simulations allowed us to predict the defects present in this sample, unfortunately the relation between the presence of In_{Cu} and the diffusion of Cr and Fe in the absorber is still not clear for us.

Chapter 7

Conclusions and outlook

During the preparation of this thesis, investigations have been made on different solar cells by the means of simulation and different measurement processes, in order to define and understand the different physics phenomena governing the cell's operation and limiting or not their performance.

Our investigation of the IPV effect (Impurity Photovoltaic effect) in silicon and gallium arsenide solar cells, has led to the following major conclusions:

- The choice of an appropriate structure (a pnn^+ in our case) has the advantage to reduce recombination process in the solar cell and however save the value of the open-circuit voltage V_{oc}.
- Light trapping is very important to give a positive benefit to the IPV effect, by increasing the opportunity for photons to be absorbed weak optical process in the cell.
- Good light management, ensuring internal reflection coefficients exceeding 99 % is needed to observe any IPV effect.
- The impurity concentration should be close but not exceed the base doping.
- When two impurity levels are present (as in the case of copper in GaAs), the IPV effect is higher with only the deepest level present.

- The presence of more than one impurity level gives an improvement in the short-circuit current (J_{sc}) but a decrease in the open-circuit voltage (V_{oc}), due to the increase of recombination in the solar cell.

Our calculations of the effect of temperature and series resistance in GaAs concentrator solar cells, shows a degradation of the cell's output in the case of air cooling system operation, due to the increase of temperature of the cell with the concentration of the light. Thus, cooling by air is not enough for a better performance of GaAs solar cells under concentration. However, water cooling allows for heat recovery and the performances are appreciably better than air cooling, especially by using a turbulent mode. The effect of series resistance is very crucial in such cells especially at thigh concentration. Thus it is important to minimize series resistance in solar cells operated at high concentration ratio.

Perimeter surface recombination is very important in small area solar cells as it is inversely proportional to the size of the cell characterised by the perimeter to area ratio.

Using a one-dimensional simulator for micro-solar cells could lead to drastic errors particularly for higher P/A values. With the presence of an important density of surface states Fermi level is pinned near mid-gap, and hence the electric field at the *p–n* junction surface could be assumed uniform. With this approximation and treating recombination at the surface in a similar manner to that of bulk space charge region we have obtained an analytical expression of the recombination current at the surface of the depleted layer. The obtained analytical expression is used as a correction to the dark current obtained by SCAPS. The simulated results of a 0.5×0.5 cm cell with the introduction of the correction term are much closer to the experimental and fitted results than those of SCAPS alone. The perimeter recombination current, even for this relatively large area cell, is important and counted about 10% of the total dark current. The open circuit voltage, the fill factor and the conversion efficiency decrease significantly when the area of the cell is reduced. The most significant deterioration was recorded in the value of the efficiency. For MEMS application solar cell open circuit voltage is the important parameter. As the open-circuit voltage is reduced more area is required to produce the desired high voltage. One way of reducing the perimeter recombination is to passivate surface states by appropriate surface treatment. Once the density of surface states is reduced the assumption of the

fully pinned Fermi level no longer holds. However, the determination of the electric field at the surfaces becomes a difficult task and it will be necessary to solve the neutrality equation in the three regions of the diode (*n*, *p*-sides and space-charge region). Furthermore, a better understanding of the perimeter recombination and surface states properties is needed to obtain a more accurate model for the perimeter current.

GaAs *p-i-n* solar cells with different intrinsic layer widths have been investigated under dark and illumination conditions.

An improvement in *p-i-n* solar cell performances was observed with the increase in the intrinsic layer width. *p-i-n* cells showed lower dark current and higher open-circuit voltage, short-circuit current and efficiency compared to *pn* cells. Our measurements and simulations on these cells, confirmed that these better performances in the *p-i-n* cells are due to their materials parameters and not to the presence of high electric field in the *i*-layer.

Electrical characterization of CIGSe thin film solar cells grown on different metallic foils with or without barrier layer, showed that the best cells are those grown with Cr barrier on Mo and had an efficiency exceeding 13 %. Excellent efficiency uniformity was observed in sample 25 (Mo/Cr/S) probably related to the type of substrate/barrier combination (the type of the SS substrate used for this sample). The other samples (4 (CrN/SS2) and 13 (CrN/S)) had lower efficiencies caused by lower open circuit voltages. Different kind of defects were detected in these cells by AS and DLTS measurements. A defect level with an activation energy varying from 50-150 meV was detected in almost all the cells. This defect closely resembles the N1 defect reported in the literature, and which is attributed to interfacial defects (V_{Se}). Cells grown on CrN contact/barrier layer showed a decrease in cell's performance and especially in the open circuit voltage. This is due to the presence of a deep recombination defect detected by AS measurements only in these cells, and which altered the CIGSe absorber quality. By simulation, we tentatively assign these defects to the In_{Cu} (0/+) and In_{Cu} (+/2+). However, the effect of out-diffusion of Cr and Fe to the absorber layer and the presence of this defect is still unclear.

Appendix A

The AlGaAs/GaAs superlattice BSF layer

To model the AlGaAs/GaAs superlattice BSF layer, we use a simple approach in replacing this layer with a single layer with effective properties. We use the data for the III-V materials system form the Ioffe Institute in Petersburg, Russia [73].

$Al_xGa_{1-x}As$ has a direct band gap when $x < 0.45$ eV, which is given by:

$$\frac{E_g(x)}{\text{eV}} = 1.424 + 1.247\,x \text{ eV} \quad \rightarrow \quad E_g(0.36) = 1.873 \text{ eV} \tag{97}$$

The band discontinuities are given by:

$$\begin{aligned} &\frac{\Delta E_C}{\text{eV}} = 0.79\,x \text{ when } x < 0.41 \\ &\frac{\Delta E_C}{\text{eV}} = 0.475 + 0.335\,x + 0.143\,x^2 \quad \text{when } x > 0.41 \\ &\qquad \rightarrow \quad \Delta E_C(0.36) = 0.284 \text{ eV} \\ &\frac{\Delta E_V}{\text{eV}} = -0.46\,x \quad \rightarrow \quad \Delta E_V(0.36) = 0.166 \text{ eV} \end{aligned} \tag{98}$$

With these data and with $a = 2.7$ nm, the width of the GaAs well, we find the energy levels in the well, see Figure 95: $E_{e1} - E_C = 0.102$ eV and $E_V - E_{h1} = 50$ meV, $E_V - E_{h2} = 183$ meV.

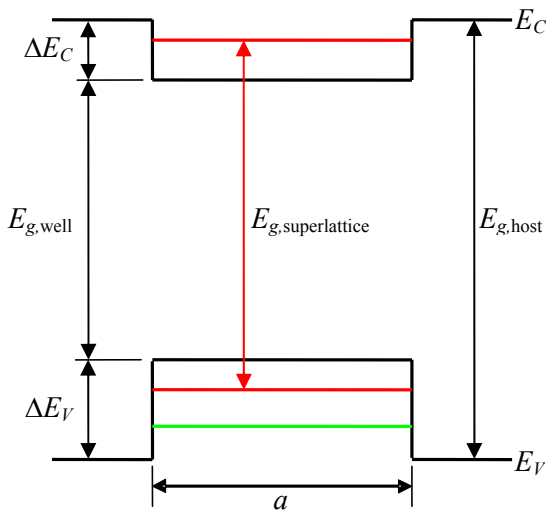

Figure 95 Energy levels in a GaAs quantum well in an $Al_xGa_{1-x}As$ (x = 0.36) host material [73]. The first electron level in the well is 102 meV above E_C, and the first and second hole level are 50 meV and 183 meV below E_V.

When the quantum well in Figure 95 is repeated periodically, the localised levels in the well may overlap and form minibands ([107], p.59). We take the position of these minibands approximately coinciding with the first electron and hole levels in the well. Thus, we consider the superlattice as a material with a band gap of (1.420 + 0.102 + 0.050) eV = 1.572 eV, and with electron affinity (4.070 – 0.102) eV = 3.99 eV. Here E_g = 1.42 eV and χ = 4.07 eV are the values for the GaAs base material. All properties of the effective superlattice material should be assigned effective values: densities of states, mobilities, … We will use the values for pure GaAs, and check afterwards that these values are not critical at all for the cell performance. We will disregard the function of the superlattice BSF as a dielectric Bragg reflector in the near infrared. This will result in some small error in the simulated quantum efficiency at long wavelengths.

Bibliography

[1] REN 21 Renewable Energy Policy Network for the 21st Century, Renewable global status report: http://www.ren21.net/

[2] I. Repins, M. Contreras, B. Egaas, C. DeHart, J. Scharf, C. Perkins, B. To and R. Noufi, "19·9 %-efficient ZnO/CdS/$CuInGaSe_2$ solar cell with 81·2% fill factor", *Progress in Photovoltaics*, vol. 16-3, pp. 235-239, 2008.

[3] M. Burgelman, J. Verschraegen, S. Degrave and P. Nollet, "Modeling thin film PV devices", *Progress in Photovoltaics*, vol. 12, pp. 143-153, 2004.

[4] M. Burgelman, P. Nollet, S. Degrave, "Modeling polycrystalline semiconductor solar cells", *Thin Solid Films*, vol. 361-362, pp.527-532, 2000.

[5] M. Green, "Third generation photovoltaics: ultra-high conversion efficiency at low cost", *Progress in Photovoltaics*, vol. 9, pp. 123-135, 2001.

[6] M. Green, K. Emery, Y. Hishikawa and W. Warta, "Solar cell efficiency tables (Version 33)", *Progress in Photovoltaics*, vol. 17, pp. 85-94, january 2009.

[7] S. M. Sze, *Physics of Semiconductor Devices*, 2nd ed, Wiley & Sons, New York, 1981.

[8] S. Khelifi, A. Belghachi, "Le rôle de la couche fenêtre dans les performances d'une cellule solaire GaAs", *Revue des Energies Renouvelables*, vol. 7, pp.13-21, 2004.

[9] A. Belghachi, S. Khelifi, "Modelling of the perimeter recombination effect in GaAs-based micro-solar cell", *Solar Energy Materials and Solar Cells*, Vol.90, No.1, pp.1-14, 2006.

[10] S. Selberherr, *Analysis and Simulation of Semiconductor Devices*, Springer Verlag, Wien - NewYork, 1984.

[11] Johan Verschraegen, *Karakterisering en modellering met SCAPS van de CISCuT dunne-filmzonnecel*, Doctorate's thesis, ELIS, University of Gent, 2007.

[12] A. Jasenek, U. Rau, V. Nadenau, H.-W. Schock, "Electronic properties of $CuGaSe_2$-based heterojunction solar cells. Part II. Defect spectroscopy", *Journal of Applied Physics*, vol. 87, No.1, pp.594-602, 2000.

[13] H. Tavakolian, J.R. Sites, "Capacitance determination of interfacial states in $CuInSe_2$ solar cells", in *Proceedings 18th IEEE Photovoltaics Specialists Conference*, Las Vegas, pp.1065-1068, 1985.

[14] D.L. Losee, "Admittance spectroscopy of impurity levels in Schottky barriers", *Journal of Applied Physics*, vol. 46, No.8, pp.2204-2214.

[15] T. Walter, R. Herberholz, C. Müller, H.W. Schock, "Determination of defect distribution from admittance measurements and application to $Cu(In,Ga)Se_2$ based heterojunctions, *Journal of Applied Physics*, vol. 80, No.8, pp.4411-4420, 1996.

[16] J. Lauwaert, K. Decok, S. Khelifi, M. Burgelman, "A simple correction method for series resistance and inductance on solar cell admittance spectroscopy", submitted to *Solar Energy Materials and Solar Cells*.

[17] P. Würfel, "Limiting efficiency for solar cells with defects from a 3-level model", *Solar Energy Materials and Solar Cells*, vol. 29, No.4, pp.403-413, 1993.

[18] M.J. Keevers and M.A. Green, "Efficiency improvement of silicon solar cells by impurity photovoltaic effect", *Journal of Applied Physics*, vol. 75, no. 8, pp. 4022-4031, 1994.

[19] M. Schmeits and A. Mani, "Impurity photovoltaic effect in c-Si solar cells. A numerical study", *Journal of Applied Physics,* vol. 85, no. 4, pp. 2207-2212, 1999.

[20] G. Beaucarne, A. S. Brown, M.J. Keevers, R. Corkish, M.A. Green, "The impurity photovoltaic (IPV) effect in wide-band gap semiconductors: An opportunity for very-high-efficiency solar cells?", *Progress in Photovoltaics Research and Application*, vol. 10, pp. 345-353, 2002.

[21] S. Khelifi, J. Verschraegen, M. Burgelman, A. Belghachi, "Numerical Simulation of Impurity Photovoltaic Effect in Silicon Solar Cells", *Renewable Energy*, vol. 33, pp.293 – 298, 2008.

[22] J. Verschraegen, S. Khelifi, M. Burgelman, A. Belghachi, Numerical Modelling of the Impurity Photovoltaic Effect (IPV) in SCAPS, Proceedings of the 21th European Photovoltaic Solar Energy Conference, Dresden, Germany, September 2006, pp. 396-399.

[23] S. Khelifi, M. Burgelman, J. Verschraegen, A. Belghachi, "Impurity photovoltaic effect in GaAs solar cell with two deep impurity levels",

Solar Energy Materials and Solar Cells", Vol.92, No.12, pp.1559-1565, 2008.

[24] G. Lucovsky, "On the photoionization of deep impurity centers in semiconductor solar cells", *Solid-State Communications*, vol. 3, pp. 299-302, 1965.

[25] D.K. Schroder, R.N. Thomas and J.C. Swartz, "Free carrier absorption in silicon", *IEEE Transaction on Electron Devices,* vol. ED-25, pp. 254-261, 1978.

[26] M.A. Green, *High Efficiency Silicon Solar Cells*, Trans Tech Publications, Aedermansdorf, 1987.

[27] H.M. Hobgood, T.T. Braggings, M.J. Sopira, J.C. Swartz and R.N. Thomas, "Growth and characterization of indium-doped silicon for extrinsic IR-detectors", *IEEE Transaction on Electron Devices*, vol. ED-27, pp. 14-23, 1980.

[28] A. G. Milnes, *Deep impurities in semiconductors*, New-York: Wiley, 1973.

[29] P. N. K. Deenapanray, V. A. Colemn, C. Jagadish, "Electrical characterization of impurity-free disordered p-type GaAs", *Electrochemical and Solid-State Letters*, vol. 6, pp. G37-G40, 2003.

[30] P. N. K. Deenapanray, M. Petravic, C. Jagadish, M. Krispin, F.D. Auret, "Electrical characterization of p-GaAs epilayers disordered by doped spin-on-glass", *Journal of Applied Physics*, vol. 97, pp. 1-7, 2005.

[31] S. M. Sze, *Modern semiconductor device physics*, New York: Wiley, 1998.

[32] S. M. Sze, *Semiconductor devices, physics and technology*, New York: Wiley, 1985.

[33] J.J. Liou, W.W. Lang, "Comparison and optimization of the performance of Si and GaAs solar cells", *Solar Energy Materials and Solar Cells*, vol. 28, pp. 9-28, 1992.

[34] S.P. Tobin, S.M. Vernon, C. Bajgar, S.J. Wojtczuk, M.R. Melloch, M.S. Lundstrom, K.A. Emery, "Assessment of MOCVD-and MBE-grown GaAs for high-efficiency solar cell applications", *IEEE Transaction on Electron Devices*, vol. 37, No. 2, pp. 469-475, 1990.

[35] B.H. Yang, D. Seghier and H.P. Gislason, "Compensation mechanism and transport behaviour of semi-insulating GaAs:Cu", *Proceedings of Semiconducting and Semi-Insulating Materials Conference*, 29 Apr-3 May 1996, Toulouse, France, IEEE, pp. 163-166, 1996.

[36] P. Blood and J.J. Harris, "Deep states in GaAs grown by molecular beam epitaxy", *Journal of Applied Physics*, vol. 56, No. 4, pp. 993-1007, 1984.

[37] S. Brehme, R. Pickenhain, "An acceptorlike electron trap in GaAs related to Ni", *Solid State Communications*, vol. 59, pp. 469-471, 1986.

[38] C.H. Henry, D.V. Lang, "Non radiative capture and recombination by multiphonon emission in GaAs and GaP", *Physical Review B*, vol. 15, pp. 989-1015, 1997.

[39] K. Leosson and H.P. Gislason, "Thermal and Eletrical of Cu-Related Acceptors in Li-and H-Passivated GaAs", *Physica Scripta*, vol. T69, pp. 196-201, 1997.

[40] S. Adachi, "*Optical constants of crystalline and amorphous semiconductors, Numerical data and graphical information*", Kluwer Academic Publishers, USA, 1999.

[41] T.D. Dzhafarov, M. Sirin, S. Akciz, "Photoelectrical characteristics of GaAs *p-n* junctions formed by Cu photostimulated diffusion", *Journal of Physics D*, vol. 31, pp.L17-L19, 1998.

[42] C.B. Honsberg and A.M. Barnett, "Light trapping in thin film GaAs solar cells", *Proceedings of 22nd IEEE Photovoltaic Specialists Conference*, October 1991, Las Vegas, NV, New York , IEEE, pp. 262–267, 1991.

[43] M.E. Klausmeir-Brown, "Status, prospects, and economics of terrestrial single junction GaAs concentration cells", in: Solar cells and their applications, edited by L.D. Partain, Wiley, New York, 1995.

[44] A. Goetzberger, "Optical confinement in thin silicon solar cells by diffuse back reflectors", *Proceedings of 15th IEEE Photovoltaic Specialists Conference*, IEEE, pp.867-870, 1981.

[45] W. Shockley and W. Read, "Statistics of the recombination of holes and electrons", *Physical Review*, vol. 87, pp. 835-842, 1952.

[46] C. T. Sah and W. Shockley, "Electron-hole recombination statistics in semiconductors through flaws with many charge conditions", *Physical Review*, vol. 109, pp. 1103-1115, 1958.

[47] R. Schropp and M. Zeman, "*Amorphous and microcrystalline silicon solar cells: modelling, materials and device technology*", Boston: Kluwer Academic Publishers, (pp. 133 and pp. 138-140), 1998.

[48] G.J. Bauhuis, P. Mulder, J.J. Schermer, E.J. HaverKamp, J. Van Deelen, P.K. Larsen, " High efficiency thin film GaAs solar cells with improved radiation hardness", *20th European Photovoltaic Solar Energy Conference*, June 2005, Barcelona, pp.468-471, 2005.

[49] L.W. James, R.L. Moon, "GaAs concentrator solar cells", *Proceeding of 11th IEEE Photovoltaic Specialists Conference*, New York, pp.402-408, 1975.

[50] G.L. Araújo, "Compound semiconductor solar cells" in: A. Luque, "Solar cells and optics for photovoltaic concentration", Adam Hilger series on optics and optoelectronics, Bristol, 1989.

[51] J.M. Woodall, H.J. Hovel, "Isothermal etchback-regrowth method for high efficiency $Ga_{1-x}Al_xAs$-GaAs solar cells", *Applied Physics Letters*, vol. 30, No. 9, pp. 492-493, 1977.

[52] J.C.C. Fan, C.O. Bozler, R.L. Chapman, "Simplified fabrication of GaAs homojunction solar cells with increased conversion efficiencies", *Applied Physics Letters*, Vol.32, No.6, pp.390-392, 1978.

[53] S. Khelifi, L. Ayat Leila, A. Belghachi, "Effects of temperature and series resistance on GaAs concentrator solar Cell", *European Physical Journal, Applied Physics*, vol. 41, pp.115 – 119, 2008.

[54] G. Sala, "Cooling of solar cells", in: A. Luque, "Solar cells and optics for *photovoltaic concentration*", Adam Hilger series on optics and optoelectronics, Bristol, 1989.

[55] A. Royne, C.J. Dey, D.R. Mills, "Cooling of photovoltaic cells under concentrated illumination: a critical review", *Solar Energy Materials and Solar Cells*, vol. 86, pp.451-483, 2005.

[56] H.C. Hamaker, C.W. Ford, J.G. Werthen, G.F. Virshup, N.R. Kaminar, D.L. King, J.M. Gee, "26 % efficient magnesium-doped AlGaAs/GaAs solar concentrator cells", *Applied Physics Letters*, vol. 47, No.7, pp.762-764, 1985.

[57] M.W. Edenburn, "Active and passive cooling for concentrating photovoltaic arrays", in *Proceeding of 14th IEEE Photovoltaic Specialists Conference*, San Diego, pp.771-776, 1980.

[58] J.C. Minãno, J.C. Gonzalez, I. Zanesco, "Flat high concentration devices", in *24th Proceeding IEEE Photovoltaic Specialists Conference*, pp.1123-1126, 1994.

[59] A.G. Aberle, P.P. Altematt, G. Heiser, S.J. Robinson, A.H. Wang, J.H. Zhao, U. Krumbein, M.A. Green, "Limiting loss mechanisms in 23 % efficient silicon solar cells", *Journal of Applied Physics*, vol. 77, No.7, pp.3491-3504, 1995.

[60] C.H. Henry, R.A. Logan, F.R. Merrit, "The effect of surface recombination on current in $Al_xGa_{1-x}As$ heterojunctions", *Journal of Applied Physics*, vol. 49, No.6, pp.3530-3542, 1978.

[61] P.E. Dodd, T.B. Stellwag, M.R. Melloch, M.S. Lundstrom, "Surface and perimeter recombination in GaAs Diodes: An experimental and theoretical investigation", *IEEE Transactions on Electron Devices*, vol. 38, No.6, pp.1253-1261, 1991.

[62] C. Walther, R.P. Blum, H. Niehus, W.T. Masselink, "Modification of Fermi-level pinning of GaAs surface through InAs quantum dots", *Physical Review B*, vol. 60, No.20, pp.R13962-R13965, 1999.

[63] J.S. Blakemore, "Semiconducting and other major properties of gallium arsenide, *Journal of Applied Physics*, vol. 53, No.10, pp.R123-R181, 1982.

[64] J. Ohsawa, M. Kawasaki, T. Tanaka, N. Tsuchida, "A GaAs micro solar cell with output voltage over 20 V", *Japanese Journal of Applied Physics*, vol. 38, No.12A, pp.6947-6951, 1999.

[65] K. Taretto, U. Rau and J.H. Werner, "Closed-form expression for the current/voltage characteristics of *pin* solar cells", *Applied Physics A*, vol. A77, pp. 865-871, 2003.

[66] C.Y. Tsai, W.H. Bloß, K. Zieger, F. Scholz, V. Frese, U. Blieske, "High efficiency NIP GaInP solar cells grown by MOVPE", in *Proceedings of 13th European Photovoltaic Energy Solar Energy Conference*, Nice, pp.918-920, 1995.

[67] A. Bett, F. Dimroth, G. Stollwerck and O. Sulima, "III-V compounds for solar cell applications", *Applied Physics A*, vol. A69, pp. 119-129, 1999.

[68] N. Konofas, E.K. Evangelou, F. Scholz, K. Zieger, E. Aperathitis, "Electrical characterization and carrier mechanisms of GaAs p/i/n devices for photovoltaic applications", Materials Science Engineering B, vol. 80, pp.152-155, 2000.

[69] T.J. Drummond, J. Klen, D. Arnold, R. Fischer, R.E. Thorne, W.G. Lyons, H. Morkoc, "Use of superlattice to enhance the interface properties between two bulk heterolayers", *Applied Physics Letters*, vol. 42, pp.615-617, (1983).

[70] M. McPherson, B.K. Jones and T. Sloan, "Effects of radiation damage in silicon *p-i-n* photodiodes", *Semicond. Sci. Technol*, vol. 12, p. 1187, 1997.

[71] A. Salètes, J.P. Contour, M. Leroux, J. Massies, N. Defranould and G. Pelous, GaAlAs/GaAs solar cells grown by molecular beam epitaxy: Material properties and device parameters, Sol. Cell 17 (1986) 373-381.

[72] M.A. Green, Solar Cells: Operating Principles, Technology and System Applications, University of New South Wales, Kensington, 1998.

[73] http://www.ioffe.ru/SVA/NSM/Hetero/index.html (October 2009). Information provided by the Ioffe Physica-technical Institute, 26 Polytekhnicheskaya, St. Petersburg 194021, Russia.

[74] H. McLeod, "Thin film optical devices", in Active and passive thin film devices, T. Coutts (ed.), Academic Press, London, pp. 321-428, 1978.

[75] U. Rau, H.W. Schock, "Electronic properties of Cu(In,Ga)Se_2 heterojunction solar cells-recent achievements, current understanding,

and future challenges", *Applied Physics A*, vol. 69, No.2, pp.131-147,1999.

[76] I. Hengel, R. Klenk, in Proceedings of 2nd World Conference and Exhibition on Photovoltaic Solar Energy Conversion, pp.545, 1996.

[77] D.S. Albin, J. Carapella, J.R. Tuttle, N.R. Noufi, in *Proceedings of Material Research Society Symposium*, vol. 228, pp. 267, 1992.

[78] J.R. Tuttle, A.Szalaj, J.Keane, in Proceedings of 28th IEEE Photovoltaic Specialists Conference, Anchorage, pp.1042-, 2000.

[79] S. Ishizuka, H. Hommoto, N. Kido, K. Hashimoto, A. Yamada, S. Niki, "Efficiency enhancement of Cu(In,Ga)Se_2 solar cells fabricated on flexible polyimide substrates using alkali-silicate glass thin layers", *Applied Physics Express*, vol. 1, pp.1-3, 2008.

[80] S. Khelifi, J. Marlein, M. Burgelman, A. Belghachi, "Electrical characteristics of Cu(In,Ga)Se_2 thin films solar cells on metallic foil substrates" in *Proceeding of 23rd European Photovoltaic Solar Energy Conference*, Valencia, pp.2165-2169, 2008.

[81] S.Khelifi, A.Belghachi, J. Lauweart, J. Wienke, R. Caballero, C.A. Kaufmann, M. Burgelman, "Characterization of flexible thin film CIGSe solar cells grown on different metallic foil substrates, presented in *E-MRS Spring Meeting*, Strasbourg, 2009.

[82] W.N. Shafarman, J. Zhu, "Effect of substrate temperature and deposition profile on evaporated Cu(In,Ga)Se_2 films and devices", *Thin Solid Films*, vol. 361-362, pp.473-477, 2000.

[83] V. Alberts, S. Zweigart, H.W. Schock, "Preparation of device quality $CuInSe_2$ by selenization of Se-containing precursors in H_2Se atmosphere", *Semiconductor Science and Technology*, vol. 12, pp.217-223, 1997.

[84] R. Caballero, C.A. Kaufmann, T. Eisenbarth, M. Cancela, R. Hesse, T. Unold, A. Eicke, R. Klenk, H.W. Schock, "The influence of Na on low temperature growth of CIGS thin film solar cells on polyimide substrates", Thin Solid Films, Vol.517, No.7, pp.2187-2190, 2009.

[85] C.A. Kaufmann, A. Neisser, R. Klenk, R. Scheer, "Transfert of Cu(In,Ga)Se_2 thin film solar cells to flexible substrate using an in situ process control", *Thin Solid Films*, vol. 480-481, pp.515-519, 2005.

[86] D. Schmid, M. Ruckh, F. Grunwald, H.W. Schock, "Chalcopyrite/defect chalcopyrite heterojunctions on the basis of $CuInSe_2$", *Journal of Applied Physics*, Vol.73, No.6, pp.2902-2909, 1993.

[87] S.B. Zhang, S.H-.Wei, A. Zunger, H. Katayama-Yoshida, "Defect Physics of $CuInSe_2$ chalcopyrite semiconductor", *Physical Review B*, vol. 57, No.16, pp.9642-9656, 1998.

[88] S.H-. Wei, S.B. Zhang, A. Zunger, "Effects of Ga addition to $CuInSe_2$ on its electronic, structural, and defect properties", *Applied Physics Letters*, vol. 72, pp.3199-3201, 1998.

[89] R. Herberholz, M. Igalson, H.W. Schock, "Distinction between bulk and interface states in $CuInSe_2$/CdS/ZnO by space charge spectroscopy", *Journal of Applied Physics*, vol. 83, No.1, pp.318-325,1998

[90] M. Igalson, M. Edoff, "Compensating donors in $Cu(In,Ga)Se_2$ absorbers of solar cells", *Thin Solid Films*, vol. 480-481, pp.322-326, 2005.

[91] J.T. Heath, J.D. Cohen, W.N. Shafarman, "Bulk and metastable defects in $CuIn_{1-x}Ga_xSe_2$ thin film using drive-level capacitance profiling", *Journal of Applied Physics*, vol. 95, No.3, pp.1000-1010, 2004.

[92] M. Burgelman, F. Engelhardt, J. F. Guillemoles, R. Herberholz, M. Igalson, R. Klenk, M. Lampert, T. Meyer, V. Nadenau, A. Niemegeers, J. Parisi, U. Rau, H. W. Schock, M. Schmitt, O. Seifert, T. Walter, S. Zott, "Defects in $Cu(In,Ga)Se_2$ semiconductors and their role in the device performance of thin film solar cells", *Progress in Photovoltaics: Research and Applications*, vol. 5, No.2, pp.121-130, 1997.

[93] U. Rau, M. Schmidt, A. Jasenek, G. Hanna, H.W. Schock, "Electrical characterization of $Cu(In,Ga)Se_2$ thin film solar cells and the role of defects for the device performance", *Solar Energy Materials and Solar Cells*, vol. 67, pp.137-143, 2001.

[94] M. Igalson, A. Urbaniak, M. Edoff, "Reinterpretation of defect levels derived from capacitance spectroscopy of CIGSe solar cells", *Thin Solid Films*, vol. 517, pp.2153-2157, 2009.

[95] F. Kessler, D. Rudmann, "Technological aspects of flexible CIGS solar cells and modules", *Solar Energy*, vol. 77, No.6, pp.685-695, 2004.

[96] T. Wada, N. Kohara, M. Nishitani, "Chemical and structural characterization of $Cu(In,Ga)Se_2$ solar cells", *Japanese Journal of Applied Physics*, vol. 35, pp.L1253-1256,1996.

[97] U. Rau, H.W. Schock, *Cu(In,Ga)Se₂ solar cells* in: M.D. Archer, R. Hill, Series on photoconversion of solar energy, Imperial College Press, vol. 1, 2001.

[98] K. Orgassa, H.W. Schock, J.H. Werner, "Alternative back contact materials for thin film $Cu(In,Ga)Se_2$ solar cells", *Thin Solid Films*, vol. 431-432, pp.387-391, 2003.

[99] F. Kessler, D. Hermann, M. Powalla, "Approach to flexible CIGS thin-film solar cells", Thin Solid Films, vol. 480-481, pp.491-498, 2005.

[100] C.A. Kaufmann, R. Caballero, T. Unold, R. Hesse, R. Klenk, S. Schorr, M. Nichterwitz, H.-W. Schock, "Depth profiling of $Cu(In,Ga)Se_2$ thin films grown at low temperatures", Solar Energy Materials and Solar Cells, Vol. 93, pp.859-863, 2009.

[101] T. Unold, T. Enzenhofer, C.A. Kaufmann, R. Klenk, "Analysis of defects in Coevaporated high-efficiency $Cu(In,Ga)Se_2$ solar cells", in *Proceedings of 4th World Conference on Photovoltaic Energy Conversion*, Hawaii, pp.356-359, 2006.

[102] C.A. Kaufmann, T. Unold, D. Abou-Ras, J. Bundesman, A. Neisser, R. Klenk, R. Scheer, K. Sakurai, H.-W. Schock, "Investigation of coevaporated $Cu(In,Ga)Se_2$ thin films in highly efficient solar cell devices", *Thin Solid Films*, vol. 515, pp.6217-6221, 2007.

[103] A.M. Gabor, J.R. Tuttle, M.H. Bode, A. Franz, A.L. Tennant, M.A. Contreras, R. Noufi, D. Garth Jensen, M.A. Hermann, Solar Energy Materials and Solar Cells, vol. 4142, pp.247-260, 1996.

[104] F.B. Dejene, V. Alberts, "Structural and optical properties of homogeneous $Cu(In,Ga)Se_2$ thin films prepared by thermal reaction of InSe/Cu/GaSe alloys with elemental Se vapour", *Journal of Physics D*, Vol.38, No.1, pp.22-25, 2005.

[105] R. Herberholz, D. Braunger, H.W. Schock, T. Haalboom, F. Ernst, "Performance and defects in $Cu(In,Ga)Se_2$ heterojunctions: combining electrical and structural measurements", in Proceedings of 14th European Photovoltaic Solar Energy Conference, Barcelona, pp.1246-1249, 1997.

[106] C. Deibel, A. Wessel, V. Dyakonov, J. Parisi, J. Palm, F. Karg, "Deep-level in stoichiometry-varied $Cu(In,Ga)(S,Se)_2$ solar cells", *Thin Solid Films*, 431-432, pp.163-166, 2003

[107] S.M. Sze and Kwok K. Ng, *Physics of semiconductor devices*, 3rd. edition, Wiley & Sons, New-York, 2007.